Master's thesis

NTNU
Norwegian University of Science and Technology
Faculty of Natural Sciences
Department of Physics

Øyvind Finnseth

Ferromagnetically mediated singlet-triplet qubit coupling

Master's thesis in Nanotechnology
Supervisor: Jeroen Danon
June 2022

NTNU
Norwegian University of
Science and Technology

Øyvind Finnseth

Ferromagnetically mediated singlet-triplet qubit coupling

Master's thesis in Nanotechnology
Supervisor: Jeroen Danon
June 2022

Norwegian University of Science and Technology
Faculty of Natural Sciences
Department of Physics

NTNU
Norwegian University of
Science and Technology

Abstract

The progress towards the realization of quantum computing is contingent upon the understanding and development of suitable physical systems in which quantum bits may be encoded. However, the requirements placed on such a system pose significant research challenges. Quantum bits need to be reliable and robust in the face of noise, easy to manipulate, and possess the scalability necessary to create powerful quantum processors. Despite the significant strides made in recent years, a qubit design that is able to satisfy these requirements well enough for applications within quantum information has yet to be realized. Further progress within the field thus depends on finding novel systems for hosting and coupling quantum bits. A promising field in that regard is in hybrid systems in which we may utilize the combined properties of the individual subsystems.

In this thesis we consider one such proposal: singlet-triplet spin qubits hosted in double quantum dots, coupled through exchange interaction to a ferromagnet. Through a combined analytical and numerical analysis, we evaluate the potential of the system to provide intermediate-range coherent qubit-qubit coupling with little to no leakage.

We derive the Hamiltonian of the combined system, including magnetic anisotropy in the ferromagnet, and find that the introduction of anisotropy gives rise to tunable rotating and counter-rotating coupling terms between the quantum dots and the ferromagnet. Numerical analysis of the time evolution of the system demonstrates coherent switching between the qubit states with limited leakage to states outside the qubit subspace. Furthermore, through the Schrieffer-Wolff transformation, we derive an effective low-energy Hamiltonian for ferromagnets in which the magnon energy is significantly larger than the qubit splitting energy, and confirm numerically that the obtained effective Hamiltonian accurately reproduces the dynamics of the original Hamiltonian.

In the regime where both the magnon energy and the externally applied magnetic field is significantly larger than the qubit splitting energy, we derive expressions for the effective terms describing the coupling between the qubit states and the leakage to states outside the qubit subspace. Using these terms, we show that the rotating and counter-rotating terms may be tuned in such a way that the leakage terms are completely suppressed within the effective Hamiltonian. Finally, we show numerically that this tuning of the coupling parameters indeed results in significantly reduced leakage for the full system Hamiltonian.

Sammendrag

Utviklingen mot realiseringen av kvantedatamaskiner er avhengig av forståelsen og utviklingen av passende fysiske systemer hvor kvantebits kan konstrueres. Å møte kravene for et slikt system er dog en betydelig forskningsutfordring. Kvantebits må være pålitelige og robuste i møte med støy, enkle å manipulere, og være skalerbare nok til å kunne danne kraftige kvanteprosessorer. Til tross for betydelig framgang i senere år gjenstår det fortsatt å finne et kvantebitdesign som møter disse kravene godt nok til applikasjoner innen kvanteinformasjonsteknologi. Den videre utviklingen innenfor feltet er dermed avhengig av å finne nye systemer for å konstruere og sammenkoble kvantebits. Et lovende område er hybridsystemer hvor vi kan benytte oss av kombinasjoner av egenskapene til individuelle undersystemer.

I denne mastergradsavhandlingen undersøker vi et slikt potensielt system: singlett-triplett kvantebits konstruert i doble kvanteprikker, sammenkoblet gjennom utvekslingskobling til en ferromagnet. Gjennom en kombinert analytisk og numerisk analyse evaluerer vi dette systemets potensial til å gjennomføre mellomavstands koherent og tapsfri sammenkobling av to kvantebits.

Vi utleder Hamilton-operatoren for det kombinerte systemet, inkludert magnetisk anisotropi, og viser at denne anisotropien gir opphav til justerbare roterende og motroterende koblingselementer mellom kvanteprikkene og ferromagneten. Numerisk analyse av tidsutviklingen til systemet demonstrerer koherent veksling med begrenset lekkasje til kvantetilstander utenfor kvantebitunderromet. Videre, gjennom en Schrieffer-Wolff transformasjon, utleder vi en lav-energi effektiv Hamilton-operator for magneter hvor magnonenergien er betydelig større enn energiforskjellen i kvantebiten, og bekrefter numerisk at denne effektive Hamilton-operatoren presist gjenskaper dynamikken til den originale Hamilton-operatoren.

I et regime hvor både magnonenergien og det eksternt påtrykte magnetfeltet er betydelig større enn energiforskjellen i kvantebiten utleder vi uttrykk for de effektive koblingselementene mellom kvantebittilstandene så vel som lekkasjeelementene til tilstander utenfor kvantebitunderromet. Ved hjelp av disse uttrykkene viser vi at de roterende og motroterende koblingskonstantene kan justeres slik at lekkasjeelementene er fullstendig eliminerte. Avslutningsvis viser vi numerisk at denne justeringen av koblingskonstantene resulterer i betraktelig redusert lekkasje for Hamilton-operatoren til det fullstendige systemet.

Preface

This master's thesis is the culmination of a 5-year Master's Degree in Nanotechnology at the Norwegian University of Science and Technology. The work presented herein was conducted during the spring of 2022, at the Center for Quantum Spintronics, Department of Physics.

I would like to thank Prof. Jeroen Danon for introducing me to this fascinating field. His insight and feedback has been both enlightening and indispensable in the writing of this thesis.

This thesis builds on previous work done during a specialization project in the fall of 2021. The focus of this project was magnon-mediated coupling of single-spin qubits. Parts of this thesis is therefore directly reused from the specialization project report [1], with some revisions. This applies to Secs. 1, 2.3, 2.5 and 3, in particular. Large parts of the work conducted during both the thesis and the aforementioned project work has included programming in Python and Wolfram Mathematica. The Python code is included in Appendix A. The Wolfram Mathematica code is not appended in the thesis, but can be made avaliable upon request.

Contents

Chapter 1

Introduction

In the past few decades, much interest has been given to the theoretical description and experimental realization of a quantum computer. From Feynman's 1982 proposal that quantum problems would be efficiently solved by a computer operating on quantum principles [2], to recent demonstrations of apparent quantum supremacy for certain computational tasks [3], much progress has already been made. The prospects of implementing significantly improved algorithms for data searches and prime factorization, developed by Grover [4] and Shor [5] respectively, allow for quantum computers to solve problems that are believed to be intractable for even the most powerful conventional computers. Furthermore, realizing quantum computation may provide an opportunity to handle the incredibly complex problems in quantum chemistry and solid state physics [6].

Despite intense research focus, however, quantum computers have yet to be realized on a practical scale. This is due to some significant challenges that need to be overcome, both in the design of the quantum computer and the engineering advances needed to implement said designs. These issues in large part relate to the fragility of quantum systems; current quantum computer designs are susceptible to noise, inducing errors in the computations that render the answers incorrect [7]. This challenge is being approached in two ways: by designing systems for quantum computation that are protected from noise, so that errors are less likely, and by designing systems that are able to detect and correct errors as they appear, thus reducing the likelihood of producing incorrect answers [8, 9]. At the core of any proposal to meet these challenges lies the quantum bit.

1.1 Quantum bits

As with the bits used in conventional computation, the fundamental building blocks in quantum computation are quantum bits, or qubits. In analogy with the state of a conventional bit, which may be either 0 or 1, a qubit is constructed from the quantum states $|0\rangle$ and $|1\rangle$[1]. Unlike a conventional bit, however, a qubit

[1]The brackets $|\ \rangle$ are the Dirac notation for quantum states, which will be used throughout the thesis. For an introduction to Dirac notation, see e.g. Berman's *Introductory Quantum*

is not restricted to existing in either state $|0\rangle$ or $|1\rangle$: it may exist in any state $|\chi\rangle$ that is a superposition of $|0\rangle$ and $|1\rangle$,

$$|\chi\rangle = \alpha\,|0\rangle + \beta\,|1\rangle\,, \tag{1.1}$$

where α and β may be any complex numbers such that $|\alpha|^2 + |\beta|^2 = 1$. Similarly to conventional bits, the qubit state must be read out to determine what state it is in. However, while the qubit state $|\chi\rangle$ need not be exactly $|0\rangle$ or $|1\rangle$, any measurement of the qubit state will return one of these states, with probability $|\alpha|^2$ or $|\beta|^2$, respectively. These probabilities may in turn be altered by manipulating the state of the qubit. By using the constraint $|\alpha|^2 + |\beta|^2 = 1$, and ignoring any overall phase factor, we may choose to rewrite the qubit state $|\chi\rangle$ in Eq. 1.1 as

$$|\chi(\theta,\phi)\rangle = \cos\frac{\theta}{2}\,|0\rangle + e^{i\phi}\sin\frac{\theta}{2}\,|1\rangle\,. \tag{1.2}$$

In this form we may view $|\chi(\theta,\phi)\rangle$ as a vector in a three-dimensional vector space defined by the angle θ and ϕ as well as the constraint $|\alpha|^2 + |\beta|^2 = 1$. Indeed, the set of all states $|\chi\rangle$ that may be described by Eq. 1.2 define a unit sphere, with θ and ϕ as the polar and azimuthal angles, respectively. This sphere is known as the Bloch sphere, and is shown in Fig. 1.1a. For a given state, θ contains information about the distribution of probability between $|\alpha|^2$ and $|\beta|^2$, while ϕ describes the phase of the state. The top and bottom of the Bloch sphere, or north and south poles, correspond to the $|0\rangle$ and $|1\rangle$ states, respectively [11]. Furthermore, unitary gate operations on a qubit may be represented by rotations around an axis on the sphere [12].

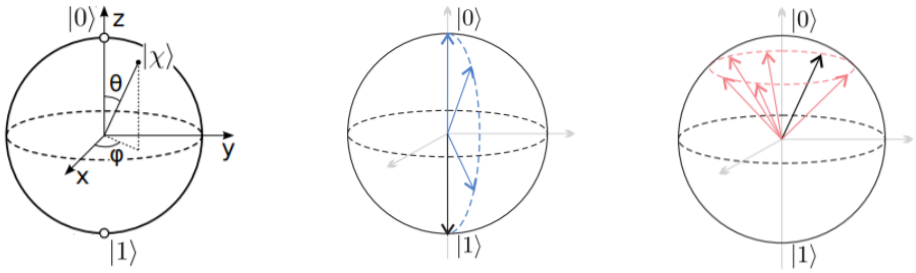

(a) **(b)** **(c)**

Figure 1.1: **a)** Bloch sphere denoting a qubit state $|\chi\rangle$. As seen from Eq. 1.2, θ and ϕ are the polar and azimuthal angles of the sphere, respectively. Here, the north pole denotes the $|0\rangle$-state, while the south pole denotes the $|1\rangle$-state. **b)** Bloch sphere illustrating how transversal noise may cause a qubit in the $|1\rangle$-state to relax, causing decoherence. **c)** Bloch sphere illustrating how longitudinal noise affects the phase angle ϕ, causing phase information to become lost. All figures adapted from [13].

The Bloch sphere is a useful tool for visualizing one of the most prolific challenges faced by potential qubits: decoherence in the form of either relaxation

Mechanics [10].

or dephasing [13]. Relaxation is the tendency of a qubit to dissipatively transition to the ground state. Dephasing refers to the loss of phase information; denoted by ϕ in Fig. 1.1a. In both cases, the decoherence is the result of noise in the physical system in which the qubit is encoded. While relaxation is a result of transversal noise, dephasing is a result of longitudinal noise.

In the context of the Bloch sphere, longitudinal noise gives rise to uncertainty in the splitting between the $|0\rangle$ and $|1\rangle$ states, that is, in the $\hat{\mathbf{z}}$-direction. Such noise affects the phase ϕ of the qubit state. To see this, consider for instance a qubit encoded in the energy splitting between the spin-up and spin-down states of an electron in a magnetic field. The applied magnetic field causes the spin to precess with a phase velocity proportional to the applied field. Therefore, any variation in the applied field, or equivalently, variations in the qubit splitting, gives rise to a variation in the phase velocity. This causes information about the phase of the qubit to become lost. Fig. 1.1c illustrates this process. Noise in the transverse (x,y) plane may instead cause the qubit to relax to its ground state. For instance, the operators that cause a spin to be excited or relax may be written as a combination of operators acting in the (x,y)-plane, $S_{\pm} = S_x \pm iS_y$ [14]. Similarly, pertubations in this plane may cause the qubit to relax by transferring its energy to the environment and transitioning to the ground state. Such a process is depicted in Fig. 1.1b.

In order to realize quantum computing, we need to be able to encode such qubits in physical systems with the desired properties. Again, an analogy to conventional bits is appropriate. These bits may for instance be encoded in current pulses through a transistor; if current is passing through the transistor, the state is 1. Otherwise, the state is zero [15].

Similarly, in order to physically construct a qubit we require a quantum system with two well defined states to represent $|0\rangle$ and $|1\rangle$ [16]. Simply finding such a system is not sufficient, however; for qubits to be able to perform computations, certain requirements must be met. Fundamental to the operation of a quantum computer is the "closed box" requirement; during operation the qubits must be as isolated from the environment as possible [17]. Only a small degree of unwanted interaction with the environment may cause the qubits to lose coherence and information to leak out of the system. However, this must simultaneously be balanced with the ability to easily and accurately control the qubits in order to perform actual computations. In order to evaluate the feasibility of a system to perform quantum computations, one may consider the five requirements proposed by DiVincenzo [18, 19]. First, the qubits should be well-defined within the Hilbert space[2] of the system, preferably in a Hilbert space that may be decomposed into direct products. Second, it must be possible to reliably initialize the system in a given state. Third, as stated above, the system must be sufficiently isolated from its environment as to limit decoherence. Fourth, it must be possible to perform gate operations as a sequence of unitary transformations of the system. Fifth and finally, it must be possible to measure the system in a way that accurately

[2]In quantum mechanics, the Hilbert space denotes the complex linear vector space in which a quantum state, in this case the state of the qubit, exists [20].

determines the outcome of the performed operations.

Various systems have been proposed, and to some extent realized, as potential qubits. These include collective excitations in superconductors, photonic modes, nitrogen vacancy centers in diamond, and in the quantum numbers of topologically non-trivial quasiparticle systems [21–24]. All these approaches come with their own set of advantages and disadvantages. In general, proposals building atomic, molecular and optical (AMO) physics, such as trapped ions and optical cavities, are able to manipulate qubits with a high degree of precision. Proposals built on solid-state physics, on the other hand, promise easier scalability and implemantation in quantum circuits [25]. In particular, spin qubits constructed in semiconductor quantum dots have been given much attention due to their potential to utilize the mature fabrication technology of semiconductor-based circuitry [26]. This proposal for realizing quantum computation will be the focus of this thesis.

1.2 Quantum-dot-based spin qubits

The idea of employing single electron spins in quantum dots to encode qubits, first proposed by Loss and DiVincenzo [19], has been given much attention due in part to its potential similarities to conventional semiconductor technologies. Even though early attempts at realizing quantom dot based spin qubits were based on gallium arsenide (GaAs) structures, the spin qubit design is still similar to conventional silicon-based semiconductor chips. As expanded upon in Sec. 1.2.2, silicon-based spin qubits have recently emerged as an attractive option due to its potentially nuclear-spin-free environment.

In the proposal by Loss and DiVincenzo, the $|0\rangle$ and $|1\rangle$ states are constructed from two opposite spin directions of an electron spin, denoted spin-up ($|\uparrow\rangle$) and spin-down ($|\downarrow\rangle$). As these spins are localized magnetic moments, they may be made to differ in energy by the Zeeman splitting imposed by an external magnetic field. The initial spin states may be produced by applying a uniform magnetic field at low temperatures and waiting for the spins to relax to the ground state. If an initial state where the spins are not all pointing in the same direction is needed, this can be accomplished by injecting the quantum dots with electrons that are already in the desired spin state for each dot, which may be done by using a spin filter that only admits electrons carrying specific spins. Alternatively, one may construct the desired algorithm to start with all spins in the ground state and use avaliable gates to manipulate the qubits into the desired configuration.

Single-qubit operations may be performed by subjecting the qubit to external fields in specific ways. An applied static magnetic field will cause an electron spin to precess around the $\hat{\mathbf{z}}$-axis of the Bloch sphere, with a frequency proportional to the strength of the applied field, the so-called Larmor frequency. For rotations around the $\hat{\mathbf{x}}$-axis, the qubit is exposed to a oscillating magnetic field perpendicular to the aforementioned static field. This field causes the spin to rotate around the $\hat{\mathbf{x}}$-axis with a frequency know as the Rabi frequency. Thus, by sequentially pulsing these fields for specific durations, full single-qubit control is accomplished [27].

Two-qubit gate operations are performed by lowering the electrostatic barrier between two quantum dots for a suitable time, allowing the spins to be coupled. Read out may be performed by allowing spins to tunnel either to a nearby paramagnetic dot, in which the spin would establish a measurable ferromagnetic domain, or through a spin valve to a secondary dot. In the latter case, if the spin valve for example permits only spin-up electrons, the presence of charge at the dot would indicate that the spin state in the qubit had indeed been spin-up. Since the original proposal by Loss and DiVincenzo, more convenient methods for read out have been proposed, for instance by using Pauli spin-blockade for spin-to-charge conversion before read out is performed [28, 29].

In conclusion, the Loss and DiVincenzo proposal, with a few modifications, should be a suitable platform to implement quantum computing. However, spin qubit based quantum computing is yet to be realized on a practical scale. This apparent lack of progress is due to a few key challenges in the realization of the proposal. As mentioned in Sec. 1.1, noise may cause the qubits to decohere during computation, so that any information is lost. In the case of quantum dot spin qubits, this may be due to unwanted interactions between the localized electron spins carrying the information and the ensemble of randomly fluctuating nuclear spins of the host semiconductor [30]. Furthermore, producing sufficiently precise oscillating magnetic fields to control such qubits is challenging, more so because the qubits must be closely packed in order to be able to interact [16]. The short range interaction also limits qubits to nearest neighbor coupling, reducing the flexibility of the setup. Finally, as the physical system in which a qubit is constructed is rarely a perfect two-level system, there may exist states that are coupled to the qubit states. Transitions to these states causes information to be lost from the qubit, which is referred to as *leakage* [31].

In the years since the Loss and DiVincenzo proposal, the efforts of the spin qubit field have been focused on overcoming these challenges. In the following three sections, some of the solutions that have been proposed in these efforts are presented.

1.2.1 Singlet-triplet spin qubits

In order to eliminate the necessity for localized oscillating magnetic fields, one can encode the qubit in a multi-electron state [32]. This may for instance be done by constructing a double quantum dot (DQD) system carrying a total of two excess electrons. We consider the potential landscape of such a system, shown as the solid blue lines in Fig. 1.2. The dotted orange lines may be ignored for now; they will be discussed below. The potential of each of the quantum dots is shown as a valley separated by a potential barrier. Within each valley there are states that the electrons, depicted as a black dots, may occupy. These states are depicted as horizontal lines.

In the case of a DQD system carrying a total of two excess electrons, assuming each electron is confined to different dots, there are four possible spin states: the spins may form a singlet or a triplet, and have different spin projections

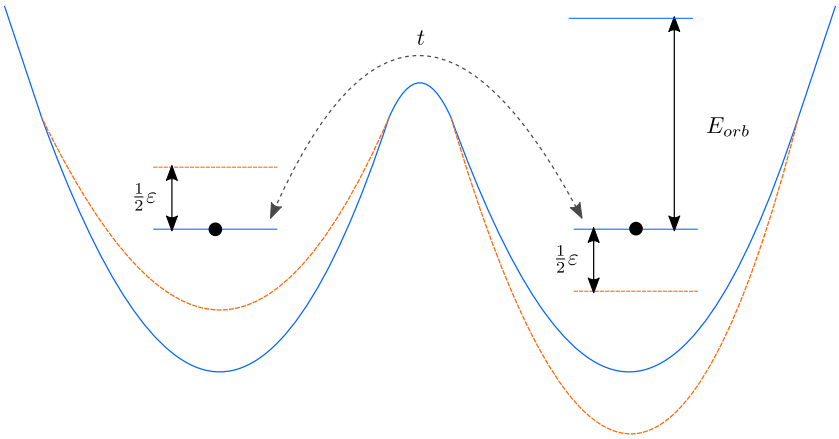

Figure 1.2: Sketch of the potential landscape of a DQD system hosting two electrons, the two valleys corresponding to the two quantum dots. The horizontal lines in each of the valleys denote available states that the electrons may occupy in each dot. The black dots on these lines depict electrons occupying said states. The electrons may transition between the two quantum dots through the tunnel coupling if they are able to overcome the potential barrier between the dots. This coupling is denoted by the dotted black line. Such a transition would transfer the system from the (1,1) charge configuration, as is depicted, to the (0,2) configuration. E_{orb} denotes the energy difference between the lowest and second lowest energy orbitals. The two dots may be subjected to a relative electrostatic potential, parametrized by ε. The solid blue line shows the potential for $\varepsilon = 0$, in which the energies of electrons occupying each of the dots are degenerate. The dotted orange lines show the same potential for non-zero ε. The shift in the potential landscape shifts the energies of the available states. Note that this figure is only a sketch; the differences in energy between the different states, as well as the height of the potential barrier do not correspond to physically relevant values.

[33]. With the indices denoting the electron spin being located in dots 1 and 2, respectively, this reads

$$\begin{aligned} |S\rangle &= \frac{1}{\sqrt{2}}(|\uparrow_1\downarrow_2\rangle - |\downarrow_1\uparrow_2\rangle) \\ |T_0\rangle &= \frac{1}{\sqrt{2}}(|\uparrow_1\downarrow_2\rangle + |\downarrow_1\uparrow_2\rangle) \\ |T_+\rangle &= |\uparrow_1\uparrow_2\rangle \\ |T_-\rangle &= |\downarrow_1\downarrow_2\rangle\,. \end{aligned} \tag{1.3}$$

Here, $|S\rangle$ ($|T_0\rangle$) is the singlet (triplet) with spin quantum number $m_s = 0$, while $|T_+\rangle$ and $|T_-\rangle$ have $m_s = \pm 1$. We refer to this configuration of electrons, with each electron in different dots, as the (1,1) charge configuration.

By careful application of the gate voltages on each dot, we may change the electrostatic potentials of the dots so that certain charge configurations are favorable. For instance, we may set these gate voltages such that the electron in dot 1 is allowed to tunnel to the second dot, so that the double dot system is in the (0,2) charge configuration [34]. In Fig. 1.2 the tunneling process is described

by the dotted black line. Transitions between charge configurations in principle preserve electron spin. Thus, if the two electrons are in different dots and have the same spin, any electron tunneling to the other dot would have to occupy a higher energy orbital in order to obey the Pauli principle. As shown in Fig. 1.2, the difference in energy between the ground state orbital and the excited orbital, E_{orb}, is quite large. In typical systems, E_{orb} is on the order of meV [28]. As long as the difference in electrostatic potential between the two dots is not too large, this leads to only the singlet state being populated in the (0,2) charge configuration:

$$|S_{02}\rangle = \frac{1}{\sqrt{2}}(|\uparrow_2\downarrow_2\rangle - |\downarrow_2\uparrow_2\rangle), \tag{1.4}$$

where the indices on the arrows indicate that both electron spins are located on the second dot.

Within the regime of gate voltages that favor the (1,1) and (0,2) charge configurations, we may alter the relative electrostatic potential between the dots, thereby altering the energy levels of the available states, while requiring the average of the energy levels of the two dots to remain unchanged [34]. This is referred to as *detuning* the dots, and will be described by the detuning parameter ε. The solid blue potential in Fig. 1.2, which we discussed above, depicts a system in the absence of detuning, that is, $\varepsilon = 0$. In dotted orange, however, we show the same potential for non-zero ε. By shifting the energy in the left dot by ε and the energy in the right by $-\varepsilon$, as shown, the average of the two naturally remain unchanged. Hence, the energies of the (1,1) states are unaffected by variations in the detuning parameter. The $|S_{02}\rangle$ state, however, with both electrons in a single dot, will have its energy altered.

The energy spectrum of a DQD system confined to the (1,1) or (0,2) configurations is shown in Fig. 1.3, as a function of the detuning parameter ε. The energies of the polarized triplet states $|T_+\rangle$ and $|T_-\rangle$ have been split by an applied magnetic field. These energies are depicted as the purple and blue horizontal lines in Fig. 1.3, respectively. The green horizontal line depicts the unpolarized triplet state $|T_0\rangle$, which, due to having equal parts spin-up and spin-down remains unaffected by the applied field. We observe that, as mentioned above, these states are unaffected by changes in the detuning parameter.

An electron in the (1,1) singlet $|S\rangle$ may tunnel to the other dot, transitioning to the (0,2) singlet $|S_{02}\rangle$, and vice versa. If the tunnel barrier between the two dots is high enough, however, the energy required for this transition to take place effectively decouples the two singlet states. If so, the (1,1) singlet will be degenerate with $|T_0\rangle$, both having equal parts spin-up and spin-down. Like the (1,1) singlet, the (0,2) singlet will be unaffected by the applied magnetic field, but its energy will vary with ε. The situation where tunnel coupling is prohibited corresponds to large values of $|\varepsilon|$ in Fig. 1.3. On both the far left and far right of the figure, the (1,1) singlet is degenerate with the unpolarized triplet, while the (0,2) singlet is a linear function of the detuning parameter.

As the detuning parameter is reduced, the tunnel coupling between the states becomes more important, and the states hybridize. This hybridization causes

the states to mix, and an exchange energy splitting J opens up between the unpolarized triplet and the singlet states, as depicted in Fig. 1.3. At this point, the eigenstates are not simply either the (1,1) or (0,2) singlet, but rather a superposition of the two. The qubit may then be encoded in the $|T_0\rangle$ state and in the low energy singlet eigenstate, that is, in the green and orange lines in Fig. 1.3. The qubit splitting energy, that is, the energy difference between the $|1\rangle$ and $|0\rangle$ states, then depends on the detuning parameter of the system, granting electrical control of this facet of the qubit.

Consider a Bloch sphere with the north and south poles defined as $|S\rangle$ and $|T_0\rangle$, respectively, the poles along the $\hat{\mathbf{x}}$-axis being the $|\uparrow\downarrow\rangle$ and $|\downarrow\uparrow\rangle$ states. This is consistent with setting $|0\rangle = |S\rangle$ and $|1\rangle = |T_0\rangle$. In this view, the pulsing of the exchange interaction between the electrons amount to a rotation of the qubit state around the $\hat{\mathbf{z}}$-axis of the Bloch sphere, so that the $|\uparrow\downarrow\rangle$ and $|\downarrow\uparrow\rangle$ states may be swapped [35]. While this manipulation method opens the qubits up to be affected by charge noise, this noise may be suppressed by operating them symmetrically [36].

Note that this does not amount to full control of the qubit; we still need to be able to perform rotations around an axis perpendicular to the $\hat{\mathbf{z}}$-axis. This may be accomplished by establishing a magnetic field gradient ΔB across the two dots [33].

1.2.2 Nuclear-spin-free spin qubits

While research into quantum dot based spin qubits in the beginning focused on III-V semiconductors such as GaAs, these host materials are disadvantaged by carrying non-zero nuclear spin. The large number of nuclei in the vicinity and the host material of the quantum dot set up an effective random magnetic field that acts on the electrons occupying the dot. Electrons coupling to the nuclear spin bath lowers the decoherence time of the qubit due to the random nature of the effective magnetic field. In response to this challenge, using group IV semiconductors such as silicon and germanium as host materials has become an increasingly attractive option [37]. These materials can be made nuclear spin free through isotopic purification, potentially increasing the coherence times of qubits significantly. Coherent control of singlet-triplet qubits in Si/SiGe heterostructures has been reported, with significantly longer coherence times than for similar GaAs structures [38].

A different approach to solve the same problem involves encoding qubits in a singlet-only subspace. This subspace is protected from nuclear spin induced decoherence as it does not interact with the fluctuating Zeeman fields of the nuclear spin bath [39]. Thus, by constructing a system of four electron spins, one may use the singlet-only subspace to encode the qubit. The basis states of this qubit are then [32]

$$\begin{aligned} |1\rangle &= |S_{14}S_{23}\rangle \\ |0\rangle &= \frac{1}{\sqrt{3}}(|S_{13}S_{24}\rangle + |S_{12}S_{34}\rangle), \end{aligned} \tag{1.5}$$

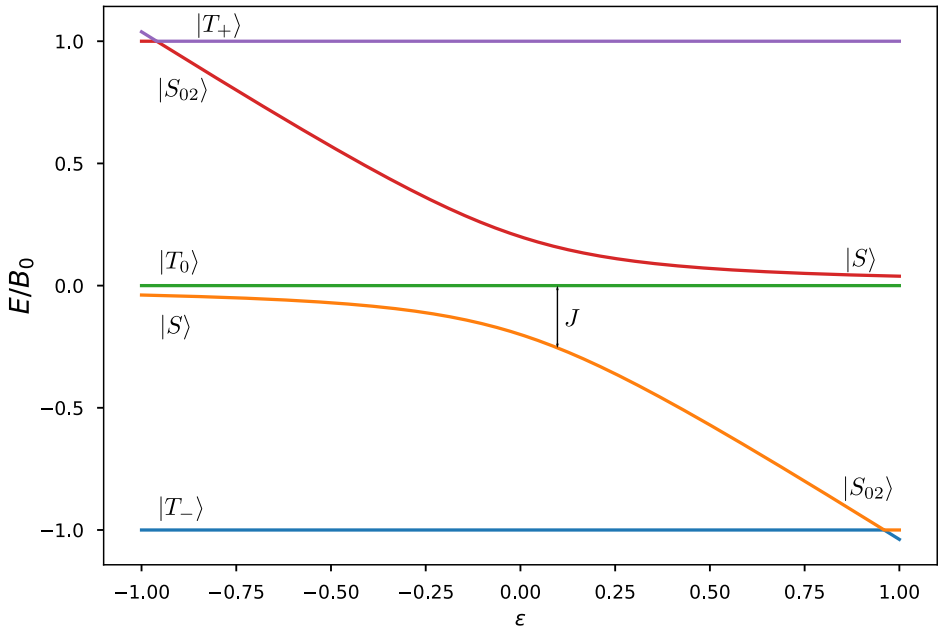

Figure 1.3: Typical energy spectrum of double quantum dot confined to the (1,1) or (0,2) charge configurations, as a function of the detuning parameter ε. The dots are subjected to a uniform external magnetic field $\mathbf{B} = B_0\hat{\mathbf{z}}$. The three horizontal lines, starting from the top, depict the energies of the $|T_+\rangle$ (purple), $|T_0\rangle$ (green), and $|T_-\rangle$ (blue) states, which are not affected by a change in the detuning. The two curved lines (red and orange) are superpositions of the $|S\rangle$ and $|S_{02}\rangle$ states. Of the (0,2) charge states, only $|S_{02}\rangle$ is included as the (0,2) triplet states are higher in energy. The tunnel coupling between the two dots is $t_c = 0.2B$.

where $|S_{ij}\rangle = \frac{1}{\sqrt{2}}(|\uparrow_i\downarrow_j\rangle - |\downarrow_i\uparrow_j\rangle)$. These states are not coupled by the nuclear field, so that the nuclear spin bath is not able to directly cause dephasing of the qubit, granting significantly improved decoherence times. Still, the nuclear field may couple these states to states that are not in the qubit subspace, causing information to leak out of the qubit.

1.2.3 Spin qubits with long range coupling

The exchange interaction between spin qubits is short range. It is therefore of significant interest to be able to extend spin qubit coupling distances to be able to reach beyond nearest neighbor interactions. One approach is through the use of microwave resonators. Here, two qubits are coupled through a superconducting cavity by tuning the qubit splittings of each qubit into resonance with one another and the electric field in the cavity. This has been reported to couple spins separated by distances over 4 millimeters [40]. While this clearly allows for long range qubit coupling, it also presents a challenge in terms of scalability. In a

future quantum processor potentially containing millions of qubits tightly packed together [16], only being able to couple qubits that are millimeters apart would be impractical.

Here, we focus on coupling spin qubits through magnons rather than microwave cavities. Magnons, being quasiparticles of the collective magnetization in a spin lattice, are able to transport spin information without necessitating charge transfer [41]. This has sparked interest in using ferromagnets to mediate the coupling between spin qubits. Such a coupling can extend the possible distance between qubits to the order of micrometers rather than nanometers [42].

In this thesis, we build on the understanding gained from previous work on quantum-dot-based single spin qubits, and study two singlet-triplet spin qubits hosted in double quantum dots coupled to an insulating ferromagnet through the exchange interaction. This hybrid platform, combining the well known and well understood subjects of insulating ferromagnets and double quantum dot-based spin qubits, offers a promising path to overcome some of the challenges faced by contemporary quantum computing. Specifically, we are interested in the potential of this platform to realize coherent qubit-qubit coupling over intermediate distances, with little to no leakage to states outside the qubit subspace. The potential is due in large part to the tunability of the system, both through electrical control of the singlet-triplet qubits and through the tunability of the ferromagnetic coupling of the qubits. We investigate this potential through a theoretical derivation of the system Hamiltonian, which will form the basis for both numerical and perturbative analysis of the dynamics of the proposed system. Through the application of the Schrieffer-Wolff transformation, we obtain effective terms describing coupling between the qubits, as well as leakage out of the qubit subspace.

1.3 Structure of the thesis

In the upcoming chapter 2, we present some fundamental tools and theory to be used in the remainder of the thesis. This includes a brief description of the quantum harmonic oscillator in section 2.1 followed by an overview of the concept of qudrature squeezing of bosonic modes in section 2.2. section 2.3 presents the Holstein-Primakoff transformation of spin operators in ferromagnets. The chapter concludes with two related methods in perturbation theory; section 2.4 reviews time independent perturbation theory to second order, while section 2.5 presents the main tool to be used in the perturbative analysis in the thesis: the Schrieffer-Wolff transformation.

In chapter 3 the Hamiltonian for a ferromagnetically coupled single spin qubit system is derived. The derivation is performed by splitting the system Hamiltonian into three parts that may be individually treated. Thus, in section 3.1 we consider the Hamiltonian of a single spin qubit. In section 3.2 we consider the Hamiltonian of an insulating ferromagnet, both in the presence and absence of anisotropy. In section 3.3 we consider the interaction between the two preceding

subsystems. With the full single spin Hamiltonian derived, section 3.4 presents a numerical analysis of the system dynamics.

Having established the framework for a coupled single spin Hamiltonian, chapter 4 proceeds by considering a ferromagnetically coupled double quantum dot system. As in chapter 3 we consider a tripartite Hamiltonian. This derivation is performed using two different bases for the double quantum dot Hamiltonian, and includes the derivation of effective Hamiltonians using the Schrieffer-Wolff transformation.

Chapter 5 considers the dynamics of ferromagnetically coupled double quantum dots using a similar numerical analysis as in section 3.4. In section 5.2 we compare the numerical simulations of the full system Hamiltonian to the results obtained using the effective Hamiltonian, and consider in detail the terms describing the coupling strength and leakage of the coupled double quantum dot system.

Chapter 2

Preliminary Concepts

The purpose of this chapter is to present some tools and concepts that will be important in the remainder of the thesis. It begins by considering the quantum harmonic oscillator before continuing with the subject of quadrature squeezing of bosonic modes. We briefly present the Holstein-Primakoff transformation of spin operators in ferromagnets. The final two sections are dedicated to two variants of perturbation theory: time independent perturbation theory to second order, and the Schrieffer-Wolff transformation to second and fourth order.

2.1 Quantum harmonic oscillator

We begin by considering one of the simplest, yet most important systems in quantum mechanics; the quantum harmonic oscillator. As we will see, an understanding of this system will be useful both in the description of quadrature squeezing in the following section and in the description of magnon excitations in a ferromagnet in Sec. 3.2.

Similarly to the well known classical harmonic oscillator, we may write the Hamiltonian of a single-mode quantum harmonic oscillator as

$$\hat{H} = \frac{\hat{p}^2}{2m} + \frac{m\omega^2\hat{q}^2}{2}, \tag{2.1}$$

where the operators $\hat{p}$ and $\hat{q}$ are momentum and position operators, respectively [43, p.84]. The angular frequency of the harmonic oscillator, ω, is defined as in the classical case, $\omega = \sqrt{k/m}$. Rather than solving the Schrödinger equation for the Hamiltonian in Eq. 2.1, it is helpful to define the operators

$$\begin{aligned} \hat{a} &= \sqrt{\frac{m\omega}{2\hbar}}\left(\hat{q} + i\frac{\hat{p}}{m\omega}\right) \\ \hat{a}^\dagger &= \sqrt{\frac{m\omega}{2\hbar}}\left(\hat{q} - i\frac{\hat{p}}{m\omega}\right). \end{aligned} \tag{2.2}$$

With these operators, we may rewrite Eq. 2.1 as

$$\hat{H} = \hbar\omega\left(\hat{a}^\dagger\hat{a} + \frac{1}{2}\right). \tag{2.3}$$

We may now define the number operator $\hat{n} = \hat{a}^\dagger \hat{a}$ along with its eigenvalues n, obtained through $\hat{n}\,|n\rangle = n\,|n\rangle$. It follows that the eigenenergies of Eq. 2.3 are

$$E_n = \hbar\omega\Big(n + \frac{1}{2}\Big). \tag{2.4}$$

It can be shown that the operators $\hat{a}^\dagger$ and $\hat{a}$ act on the eigenstates as [43, p.85]

$$\begin{aligned} \hat{a}\,|n\rangle &= \sqrt{n}\,|n-1\rangle \\ \hat{a}^\dagger\,|n\rangle\,\sqrt{n+1}\,|n+1\rangle\,, \end{aligned} \tag{2.5}$$

where n is a non-negative integer. This, along with the eigenenergies obtained in Eq. 2.4, allows us to interpret the operators $\hat{a}^\dagger$ and $\hat{a}$ as creating and annihilating excitations of an energy quantum, denoted by n, with which the system exceeds the zero-point energy $E_0 = \frac{1}{2}\hbar\omega$. For these operators we obtain

$$\Big[\hat{a}, \hat{a}^\dagger\Big] = \frac{i}{2\hbar}([p, x] - [x, p]) = 1. \tag{2.6}$$

We also note that $[\hat{a}, \hat{a}] = \Big[\hat{a}^\dagger, \hat{a}^\dagger\Big] = 0$. From this we may conclude that the excitations described by the operators $\hat{a}$ and $\hat{a}^\dagger$ follow bosonic commutation relations.

The states $|n\rangle$, known as Fock states, are important states in quantum field theory. By describing a quantized field, such as the electromagnetic field, as an infinite array of decoupled harmonic oscillators, the Fock state $|n\rangle$ represents a state with exactly n excitations of the energy quantum $\hbar\omega$. In Sec. 3.2, this representation will be used to describe magnons as excitations of the magnetization field of a ferromagnet.

2.2 Quadrature squeezing

Quadrature squeezing is a well-known concept in quantum optics, wherein it refers to the reduction in uncertainty of either the photonic momentum or position operator at the expense of increased uncertainty of the other. The concept is not exclusively applicable to photons, however, but may be applied to any bosonic mode. In Sec. 3.2 we will use the theory derived in this section to consider squeezing of the aforementioned magnons, as these excitations follow bosonic commutation relations.

We begin by constructing dimensionless versions of the position and momentum operators of the quantum harmonic oscillator as written in Eq. 2.1,

$$\begin{aligned} \hat{X}_1 &= \frac{1}{2}\Big(\hat{a} + \hat{a}^\dagger\Big) \\ \hat{X}_2 &= \frac{1}{2i}\Big(\hat{a} - \hat{a}^\dagger\Big), \end{aligned} \tag{2.7}$$

where the operators $\hat{a}$ and $\hat{a}^\dagger$ are the ladder operators of the quantum harmonic oscillator as defined in Eq. 2.2. The dimensionless operators $\hat{X}_{1,2}$ are so-called quadrature operators, obeying the commutation relation

$$\left[\hat{X}_1, \hat{X}_2\right] = \frac{i}{2}. \tag{2.8}$$

The term *quadrature* stems from the original use in classical optics, in which the operators $\hat{X}_1$ and $\hat{X}_2$ are the real and imaginary parts of a phasor, and are a quarter cycle (90°) out of phase with one another [44]. Following a generalization of the well known Heisenberg uncertainty principle [45], the uncertainty in the simultaneous measurement of two operators $\hat{A}$ and $\hat{B}$ may be written [46]

$$\Delta\hat{A}\Delta\hat{B} = \frac{1}{2}|\hat{C}|, \tag{2.9}$$

where $\hat{C} = \left[\hat{A}, \hat{B}\right]$ is the commutator of the aforementioned operators. The uncertainty in the quadrature operators thus follow the relation

$$\langle(\Delta\hat{X}_1)^2\rangle\langle(\Delta\hat{X}_2)^2\rangle \geq \frac{1}{16}, \tag{2.10}$$

where the uncertainty is defined as $\Delta\hat{X}_i = \sqrt{\left\langle\hat{X}_i^2\right\rangle - \left\langle\hat{X}_i\right\rangle^2}$ and $\left\langle\hat{X}_i\right\rangle$ is the expectation value of the operator $\hat{X}_i$ for $i = 1, 2$.

States where this uncertainty is uniformly distributed across the two quadratures, so that $\langle(\Delta\hat{X}_j)^2\rangle = \frac{1}{4}$ for $j = 1, 2$, are known as *coherent*. If, on the other hand, either $\langle(\Delta\hat{X}_1)^2\rangle < \frac{1}{4}$ or $\langle(\Delta\hat{X}_2)^2\rangle < \frac{1}{4}$, the state is said to be *squeezed*. That is, a squeezed state has lower uncertainty than the coherent state in one of the quadratures, at the cost of a corresponding increase in the uncertainty of the other quadrature maintaining the relation in Eq. 2.10.

Such states may be generated by acting on a non-squeezed state with the squeeze operator $\hat{S}(\xi)$, defined as

$$\hat{S}(\xi) = \exp\left[\frac{1}{2}\left(\xi^*\hat{a}^2 - \xi(\hat{a}^\dagger)^2\right)\right], \tag{2.11}$$

with $\xi = r\, e^{i\theta}$, where the squeeze parameter r is real and positive and $0 \leq \theta \leq 2\pi$. Note that $\hat{S}(\xi)$ is unitary and obeys $\hat{S}^\dagger(\xi) = \hat{S}(-\xi)$. In order to be able to evaluate the expectation values of the $\hat{a}$-operators, and subsequently determine the variances of $\hat{X}_1$ and $\hat{X}_2$, we use the Baker-Hausdorf lemma to obtain

$$\begin{aligned}\hat{S}^\dagger(\xi)\hat{a}\hat{S}(\xi) &= \hat{a}\cosh r - \hat{a}^\dagger e^{i\theta}\sinh r \\ \hat{S}^\dagger(\xi)\hat{a}^\dagger\hat{S}(\xi) &= \hat{a}^\dagger\cosh r - \hat{a}e^{-i\theta}\sinh r.\end{aligned} \tag{2.12}$$

Considering the vacuum state, which we denote $|0\rangle$, we construct the squeezed vacuum state $|\xi\rangle = \hat{S}(\xi)\,|0\rangle$. For this state, we obtain the variances

$$\begin{aligned}\langle(\Delta\hat{X}_1)^2\rangle &= \frac{1}{4}\left[\cosh^2 r + \sinh^2 r - 2\sinh r\cosh r\cos\theta\right] \\ \langle(\Delta\hat{X}_2)^2\rangle &= \frac{1}{4}\left[\cosh^2 r + \sinh^2 r + 2\sinh r\cosh r\cos\theta\right],\end{aligned} \tag{2.13}$$

which, for $\theta = 0$ reduces to

$$\begin{aligned} \langle (\Delta \hat{X}_1)^2 \rangle &= \frac{1}{4} e^{-2r} \\ \langle (\Delta \hat{X}_2)^2 \rangle &= \frac{1}{4} e^{2r}. \end{aligned} \tag{2.14}$$

As $r > 0$, this implies that the uncertainty in the $\hat{X}_1$ quadrature is squeezed, that is, reduced at the expense of the uncertainty in the $\hat{X}_2$ quadrature [47]. This is visualized in Fig. 2.1, showing en error ellipse for $\theta = 0$. As we can see, the distribution of uncertainty is smaller in $\hat{X}_1$ than in $\hat{X}_2$.

2.3 Holstein-Primakoff transformation

In order to make spin operators in ferromagnets more tractable, it is helpful to express them in terms of bosonic operators describing fluctuations about the classical ground state of the magnet. Assuming the ground state magnetization to be along $\hat{\mathbf{z}}$, the spin component along the $\hat{\mathbf{z}}$ direction at each lattice site is the spin quantum number S. This spin moment may be reduced by fluctuations in the ground state, which we include as bosonic excitations with spin-1 in the $-\hat{\mathbf{z}}$ direction. In this view, the $\hat{\mathbf{z}}$-component of the spin at each lattice site in the ferromagnet may be written

$$S_i^z = S - \hat{a}_i^\dagger \hat{a}_i, \tag{2.15}$$

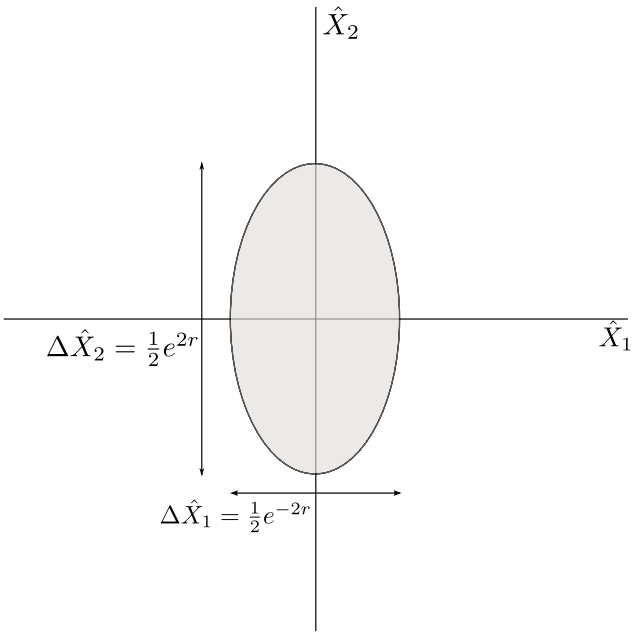

Figure 2.1: Ellipse showing the distribution of uncertainty of the squeezed vacuum state for $\theta = 0$. The squeezing is in the $\hat{X}_1$ quadrature, lowering the uncertainty at the expense of an increased uncertainty in the $\hat{X}_2$ quadrature. For the pure vacuum state, the ellipse would be a circle. Figure adapted from [47].

where $\hat{a}_i^\dagger$ and $\hat{a}_i$ are creation and annihilation operators of the spin-1 bosons, similar to the ladder operators of the quantum harmonic oscillator discussed in Sec. 2.1 [48].

Recalling the discussion of Fock states in Sec. 2.1, we may understand Eq. 2.15 as expressing the fluctuations about the ordered ground state as quantized excitations in the magnetization field of the ferromagnet. These excitations are known as magnons, and will be further considered in Sec. 3.2.

Consider now the $\hat{\mathbf{x}}$ and $\hat{\mathbf{y}}$ components of the spin operator, S_i^x and S_i^y. It is convenient to express these components through spin excitation and relaxation operators $S_i^+ = S_i^x + iS_i^y$ and $S_i^- = S_i^x - iS_i^y$. Through the Holstein-Primakoff transformation, these may be expressed in terms of the aforementioned bosonic operators as [49]

$$\begin{aligned} S_i^+ &= \sqrt{2S}\left(1 - \frac{\hat{a}_i^\dagger \hat{a}_i}{2S}\right)^{\frac{1}{2}} \hat{a}_i \\ S_i^- &= \hat{a}_i^\dagger \sqrt{2S}\left(1 - \frac{\hat{a}_i^\dagger \hat{a}_i}{2S}\right)^{\frac{1}{2}}. \end{aligned} \tag{2.16}$$

This is the Holstein-Primakoff transformation of spin operators. In cases where the spin system is nearly ordered, for instance at low temperatures, the number of excitations around the classical ground state is small. We may then assume $\langle \hat{n}_i \rangle = \left\langle \hat{a}_i^\dagger \hat{a}_i \right\rangle \ll S$, so that the second term within the parentheses above may be discarded. Thus, we approximate the spin excitation and relaxation operators as [50]

$$\begin{aligned} S_i^+ &\approx \sqrt{2S}\hat{a}_i \\ S_i^- &\approx \sqrt{2S}\hat{a}_i^\dagger. \end{aligned} \tag{2.17}$$

2.4 Time independent perturbation theory

As a primer to the main pertrubative tool used in the thesis, the Schrieffer-Wolff transformation, we include a short description of the more familiar time independent perturbation theory to first and second order. As we shall see in Sec. 2.5, the theories are closely related. Consider a system described by a Hamiltonian that may be written as a sum of an unperturbed Hamiltonian $\hat{H}_0$ and the perturbation $\hat{V}$

$$\hat{H} = \hat{H}_0 + \hat{V}, \tag{2.18}$$

where the eigenstates $\left|n^{(0)}\right\rangle$ and eigenenergies $E_n^{(0)}$ of the unperturbed Hamiltonian is assumed to be known. We now attempt to obtain the eigenstates and eigenenergies of the full Hamiltonian including the perturbation by solving

$$\left(\hat{H}_0 + \lambda \hat{V}\right)|n\rangle = E_n |n\rangle, \tag{2.19}$$

where λ is a book-keeping parameter introduced to keep track of the order of the perturbation as we proceed to expand the eigenenergies and eigenstates in

powers of λ. Doing so, we may write Eq. 2.19 as

$$\left(\hat{H}_0 + \lambda\hat{V} - E_n^{(0)} - \lambda E_n^{(1)} - \lambda^2 E_n^{(2)} - ...\right)\left(\left|n^{(0)}\right\rangle + \lambda\left|n^{(1)}\right\rangle + \lambda^2\left|n^{(2)}\right\rangle + ...\right) = 0. \tag{2.20}$$

For the above equation to be valid for any λ, it has to hold for each power of λ. This allows us to obtain the following set of equations, retaining terms to $\mathcal{O}(\lambda^2)$:

$$\begin{aligned} &\mathcal{O}\left(\lambda^1\right) : \left(\hat{H}_0 - E_n^{(0)}\right)\left|n^{(1)}\right\rangle + \left(\hat{V} - E_n^{(1)}\right)\left|n^{(0)}\right\rangle = 0 \\ &\mathcal{O}\left(\lambda^2\right) : \left(\hat{H}_0 - E_n^{(0)}\right)\left|n^{(2)}\right\rangle + \left(\hat{V} - E_n^{(1)}\right)\left|n^{(1)}\right\rangle - E_n^{(2)}\left|n^{(0)}\right\rangle = 0, \end{aligned} \tag{2.21}$$

where the equation for $\mathcal{O}(\lambda^0)$ has been omitted as it is true by assumption. We can obtain the first order correction to the energy by multiplying the first order equation above with $\left\langle n^{(0)}\right|$ from the left, yielding

$$E_n^{(1)} = \left\langle n^{(0)}\middle|\hat{V}\middle|n^{(0)}\right\rangle. \tag{2.22}$$

Similarly, we can obtain the first order correction to the eigenstates by multiplying the same equation from the left with $\left\langle m^{(0)}\right|$, where $m \neq n$ and using that $\left|n^{(1)}\right\rangle = \sum_m \left|m^{(0)}\right\rangle\left\langle m^{(0)}\middle|n^{(1)}\right\rangle$, yielding

$$\left|n^{(1)}\right\rangle = \sum_m \frac{\left\langle m^{(0)}\middle|\hat{V}\middle|n^{(0)}\right\rangle}{E_n^{(0)} - E_m^{(0)}}\left|m^{(0)}\right\rangle. \tag{2.23}$$

Note that due to the denominator in the above expression, this only holds for non-degenerate states. The second order correction to the energy levels may be obtained by multiplying the second order equation in Eq. 2.21 with $\left\langle n^{(0)}\right|$ from the left, just as in the first order case. Inserting the result for $\left|n^{(1)}\right\rangle$ from Eq. 2.23 yields [20]

$$E_n^{(2)} = \sum_m \frac{\left|\left\langle m^{(0)}\middle|\hat{V}\middle|n^{(0)}\right\rangle\right|^2}{E_n^{(0)} - E_m^{(0)}}. \tag{2.24}$$

2.5 Schrieffer-Wolff transformation

In chapters 3 and 4 we will consider the Hamiltonians of systems with qubits coupled to a ferromagnet. The ferromagnet in these systems is in principle able to host any number of magnons up to $2SN$, where N is the number of lattice sites in the magnet , as this would entail that all spins are completely flipped. For any realistic ferromagnet, N is a rather large number, making the full Hilbert space of any Hamiltonian describing it intractably large. It is therefore of interest to be able to separate the lower energy blocks in the Hamiltonian into an effective Hamiltonian, whilst retaining coupling to higher energy states. This may be achieved by employing a Schrieffer-Wolff (SW) transformation: a unitary transformation to decouple energy-separated blocks in a Hamiltonian [51].

The SW transformation is performed by separating the Hamiltonian into a block diagonal part $\hat{H}_0$ and a block off-diagonal perturbative part $\hat{V}$, so that the Hamiltonian is written

$$\hat{H} = \hat{H}_0 + \lambda\hat{V}, \tag{2.25}$$

where λ is a small perturbation parameter. The unperturbed Hamiltonian is a matrix on the form

$$\hat{H}_0 = \begin{pmatrix} \hat{H}_0^{(1)} & 0 \\ 0 & \hat{H}_0^{(2)} \end{pmatrix}, \tag{2.26}$$

where $\hat{H}_0^{(1)}$ and $\hat{H}_0^{(2)}$ denote Hamiltonians of two subspaces that are separated in energy from one another. Similarly, the perturbative part of the Hamiltonian is of the form

$$\hat{V} = \begin{pmatrix} 0 & \hat{V}_{12} \\ \hat{V}_{21} & 0 \end{pmatrix}, \tag{2.27}$$

so that the perturbation $\hat{V}$ couples the blocks of the unperturbed Hamiltonian H_0 [33, Appendix A]. For the leading order result of the transformation to be accurate, the eigenenergies of $\hat{H}_0^{(1)}$ may be degenerate on their own, but must differ from the eigenenergies of $\hat{H}_0^{(2)}$ so that any coupling element between states in the different subspaces is smaller than the energy differences between the states, $|\hat{V}_{ij}| \ll |E_i - E_j|$, where E_i and E_j denote eigenenergies in different subspaces. Note that, as the original Hamiltonian is hermitian, $\hat{V}_{12} = \hat{V}_{21}^\dagger$ is required.

This Hamiltonian is then subjected to a unitary transform U so that all block off-diagonal terms in the Hamiltonian are cancelled. The transformation is often expressed through $U = e^S$, where S is termed the generator of the transformation.

The effective Hamiltonian is written $\tilde{H} = U\hat{H}U^\dagger = e^S\hat{H}e^{-S} = e^S(\hat{H}_0+\lambda\hat{V})e^{-S}$, with λ as a perturbation parameter. The rotated Hamiltonian $\tilde{H}$ now acts in a Hilbert space spanned by the transformed basis states $\left|\tilde{\psi}\right\rangle = e^S\left|\psi\right\rangle$, where $|\psi\rangle$ are the basis states of the Hamiltonian before the transformation. For the transform to be unitary, the generator S is required to be skew-hermitian, $S = -S^\dagger$. Furthermore, S is expressed as a power series in λ, $S = \sum_{n=0}^{\infty}\lambda^n S_n$. Expanding the generator S and retaining terms to $\mathcal{O}(\lambda^2)$, the transformation becomes

$$\tilde{H} = (I + \lambda S_1 + \lambda^2 S_2 + \frac{\lambda^2}{2}S_1^2)(\hat{H}_0 + \lambda\hat{V})(I - \lambda S_1 - \lambda^2 S_2 + \frac{\lambda^2}{2}S_1^2). \tag{2.28}$$

Expanding this expression, again to $\mathcal{O}(\lambda^2)$, results in

$$\begin{aligned} \tilde{H} = {} & \hat{H}_0 \\ & + \lambda(\hat{V} + S_1\hat{H}_0 - \hat{H}_0 S_1) \\ & + \lambda^2(S_1\hat{V} - \hat{V}S_1 + S_2\hat{H}_0 - \hat{H}_0 S_2 + \frac{1}{2}S_1^2\hat{H}_0 + \frac{1}{2}\hat{H}_0 S_1^2 - S_1\hat{H}_0 S_1) \end{aligned} \tag{2.29}$$

Grouping the terms in Eq. 2.29 into commutators we arrive at

$$\tilde{H} = \hat{H}_0 + \lambda\hat{V} + \lambda\Big[S_1, \hat{H}_0\Big] + \lambda^2\Big[S_1, \hat{V}\Big] + \lambda^2\Big[S_2, \hat{H}_0\Big] + \frac{\lambda^2}{2}\Big[S_1, \Big[S_1, \hat{H}_0\Big]\Big]. \tag{2.30}$$

For $\tilde{H}$ to be block diagonal to first order in the perturbation, we need to cancel the block off-diagonal perturbation $\hat{V}$. Thus, setting $\lambda = 1$, we require

$$\left[S_1, \hat{H}_0\right] = -\hat{V}. \tag{2.31}$$

Furthermore, we ensure that the $\left[S_2, \hat{H}\right]$-term does not give any block off-diagonal contributions by letting $S_2 = 0$. Inserting this into Eq. 2.30 simplifies the expression into

$$\tilde{H} = \hat{H}_0 + \frac{1}{2}\left[S_1, \hat{V}\right]. \tag{2.32}$$

From Eq. 2.32 we may observe that S_1, in addition to being skew-hermitian, must be block off-diagonal for $\tilde{H}$ to be block diagonal. The effective Hamiltonian $\tilde{H}$ is now on the form

$$\tilde{H} = \begin{pmatrix} \tilde{H}_0^{(1)} & 0 \\ 0 & \tilde{H}_0^{(2)} \end{pmatrix}, \tag{2.33}$$

so that the blocks $\tilde{H}_0^{(1)}$ and $\tilde{H}_0^{(2)}$ are decoupled. This allows us to consider for instance $\tilde{H}_0^{(1)}$ independently, without having to consider the subspace described by $\tilde{H}_0^{(2)}$. The generator S_1 may be determined from Eq. 2.31. For each element in S_1, $\hat{H}_0$ and $\hat{V}$,

$$\sum_k \left[\hat{H}_{0,ik} S_{1,kj} - S_{1,ik}\hat{H}_{0,kj}\right] = \hat{V}_{ij}. \tag{2.34}$$

If the unperturbed Hamiltonian is diagonal, each element may be written as $\hat{H}_{0,ij} = E_i\delta_{ij}$, where E_i are the diagonal elements 0f $\hat{H}_0$. Thus,

$$S_{1,ij} = \frac{\hat{V}_{ij}}{E_i - E_j}. \tag{2.35}$$

Inserting this into Eq. 2.32, we obtain an expression for each element of the transformed Hamiltonian

$$\tilde{H}_{ij} = \hat{H}_{0,ij} + \frac{1}{2}\sum_k \left[\frac{\hat{V}_{ik}\hat{V}_{kj}}{E_i - E_k} + \frac{\hat{V}_{ik}\hat{V}_{kj}}{E_j - E_k}\right]. \tag{2.36}$$

Consider the diagonal elements of Eq. 2.36, $\tilde{H}_{ii} = E_i + \frac{\hat{V}_{ik}\hat{V}_{ki}}{E_i - E_k}$. This correction to the unperturbed energy E_i is indeed the correction obtained in Eq. 2.24 through second order perturbation theory.

In certain contexts it is insufficient to compute the SW transformation to second order. To resolve this we may also compute the transformation to fourth order by once again expressing the generator as $S = \sum_{n=0}^{\infty}\lambda^n S_n$ and retaining terms to $\mathcal{O}(\lambda^4)$. This yields a transformed Hamiltonian

$$\begin{aligned}\tilde{H} = \hat{H} &+ \left[S, \hat{H}\right] + \frac{1}{2}\left[S, \left[S, \hat{H}\right]\right] \\ &+ \frac{1}{6}\left[S, \left[S, \left[S, \hat{H}\right]\right]\right] \\ &+ \frac{1}{24}\left[S, \left[S, \left[S, \left[S, \hat{H}\right]\right]\right]\right] + \mathcal{O}\left(\lambda^5\right).\end{aligned} \tag{2.37}$$

We now insert $\hat{H} = \hat{H}_0 + \lambda\hat{V}$ and simplify to obtain

$$\begin{aligned}\tilde{H} = \hat{H}_0 &+ \frac{\lambda^2}{2}\Big[S_1, \hat{V}\Big] \\ &+ \lambda^3\Big(\frac{1}{3}\Big[S_1, \Big[S_1, \hat{V}\Big]\Big] + \Big[S_3, \hat{H}_0\Big]\Big) \\ &+ \frac{\lambda^4}{2}\Big(\Big[S_3, \hat{V}\Big] + \frac{1}{4}\Big[S_1, \Big[S_1, \Big[S_1, \hat{V}\Big]\Big]\Big] + \Big[S_1, \Big[S_3, \hat{H}_0\Big]\Big]\Big),\end{aligned} \tag{2.38}$$

where we require that $\Big[S_1, \hat{H}_0\Big] = -\hat{V}$ and $\Big[S_3, \hat{H}_0\Big] = -\frac{1}{3}\Big[S_1, \Big[S_1, \hat{V}\Big]\Big]$. As in the second order transition, we have set $S_2 = 0$. Furthermore, as S_4 carries a contribution of $\mathcal{O}(\lambda^4)$ on its own, it only appears in a single term in Eq. 2.37, said term being $\Big[S_4, \hat{H}\Big]$. Therefore, we have chosen $S_4 = 0$ in Eq. 2.38, for simplicity.

From the requirements above, we find that S_1 may be determined through Eq. 2.35, as in the second order SW transformation. Similarly, for a diagonal unperturbed Hamiltonian, we may obtain the thrid order component of the generator through

$$S_{3,ij} = \frac{X_{ij}}{E_i - E_j}, \tag{2.39}$$

where $X = \frac{1}{3}\Big[S_1, \Big[S_1, \hat{V}\Big]\Big]$. Finally, we obtain the effective Hamiltonian

$$\tilde{H} = \hat{H}_0 + \frac{\lambda^2}{2}\Big[S_1 + S_3, \hat{V}\Big] - \frac{\lambda^4}{24}\Big[S_1, \Big[S_1, \Big[S_1, \hat{V}\Big]\Big]\Big]. \tag{2.40}$$

This Hamiltonian is block diagonal and includes terms to fourth order in the perturbation. Note that, if the unperturbed Hamiltonian is not diagonal, finding the generator of the transformation is not trivial. This applies to both S_1 and S_3. Thus, in this thesis, we will restrict the application of the SW transformation to diagonal unperturbed Hamiltonians.

Chapter 3

Coupled single spin qubit Hamiltonian

Here, we derive the system Hamiltonian for two quantum dot based single spin qubits coupled to a ferromagnet, following the work of Skogvoll et al. [52]. With this framework established, we in chapter 4 proceed to expand the system by adding a second quantum dot and a second electron to each of the qubits in the single spin system. We then derive both a full system Hamiltonian and an effective low-energy Hamiltonian for this coupled DQD system. We begin, however, with the single spin qubit system.

The Hamiltonian for single spin qubits coupled to a ferromagnet may be split into three parts: the energy of the qubits, the ferromagnetic energy, and the interaction energy between the ferromagnet and the qubits,

$$\hat{H} = \hat{H}_q + \hat{H}_F + \hat{H}_{int}, \tag{3.1}$$

with $\hat{H}_q$ describing a spin qubit, $\hat{H}_F$ describing the ferromagnet, and $\hat{H}_{int}$ describing the interaction between the two. In the following sections, we derive each of the three terms of Eq. 3.1.

3.1 Spin qubit Hamiltonian

Lifting the degeneracy of the spin-up and spin-down states of the electron by an applied magnetic field, the qubit may be encoded in this energy splitting, thereby defining spin-up as $|1\rangle$ and spin-down as $|0\rangle$. Defining the qubit energy splitting to be ω_q, the Hamiltonian of the qubits may be written

$$\hat{H}_q = \sum_{i=1,2} \frac{\omega_q^{(i)}}{2} \hat{\sigma}_z^{(i)}, \tag{3.2}$$

where the index i denotes the qubit number, and $\hat{\sigma}_z^{(1)} = \hat{\sigma}_z \otimes I_2$, $\hat{\sigma}_z^{(2)} = I_2 \otimes \hat{\sigma}_z$. Here, $\hat{\sigma}_z$ is the standard Pauli matrix and I_2 is the 2x2 identity matrix. The operators $\hat{\sigma}_z^{(i)}$ as defined above function as Pauli operators in the two-qubit Hilbert

space. Setting the energy splitting of the first qubit $\omega_q^{(1)} = \omega_q$, we may write the energy splitting of the second qubit as $\omega_q^{(2)} = \omega_q - \delta$, so that δ parametrizes the difference in qubit splittings between the two qubits. The case $\delta = 0$ thus corresponds to the two qubits having the same splitting.

3.2 Ferromagnet Hamiltonian

In the context of this paper, we consider the ferromagnet to be an array of spins that, in the ground state, are parallel. The spins are all assumed to be coupled to their nearest neighbor through the exchange interaction with a coupling strength described by J:

$$\hat{H}_F^{(1)} = -J \sum_{\langle i,j \rangle} \mathbf{S}_i \cdot \mathbf{S}_j, \tag{3.3}$$

where the exchange energy $J > 0$ and the sum over $\langle i, j \rangle$ runs over nearest neighbors on each lattice site [53, p. 74]. We assume the magnet to be insulating, neglecting any electron tunneling between sites. Applying a magnetic field $H_0\hat{\mathbf{z}}$ gives a contribution

$$\hat{H}_F^{(2)} = |\gamma|\mu_0 H_0 \sum_i S_i^z, \tag{3.4}$$

known as the Zeeman energy, at each site i. Here, $|\gamma|$ is the gyromagnetic ratio and μ_0 is the vacuum permeability. Finally, we take into account a general magnetic anisotropy in the ferromagnet, included as

$$\hat{H}_F^{(3)} = \sum_i \Big[K_x (S_i^x)^2 + K_y (S_i^y)^2 + K_z (S_i^z)^2 \Big]. \tag{3.5}$$

Here, the constants $K_{x,y,z}$ parametrize the magnetic anisotropy in their respective directions. This anisotropy may for instance arise from magnetocrystalline anisotropy, wherein aligning magnetic moments along certain axes in the ferromagnet crystal structure is energetically favorable [54]. The total ferromagnetic Hamiltonian is finally written as the sum of these three contributions:

$$\hat{H}_F = -J \sum_{\langle i,j \rangle} \mathbf{S}_i \cdot \mathbf{S}_j + |\gamma|\mu_0 H_0 \sum_i S_i^z + \sum_i \Big[K_x (S_i^x)^2 + K_y (S_i^y)^2 + K_z (S_i^z)^2 \Big]. \tag{3.6}$$

The Hamiltonian in Eq. 3.6 may be mapped into bosonic magnon operators using the Holstein-Primakoff transformation presented in Sec. 2.3. Assuming the contribution from the Zeeman energy to be considerably larger than the contribution from anisotropy, the spins are considered to be mostly ordered along $\hat{\mathbf{z}}$. It then suffices to use the linear Holstein-Primakoff transformation found in Eq. 2.17. First, consider a ferromagnet in the absence of magnetic anisotropy, that is, consider only the first two terms in Eq. 3.6. Employing the Holstein-Primakoff transformation and keeping terms to second order in magnon operators gives

$$\hat{H}_F^{(1,2)} = |\gamma|\mu_0 H_0 \sum_i \hat{a}_i^\dagger \hat{a}_i - 2JS \sum_{\langle i,j \rangle} \Big[\hat{a}_i^\dagger \hat{a}_j - \hat{a}_i^\dagger \hat{a}_i \Big]. \tag{3.7}$$

Above, we have neglected all constant terms as they simply alter the zero-point reference energy. The magnon operators in Eq. 3.7 may be represented as quantized spin waves [48, p. 292] with wavevector $\mathbf{k}$. Introducing Fourier transformed operators $a_{\mathbf{k}}$ through the relations $\hat{a}_i = \frac{1}{\sqrt{N}} \sum_{\mathbf{k}} \hat{a}_{\mathbf{k}} e^{-i\mathbf{k}\cdot\mathbf{r}_i}$ and $\hat{a}_i^\dagger = \frac{1}{\sqrt{N}} \sum_{\mathbf{k}} \hat{a}_{\mathbf{k}}^\dagger e^{i\mathbf{k}\cdot\mathbf{r}_i}$, where N is the number of lattice sites, yields

$$\hat{H}_F^{(1,2)} = |\gamma|\mu_0 H_0 \sum_{\mathbf{k}} \hat{a}_{\mathbf{k}}^\dagger \hat{a}_{\mathbf{k}} + 2JS \sum_{\mathbf{k}} [z - \chi(\mathbf{k})] \hat{a}_{\mathbf{k}}^\dagger \hat{a}_{\mathbf{k}}, \tag{3.8}$$

where z is the number of nearest neighbors on a lattice site, $\chi(\mathbf{k}) = \sum_{\boldsymbol{\delta}} e^{-i\mathbf{k}\cdot\boldsymbol{\delta}}$, and $\boldsymbol{\delta}$ denotes vectors between neighboring lattice sites. Note that $\chi(0) = \sum_{\boldsymbol{\delta}} 1 = z$ by definition, as z is the number of available vectors $\boldsymbol{\delta}$ to nearest neighbors. The prefactors in Eq. 3.8 may all be combined into $\omega_{\mathbf{k}} = |\gamma|\mu_0 H_0 - 2SJz + \chi(\mathbf{k})$, resulting in the isotropic ferromagnet Hamiltonian

$$\hat{H}_F^{(1,2)} = \sum_{\mathbf{k}} \omega_{\mathbf{k}} \hat{a}_{\mathbf{k}}^\dagger \hat{a}_{\mathbf{k}}. \tag{3.9}$$

The operator $\hat{a}_{\mathbf{k}}^\dagger \hat{a}_{\mathbf{k}}$ is the magnon number operator; it simply counts the number of magnon excitations with wavevector $\mathbf{k}$ present in the ferromagnet. The prefactor $\omega_{\mathbf{k}}$ is then the energy associated with each such magnon excitation. Furthermore, $\hat{H}_F^{(1,2)}$ is diagonal; the above magnons are eigenmodes of the isotropic system. Note the similarity with the Hamiltonian of the quantum harmonic oscillator presented in Sec. 2.1. As in Eq. 2.3, the magnons may be viewed as excitations of spin-flips that increase the energy of the system above the ground state of completely aligned spins.

Now, consider the anisotropy term in Eq. 3.5. By employing the relations $S_i^x = \frac{1}{2}\left(S_i^+ + S_i^-\right)$, $S_i^y = \frac{1}{2i}\left(S_i^+ - S_i^-\right)$ and the Holstein-Primakoff transformation as above, $\hat{H}_F^{(3)}$ may be rewritten

$$\hat{H}_F^{(3)} = \sum_i \left[\frac{S}{2}(K_x - K_y)\left(\hat{a}_i^\dagger \hat{a}_i^\dagger + \hat{a}_i \hat{a}_i + 2\hat{a}_i^\dagger \hat{a}_i\right) + K_z\left(S^2 - 2S\hat{a}_i^\dagger \hat{a}_i\right)\right]. \tag{3.10}$$

In order to write this in a way that is comparable to Eq. 3.9, similar Fourier transforms as above are carried out, resulting in

$$\hat{H}_F^{(3)} = S(K_x - K_y + 2K_z) \sum_{\mathbf{k}} \hat{a}_{\mathbf{k}}^\dagger \hat{a}_{\mathbf{k}} + \frac{S}{2}(K_x - K_y) \sum_{\mathbf{k}} \left[\hat{a}_{\mathbf{k}}^\dagger \hat{a}_{-\mathbf{k}}^\dagger + \hat{a}_{\mathbf{k}} \hat{a}_{-\mathbf{k}}\right]. \tag{3.11}$$

Now, Eqs. 3.9 and 3.11 may be combined into the total ferromagnet Hamiltonian

$$\hat{H}_F = \sum_{\mathbf{k}} \left[A_{\mathbf{k}} \hat{a}_{\mathbf{k}}^\dagger \hat{a}_{\mathbf{k}} + B_{\mathbf{k}}\left(\hat{a}_{\mathbf{k}}^\dagger \hat{a}_{-\mathbf{k}}^\dagger + \hat{a}_{\mathbf{k}} \hat{a}_{-\mathbf{k}}\right)\right], \tag{3.12}$$

with $A_{\mathbf{k}} = |\gamma|\mu_0 H_0 + 2JS[z - \chi(\mathbf{k})] + S(K_x - K_y + 2K_z)$ and $B_{\mathbf{k}} = \frac{S}{2}(K_x - K_y)$. Similarly to Eq. 3.9, the term $\sum_{\mathbf{k}} A_{\mathbf{k}} \hat{a}_{\mathbf{k}}^\dagger \hat{a}_{\mathbf{k}}$ describes the number of magnon excitations for each wavevector $\mathbf{k}$, and the energy of each excitation. The terms $\sum_{\mathbf{k}} B_{\mathbf{k}}\left(\hat{a}_{\mathbf{k}}^\dagger \hat{a}_{-\mathbf{k}}^\dagger + \hat{a}_{\mathbf{k}} \hat{a}_{-\mathbf{k}}\right)$, however, deviate from this simple picture and require

further investigation. For simplicity, we consider only the uniform $\mathbf{k} = 0$ mode in the following derivation. This is justified by considering magnets on a sufficiently small scale so that the uniform mode is well separated from higher energy modes [55]. This simplifies Eq. 3.12 to

$$\hat{H}_F = A\hat{a}^\dagger\hat{a} + B((\hat{a}^\dagger)^2 + \hat{a}^2), \tag{3.13}$$

with $A = |\gamma|\mu_0 H_0 + S(K_x - K_y + 2K_z)$ and $B = \frac{S}{2}(K_x - K_y)$.

However, Eq. 3.13 still contains the off-diagonal terms $(\hat{a}^\dagger)^2$ and $\hat{a}^2$. In order to diagonalize it, we perform a Bogoliubov transformation, a canonical transformation in which we introduce new operators $\hat{\alpha}$ and $\hat{\alpha}^\dagger$ such that

$$\hat{a} = u\hat{\alpha} + v\hat{\alpha}^\dagger. \tag{3.14}$$

Here, we require that the new operators obey bosonic commutation relations, so that $\left[\hat{\alpha}, \hat{\alpha}^\dagger\right] = 1$ and $[\hat{\alpha}, \hat{\alpha}] = \left[\hat{\alpha}^\dagger, \hat{\alpha}^\dagger\right] = 0$. These relations are satisfied as long as $u^2 - v^2 = 1$. Considering this constraint we may parametrize u and v as $u = \cosh r$ and $v = \sinh r$. With this transformation, the Hamiltonian becomes

$$H_F = \omega_0\hat{\alpha}^\dagger\hat{\alpha}, \tag{3.15}$$

with $\sinh r = \frac{-2B}{\sqrt{(A+\omega_0)^2 - 4B^2}}$ and $\omega_0 = \sqrt{A^2 - 4B^2}$ [52]. The operators $\hat{\alpha}, \hat{\alpha}^\dagger$ are bosonic eigenmodes of the anisotropic ferromagnet, with ω_0 as the eigenmode energy. Unlike the spin-1 magnons that were eigenmodes of the isotropic ferromagnet, this transformed magnon excitation is a superposition of odd-number magnon states [56]. In order to understand the relation between these magnons and the spin-1 magnons that were eigenmodes of the isotropic ferromagnet, we consider the vacuum state of the anisotropic system, defined as

$$\hat{\alpha}\left|0\right\rangle_{\hat{\alpha}} = 0, \tag{3.16}$$

where the subscript $\hat{\alpha}$ denotes the vacuum state in the transformed basis. Considering the transformation in Eq. 3.14, we may conversely write the $\hat{\alpha}$ operator as $\hat{\alpha} = u\hat{a} - v\hat{a}^\dagger$, with $u = \cosh r$ and $v = \sinh r$. Inserting into Eq. 3.16, we obtain

$$(\cosh r\hat{a} - \sinh r\hat{a}^\dagger)\left|0\right\rangle_{\hat{\alpha}} = 0. \tag{3.17}$$

Comparing this expression to Eq. 2.12, we see that the definition of the vacuum state for the anisotropic ferromagnet corresponds to acting on the spin-1 magnon operator with a squeezing operator $S(\xi)$ for $\theta = 0$. Thus, in analogy to squeezed states of light in quantum optcs, we may call these new eigenmodes of the anisotropic ferromagnet squeezed magnons. The parameter r that defines the transformation to the squeezed basis is therefore known as the squeezing parameter. Importantly, the squeeze parameter is directly related to the anisotropy of the ferromagnet. This anisotropy may be affected by external fields, for instance by imposing a strain on the magnet [57]. This, in principle, allows for tuning of the degree of squeezing in the system. As we shall see in the following section, this

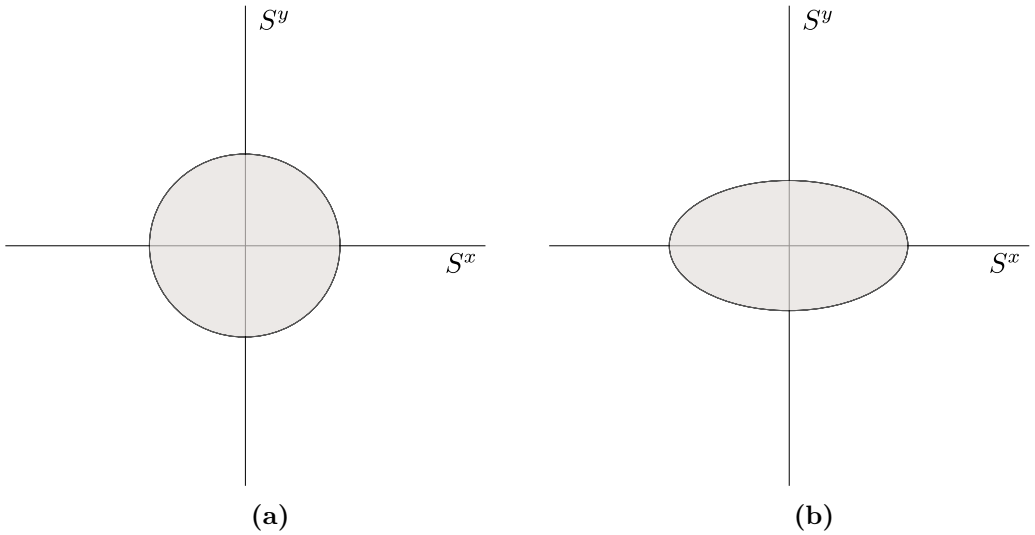

Figure 3.1: Uncertainty ellipses for **a)** isotropic and **b)** anisotropic ferromagnets with ground state magnetization along $\hat{\mathbf{z}}$. In the anisotropic ferromagnet, the fluctuations in the $\hat{\mathbf{y}}$ component the spin operator are, in this case, suppressed. Heisenberg's uncertainty relation is upheld by a corresponding increase in the fluctuations of the $\hat{\mathbf{x}}$ component. Figures adapted from [58].

has important implications for the coupling between the quantum dots and the ferromagnet.

The squeezing results from the system reducing uncertainty in one quadrature while increasing uncertainty in another, so that the normally circular uncertainty is squeezed into an elliptical shape. This is visualized in Fig. 3.1, in which we show an example of uncertainty ellipses for an anisotropic ferromagnet, contrasted with the isotropic case. In the figure, we have assumed the energy cost on the $\hat{\mathbf{y}}$ component of a spin in the ferromagnet to be larger than that of the $\hat{\mathbf{x}}$ component, corresponding to $K_x < K_y$ in Eq. 3.5. Hence, the quantum fluctuations in the $\hat{\mathbf{y}}$ component of the spin operator will be suppressed at the expense of increased fluctuations of the $\hat{\mathbf{x}}$ component [58]. This allows the ferromagnet to minimize energy while upholding the Heisenberg uncertainty relation [59].

3.3 Interaction Hamiltonian

We assume the spin qubits to be exchange coupled to the ferromagnet, and here derive the Hamiltonian describing one spin qubit coupled to the ferromagnet. For each spin qubit, assume there are N_{int} sites where coupling between the qubit and the ferromagnet may occur. The interaction Hamiltonian may be written

$$\hat{H}_{int} = J_{int} \sum_l \mathbf{S}_l \cdot \mathbf{s}_l, \tag{3.18}$$

where $\mathbf{S}_l$ is the ferromagnetic spin operator at interfacial site l and $\mathbf{s}_l$ is the spin of the electron in the quantum dot at the same site. J_{int} describes the strength of the exchange coupling. We first consider the ferromagnet to be isotropic.

The spin operator of the electron may be expressed as [52]

$$\mathbf{s}_l = \frac{|\psi_l|^2}{2}\boldsymbol{\sigma}, \tag{3.19}$$

where ψ_i is the amplitude of the wavefunction of the electron at site l. The components of the Pauli vector $\boldsymbol{\sigma} = \hat{\sigma}_x\hat{\mathbf{x}} + \hat{\sigma}_y\hat{\mathbf{y}} + \hat{\sigma}_z\hat{\mathbf{z}}$ are defined as in Sec. 3.1. Using $S_l^{+/-} = S_l^x \pm iS_l^y$ and $s_l^{+/-} = s_l^x \pm is_l^y$, we may express the interaction Hamiltonian as the sum of two terms $\hat{H}_{int} = \hat{H}_{int1} + \hat{H}_{int2}$, where

$$\begin{aligned}\hat{H}_{int1} &= J_{int}\sum_l S_l^z s_l^z \\ &= \frac{J_{int}}{2}\sum_l |\psi_l|^2(S - \hat{a}_l^\dagger\hat{a}_l)\hat{\sigma}_z \\ &\approx \frac{1}{2}J_{int}N_{int}\xi S\hat{\sigma}_z,\end{aligned} \tag{3.20}$$

and $\xi = \sum_l \frac{|\psi_l|^2}{N_{int}}$ is the average qubit wavefunction intensity averaged over all interfacial sites. In the second line we have applied the Holstein-Primakoff transformation as in Sec. 2.3, retaining terms to quadratic order in magnon operators. For the second contribution we obtain

$$\begin{aligned}\hat{H}_{int2} &= \frac{J_{int}}{2}\sum_l (S_l^+ s_l^- + S_l^- s_l^+) \\ &= J_{int}\sqrt{\frac{S}{2}}\sum_l |\psi_l|^2(\hat{a}_l^\dagger\hat{\sigma}_- + \hat{a}_l\hat{\sigma}_+),\end{aligned} \tag{3.21}$$

where the Holstein-Primmakoff transformation has once again been applied. As in Eq. 3.8 we introduce Fourier transformed operators for $\hat{a}_l$ and retain only the uniform $\mathbf{k} = 0$ mode. This yields

$$\hat{H}_{int2} = J_{int}N_{int}\xi\sqrt{\frac{S}{2N}}(\hat{a}^\dagger\hat{\sigma}_- + \hat{a}\hat{\sigma}_+). \tag{3.22}$$

Having obtained these two contributions we may write the combined interaction Hamiltonian as

$$\hat{H}_{int} = J_{int}N_{int}\xi\left[\sqrt{\frac{S}{2N}}(\hat{a}^\dagger\hat{\sigma}_- + \hat{a}\hat{\sigma}^+) + \frac{S}{2}\hat{\sigma}_z\right]. \tag{3.23}$$

The second term within the brackets of Eq. 3.23 renormalizes the qubit splitting and may be absorbed into the qubit energy derived in Sec. 3.1, redefining $\hat{H}_q' = \hat{H}_q + \hat{H}_{int1} = \frac{\omega_q'}{2}\hat{\sigma}_z$ where $\omega_q' = \omega_q + J_{int}N_{int}\xi S$ [56]. In order to avoid clutter the primes will be omitted in the remainder of the thesis.

The first term describes two possible processes that may occur due to the interaction between the ferromagnet and the qubit. First, an excited spin state in the qubit may relax while a magnon is created, described by $\hat{a}^\dagger\hat{\sigma}_-$. Second, a

magnon may be destroyed, causing an excitation of spin in the qubit, described by $\hat{a}\hat{\sigma}_+$. Note that in both cases, the number of spin excitations is conserved. The prefactors to this term are gathered into a coupling constant g so that the interaction Hamiltonian may be written, for two spin qubits coupled to an isotropic ferromagnet,

$$\hat{H}_{int} = \sum_{i=1,2} g(\hat{a}^\dagger \hat{\sigma}_-^{(i)} + \hat{a}\hat{\sigma}_+^{(i)}), \tag{3.24}$$

assuming g to be the same for both qubits.

If instead the ferromagnet is anisotropic, a similar Bogoliubov transformation as in Sec. 3.2 may be carried out for the magnon operators in Eq. 3.24. Inserting the transformation $\hat{a} = \cosh r\hat{\alpha} + \sinh r\hat{\alpha}^\dagger$ into Eq. 3.24 results in

$$\hat{H}_{int} = \sum_{i=1,2} \Big[g_R(\hat{\alpha}^\dagger \hat{\sigma}_-^{(i)} + \hat{\alpha}\hat{\sigma}_+^{(i)}) + g_{CR}(\hat{\alpha}^\dagger \hat{\sigma}_+^{(i)} + \hat{\alpha}\hat{\sigma}_-^{(i)}) \Big], \tag{3.25}$$

where we have defined $g_R = g\cosh r$ and $g_{CR} = g\sinh r$. Here g_R and g_{CR} are prefactors to what are known as rotating and counter-rotating terms, respectively. Unlike the rotating terms, the counter-rotating terms $\hat{\alpha}^\dagger\hat{\sigma}_+$ and $\hat{\alpha}\hat{\sigma}_-$ do not conserve the number of excitations. Rather, the $\hat{\alpha}^\dagger\hat{\sigma}_+$ term describes the simultaneous excitation of both a spin state and magnon. Similarly, the $\hat{\alpha}\hat{\sigma}_-$ term describes the simultaneous relaxation and annihilation of a spin state and a magnon, respectively. Furthermore, note that by setting the squeezing parameter $r = 0$ the counter-rotating terms vanish, and we regain the Hamiltonian of Eq. 3.24, as expected. Additionally, as both $\cosh r$ and $\sinh r$ are monotonically increasing functions of r, the coupling strength increases with magnon squeezing.

Finally, we may combine Eqs. 3.2, 3.15, and 3.25 into the full system Hamiltonian

$$H = \omega_0\hat{\alpha}^\dagger\hat{\alpha} + \sum_{i=1,2} \left[\frac{\omega_q^{(i)}}{2}\hat{\sigma}_z^{(i)} + g_R\Big(\hat{\alpha}^\dagger\hat{\sigma}_-^{(i)} + \hat{\alpha}\hat{\sigma}_+^{(i)}\Big) + g_{CR}\Big(\hat{\alpha}^\dagger\hat{\sigma}_+^{(i)} + \hat{\alpha}\hat{\sigma}_-^{(i)}\Big) \right]. \tag{3.26}$$

This Hamiltonian is a realization of the anisotropic quantum Rabi model [60]. By including anisotropy in the derivation of the ferromagnetic and interaction Hamiltonians, we obtain squeezed magnons as the eigenmodes of the ferromagnet. This in turn gives rise to counter-rotating terms (g_{CR}) in the interaction between the qubits and the Hamiltonian.

Recall the tunability of the squeezing parameter r as described in the previous section. Through the dependence of the coupling terms g_R and g_{CR} on r, we are in principle able to alter the coupling between the quantum dots and the ferromagnet by altering the anisotropy of the magnet. In Sec. 5.2 we will see that this tunability plays an important role in limiting leakage from the qubit subspace.

3.4 Numerical simulation of coupled spin qubits

The full system Hamiltonians of Eq. 3.26, for the single spin qubit case, is difficult to treat analytically. Thus, in order to understand how the system evolves in

time, we here solve the time-dependent Schrödinger equation (TDSE),

$$i\hbar\frac{\partial}{\partial t}\left|\psi(t)\right\rangle = \mathcal{H}\psi(t), \tag{3.27}$$

numerically using the Python QuTiP package [61]. This is done by applying the QuTiP built in function for solving the TDSE, *sesolve* [62], on a matrix Hamiltonian constructed from Eq. 3.26. Given an initial state $|\psi(0)\rangle$ and a Hamiltonian $\mathcal{H}$, the *sesolve* function calculates the time evolved state $|\psi(t)\rangle$ for each time step. We may then calculate the overlap with any state $|\chi\rangle$ we are interested in as $|\langle\psi(t)|\chi\rangle|^2$. The code used to produce the following simulations may be found in Appendix A.1

We begin by presenting a summary of the numerical results obtained for the single spin qubit case. Later on, in Sec. 5.1, this will be useful to highlight the specific benefits of the coupled DQD system. For a more thorough report on the single spin qubit system, we refer to the preceding project work [1].

In each of the following calculations, the single spin qubit Hamiltonian (Eq. 3.26) was limited to containing a maximum of 50 magnons. Due to the energy cost associated with increasing magnon occupations, this is believed to be sufficient to capture all effects from magnons on the dynamics of the system. In the following sections, unless stated otherwise, we assume the qubits to be identical so that $\delta = 0$ and $\omega_q^{(1)} = \omega_q^{(2)} = \omega_q$. We also define the zero point energy of the system to be in the middle of the qubit splitting, so that the energy associated with a spin-up (spin-down) state is $(-)\frac{\omega_q}{2}$. In all following simulations, the rotating coupling term is set to $g_R = 0.1\omega_q$

We now evaluate the dynamics of the states in the 0-magnon subspace ($|0\uparrow\uparrow\rangle$, $|0\uparrow\downarrow\rangle$, $|0\downarrow\uparrow\rangle$, and $|0\downarrow\downarrow\rangle$) and how they are influenced by states with higher magnon occupations. We begin by considering a system where the magnon energy is tuned to be resonant with the qubit splitting, setting $\omega_0 = \omega_q$. This system is evaluated both for an isotropic ($g_{CR} = 0$) and an anisotropic ($g_{CR} = 0.1\omega_q$) ferromagnet. The same evaluation is then carried out for a system with magnon energy tuned away from resonance, setting $\omega_0 = 2\omega_q$. Once again we consider both isotropic and anisotropic ferromagnets.

First, we consider the system in absence of magnon squeezing by setting $g_{CR} = 0$. Furthermore, we set the magnon energy to resonance ($\omega_0 = \omega_q$) and initialize in $|0\uparrow\downarrow\rangle$. Calculating the time evolution from this initial state, we evaluate the probability for the system to occupy the $|0\uparrow\downarrow\rangle$ and $|0\downarrow\uparrow\rangle$ states as a function of time. These probabilities are plotted in Fig. 3.2, as the solid blue and orange lines, respectively. The figure shows well behaved coherent switching between the two states. Note however the slight deviation from harmonic oscillation in both plots; the valleys appear to be slightly broadened compared to the peaks. This is due to leakage to the $|1\downarrow\downarrow\rangle$ state through the rotating coupling term $\alpha^\dagger\sigma_-$, which in Fig. 3.2 is depicted as the dotted green line. In this coupling, a spin is relaxed from spin-up to spin-down (σ_-) and a magnon excitation created ($\alpha^\dagger$). The energies associated with the $|0\uparrow\downarrow\rangle$ and $|0\downarrow\uparrow\rangle$ states are zero, as the two opposite spins cancel the contribution from one another.

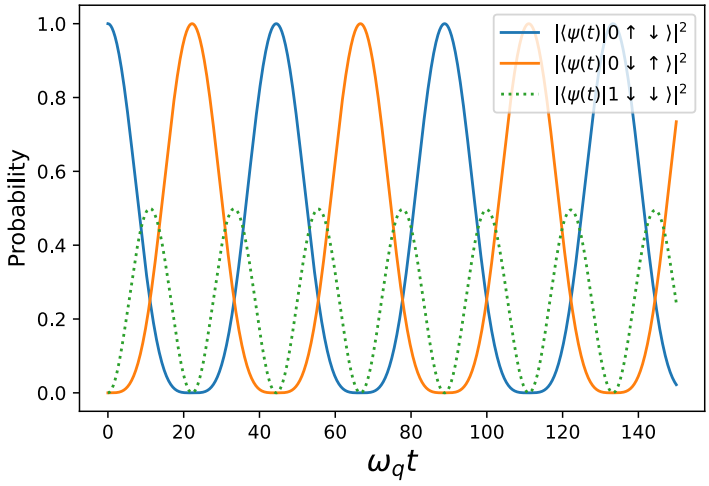

Figure 3.2: Time evolution of Hamiltonian in Eq. 3.26, initialized in $|0\uparrow\downarrow\rangle$, depicting occupation probabilities of $|0\uparrow\downarrow\rangle$ (solid blue line), $|0\downarrow\uparrow\rangle$ (solid orange line), and $|1\downarrow\downarrow\rangle$ (dotted green line). In this simulation, $\omega_0 = \omega_q$, $g_R = 0.1\omega_q$ and $g_{CR} = 0$ was employed.

The $|1\downarrow\downarrow\rangle$ state has an energy of $\omega_0 - \omega_q$. Therefore, for $\omega_0 \approx \omega_q$, the states are degenerate, facilitating the transition. Crucially, this leakage prevents the qubits from evenly mixing without influence from states outside the qubit subspace. Due to the probability for the system to simultaneously leak into $|1\downarrow\downarrow\rangle$ (visible as peaks in the dotted green lines), the $|0\uparrow\downarrow\rangle$ and $|0\downarrow\uparrow\rangle$, the crossing point between the two states is lowered.

We now include magnon squeezing by setting $g_{CR} = g_R = 0.1\omega_q$. As in Fig. 3.2, we initialize in $|0\uparrow\downarrow\rangle$ and calculate the evolution of the $|0\uparrow\downarrow\rangle$, $|0\downarrow\uparrow\rangle$, $|1\downarrow\downarrow\rangle$, and $|1\uparrow\uparrow\rangle$ states with the magnon energy at resonance, shown in Fig 3.3. Although the inclusion of the squeezed magnons has decidedly made the evolution more complicated than in Fig. 3.2, the two qubits still exchange their states. As before, the $|0\uparrow\downarrow\rangle$ (solid blue) and $|0\downarrow\uparrow\rangle$ (solid orange) states are coupled to $|1\downarrow\downarrow\rangle$ (dotted green) through the rotating coupling. Through the introduction of squeezed magnons, they are also able to excite a magnon and excite a spin ($\alpha^\dagger\sigma_+$), which couples them to the $|1\uparrow\uparrow\rangle$ state (dotted yellow). However, leakage into this state is minimal, evident by the probability of $|1\uparrow\uparrow\rangle$ to be occupied being close to zero in Fig. 3.3. This is likely due to this state having an energy of $\omega_0 + \omega_q$, higher than that of the other three states considered here.

As noted above, the significant leakage to the $|1\downarrow\downarrow\rangle$ state we may observe in Figs. 3.2 and 3.3 is likely due to this state being degenerate with $|0\uparrow\downarrow\rangle$ and $|0\downarrow\uparrow\rangle$ when the magnon energy is resonant with the qubit splitting. To mitigate this leakage issue we now consider systems in which the magnon energy is tuned away from resonance, setting $\omega_0 = 2\omega_q$, lifting the aforementioned degeneracy.

We first consider a system comprised of an isotropic ferromagnet, setting the counter rotating term g_{CR} to be zero. We once again initialize in $|0\uparrow\downarrow\rangle$, and calculate the time evolution of the $|0\uparrow\downarrow\rangle$, $|0\downarrow\uparrow\rangle$, $|1\downarrow\downarrow\rangle$ and $|1\uparrow\uparrow\rangle$ states for

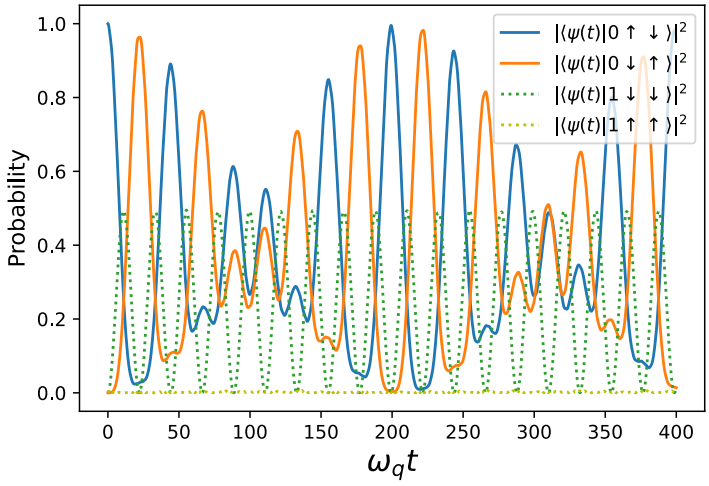

Figure 3.3: Time evolved occupation probabilities of $|0\uparrow\downarrow\rangle$ (solid blue), $|0\downarrow\uparrow\rangle$ (solid orange), $|1\downarrow\downarrow\rangle$ (dotted green) and $|1\uparrow\uparrow\rangle$ (dotted yellow), with initial state $|\psi(0)\rangle = |0\uparrow\downarrow\rangle$, at resonance ($\omega_0 = \omega_q$) and including magnon squeezing so that $g_R = g_{CR} = 0.1\omega_q$.

a system with the magnon energy tuned away from resonance. The resulting time evolution is shown in Fig. 3.4a. As we can see, the $|1\downarrow\downarrow\rangle$ and $|1\uparrow\uparrow\rangle$ states are barely occupied, indicating that the leakage issue has indeed been mitigated. Furthermore, we observe that the $|0\uparrow\downarrow\rangle$ and $|0\downarrow\uparrow\rangle$ states show well-behaved coherent switching, and are able to evenly mix. This is in contrast to the situation depicted in Fig 3.2, where the leakage into $|1\downarrow\downarrow\rangle$ prevented even mixing of the states. Similar conclusions may be drawn from Fig. 3.4b, in which we have introduced anisotropy to the ferromagnet, setting $g_{CR} = 0.1\omega_q$. The parameters are otherwise the same as the ones used to calculate the evolution in Fig. 3.4a. Once again, we calculate the time evolution of the $|0\uparrow\downarrow\rangle$, $|0\downarrow\uparrow\rangle$, $|1\downarrow\downarrow\rangle$ and $|1\uparrow\uparrow\rangle$, initializing in $|0\uparrow\downarrow\rangle$. Qualitatively, the time evolution is identical to the isotropic ferromagnet system. We observe a slight increase in the switching frequency of the qubits, likely due to the inclusion of the counter-rotating term increasing the coupling strength between the qubit states.

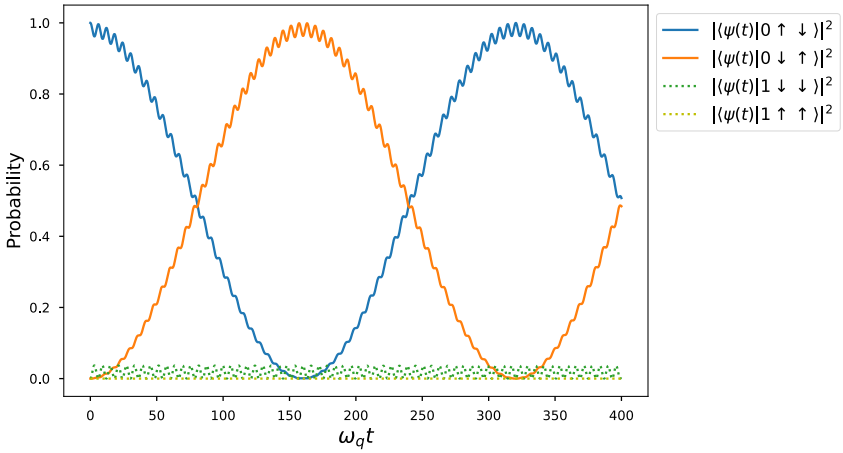

(a)

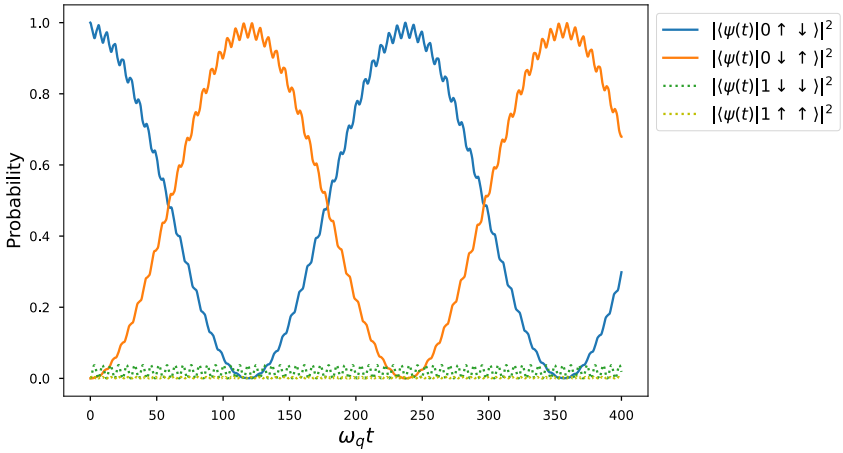

(b)

Figure 3.4: Time evolved occupation probabilities of $|0\uparrow\downarrow\rangle$ (solid blue), $|0\downarrow\uparrow\rangle$ (solid orange), $|1\downarrow\downarrow\rangle$ (dotted green) and $|1\uparrow\uparrow\rangle$ (dotted yellow), with initial state $|\psi(0)\rangle = |0\uparrow\downarrow\rangle$, with magnon energy tuned to $\omega_0 = 2\omega_q$ and $g_R = 0.1\omega_q$. **a)** Time evolution calculated for a system with an isotropic ferromagnet, $g_{CR} = 0$. **b)** Time evolution calculated for a system with an anisotropic ferromagnet, $g_{CR} = 0.1\omega_q$.

Chapter 4

Coupled singlet-triplet Hamiltonian

Building on the framework established in the single spin qubit case, we now expand the system to include a second quantum dot on each side of the ferromagnet. The setup is sketched in Fig. 4.1. Each DQD on either side of the ferromagnet hosts two electrons that may either inhabit the (1,1) or (0,2) charge configurations. The DQDs are subjected to a relative electrostatic potential described by the detuning parameter ε. We assume the dots to be small enough and the relative electrostatic potential of the dots to be tuned so that the orbital level splitting between the (0,2) singlet and triplet states is sufficiently large that any occupation probability of the (0,2) triplet may be safely neglected. Furthermore, the DQDs are exposed to a uniform external magnetic field B in order to lift the degeneracy of the spin-up and spin-down states.

The two dots in the DQD are tunnel coupled to one another, hybridizing the singlet states. However, due to the limited range of the exchange interaction, only the dot closest to the ferromagnet experiences the exchange coupling to the magnet. To account for this we include a magnetic field gradient ΔB across the two quantum dots. This gradient may be understood by considering the contribution to $\hat{\sigma}_z$ derived in Eq. 3.20, which will only apply for the closest of the dots. A second contribution to the gradient is due to the demagnetization field of the ferromagnet varying across the double dot system. We will not derive the exact form of the magnetic field gradient in this thesis, but rather take it as a parameter of the system.

We describe the DQD system through the $\{|T_+\rangle, |T_0\rangle, |S_{11}\rangle, |T_-\rangle, |S_{02}\rangle\}$ states. Here, the $|T_\pm\rangle$ states refer to the polarized triplet states $|\uparrow\uparrow\rangle$ and $|\downarrow\downarrow\rangle$. The leftmost arrow in $|\uparrow\uparrow\rangle$ and $|\downarrow\downarrow\rangle$ denotes the spin in the dot closest to the ferromagnet. For brevity the indices indicating the dot hosting the electron spin have been dropped for states in the (1,1) charge configuration. The $|T_0\rangle$ ($|S_{11}\rangle$) state refers to the unpolarized triplet (singlet) state $\frac{1}{\sqrt{2}}(|\uparrow\downarrow\rangle \pm |\downarrow\uparrow\rangle)$. Finally, the $|S_{02}\rangle$ state refers to the (0,2) configuration singlet state, $|\uparrow_2\downarrow_2\rangle$, where the indices denote that the spins are located in the second dot.

The qubit states $|0\rangle$ and $|1\rangle$ are encoded in the second and third lowest energy

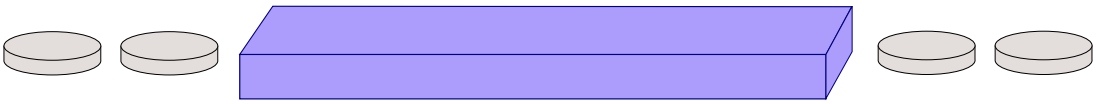

Figure 4.1: Schematic of the ferromagnetically coupled double quantum dot system. The ferromagnet is depicted in blue, with two quantum dots depicted in gray on either end of the magnet, each hosting two spins.

eigenstates of the DQD Hamiltonian, respectively. These energies may be seen in Fig. 4.2, in which the energies of each eigenstate of the DQD system is calculated numerically as a function of the detuning parameter. The energy of the $|1\rangle$ state corresponds to the green line, while the energy of the $|0\rangle$ state corresponds to the orange line. As we can see from Fig. 4.2, the difference in energy between these states varies depending on the choice of detuning parameter. This allows us to tune the qubit splitting via varying the relative electrostatic potential between the two quantum dots.

In the derivation of the system Hamiltonian, and subsequently, an effective Hamiltonian, we will be working in a basis constructed from the eigenstates of the DQD. However, as we will see in Sec. 4.3, these eigenstates are quite complicated superpositions of the $|T_0\rangle$, $|S_{11}\rangle$, $|S_{02}\rangle$ states. Thus, to gain an understanding of the system, we begin by working in the $\{|T_+\rangle, |\uparrow\downarrow\rangle, |\downarrow\uparrow\rangle, |T_-\rangle, |S_{02}\rangle\}$-basis, which we will call the $|\uparrow\downarrow\rangle$-basis for brevity. This choice of basis is motivated by

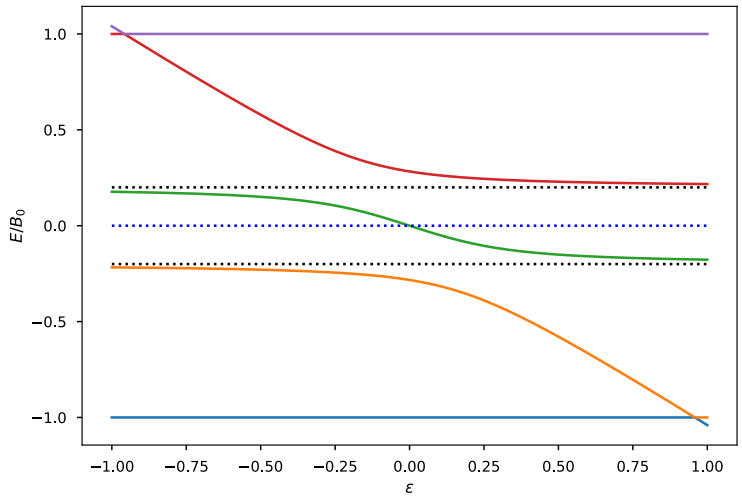

Figure 4.2: Numerically calculated energy spectrum of the DQD system as a function of the detuning parameter ε. The dotted blue line depicts the zero energy point. In contrast to Fig. 1.3, we include a magnetic field gradient across the DQD system, setting $\Delta B = 0.2B_0$. The dotted black lines correspond to energies of $\pm\Delta B$. Starting from the top, the energies correspond to the $|T_+\rangle$, $|2\rangle$, $|1\rangle$, $|0\rangle$, and $|T_-\rangle$ states, as described in Eq. 4.13. For both plots, the tunnel coupling is $t = 0.2B_0$. The DQD is exposed to a uniform external magnetic field of $\mathbf{B} = B_0\hat{\mathbf{z}}$.

recognizing that, for sufficiently negative detuning parameters, the $|0\rangle$ and $|1\rangle$ states may be approximated by the $|\downarrow\uparrow\rangle$ and $|\uparrow\downarrow\rangle$ states, respectively.

To understand this, consider the energy spectrum in Fig. 4.2 for $\varepsilon \leq -0.5B_0$, for which we may consider the mixing of the $|S_{11}\rangle$ and $|S_{02}\rangle$ due to the tunnel coupling to be quite small. Thus, if we disregard for the moment the magnetic field gradient (as in Fig. 1.3), the $|0\rangle$ and $|1\rangle$ states consist mainly of the $|S_{11}\rangle$ and $|T_0\rangle$ states, respectively, and these states are close to degenerate. Re-introducing the magnetic field gradient lifts the degeneracy and causes the $|S_{11}\rangle$ and $|T_0\rangle$ states to hybridize. If the eigenstates were exactly even mixtures of these states, this would correspond to the states $|0\rangle' = \frac{1}{\sqrt{2}}(|T_0\rangle - |S_{11}\rangle)$ and $|1\rangle' = \frac{1}{\sqrt{2}}(|T_0\rangle + |S_{11}\rangle)$, which are precisely the $|\downarrow\uparrow\rangle$ and $|\uparrow\downarrow\rangle$ states. These states would, in the absence of tunnel coupling, have energies of $\pm\Delta B$, respectively. These energy levels are depicted as the dotted black lines in Fig. 4.2. We see that the energies of the $|0\rangle$ and $|1\rangle$ deviate slightly from these energy levels, implying that the actual eigenstates will differ from $|\downarrow\uparrow\rangle$ and $|\uparrow\downarrow\rangle$. However, this energy shift is small enough that considering $|\downarrow\uparrow\rangle$ and $|\uparrow\downarrow\rangle$ as the qubit states is a reasonable approximation for values of ε that are negative and sufficiently far from zero.

Using the $|\uparrow\downarrow\rangle$-basis and restricting our analysis to a regime where ε is negative thus allows us to consider the simple $|\downarrow\uparrow\rangle$ and $|\uparrow\downarrow\rangle$ states rather than the more complicated actual eigenstates, and perform the derivation whilst maintaining a firmer grasp on the physical processes the Hamiltonian describes. This allows us to better understand the choices made when perturbatively obtaining an effective Hamiltonian, which will be useful when proceeding with the eigenstate basis.

Naturally, any state of the full coupled system will include information about the magnon occupation number as well as the state of each of the DQDs. These states will be written as $|n\phi_1\phi_2\rangle$. Here, n denotes the number of magnon excitations present in the system. The states of the DQDs on either side of the ferromagnet are described by $\phi_{1,2}$, respectively. For states with $n = 0$ we will omit the magnon excitation number from the state label, writing simply $|\phi_1\phi_2\rangle$.

4.1 In the $|\uparrow\downarrow\rangle$-basis

Consider the DQD Hamiltonian in the $\{|T_+\rangle, |\uparrow\downarrow\rangle, |\downarrow\uparrow\rangle, |T_-\rangle, |S_{02}\rangle\}$-basis. The applied magnetic field only has a net effect on the polarized states $|T_\pm\rangle$; for the remaining states the contribution from the spin-up and spin-down electrons cancel one another. The magnetic field gradient between the dots due to the demagnetization field serves to lift the degeneracy of the $|\uparrow\downarrow\rangle$ and $|\downarrow\uparrow\rangle$ states. The relative electrostatic potential between the dots is taken into account by the detuning parameter ε lowering or raising the energy of the $|S_{02}\rangle$ state. Finally, the $|\uparrow\downarrow\rangle$ and $|\downarrow\uparrow\rangle$ states are tunnel coupled to the $|S_{02}\rangle$ state and vice versa. As the tunneling process does not involve a spin flip, this is not possible for the

triplet states. This results in the DQD qubit Hamiltonian

$$\begin{aligned}\hat{H}_q = & B(|T_+\rangle\langle T_+| - |T_-\rangle\langle T_-|) \\ & + \Delta B(|\uparrow\downarrow\rangle\langle\uparrow\downarrow| - |\downarrow\uparrow\rangle\langle\downarrow\uparrow|) - \varepsilon\,|S_{02}\rangle\langle S_{02}| \\ & + \frac{t}{\sqrt{2}}(|\uparrow\downarrow\rangle\langle S_{02}| - |\downarrow\uparrow\rangle\langle S_{02}|) + h.c.\end{aligned} \tag{4.1}$$

Alternatively, we may write this Hamiltonian as a matrix by making use of Heisenberg's matrix formulation of quantum mechanics, in which quantum mechanical operators in a N-dimensional Hilbert space are represented as NxN-dimensional matrices, and states as N-dimensional column vectors [63]. In this formulation, $\hat{H}_q$ becomes

$$\hat{H}_q = \begin{pmatrix} B & 0 & 0 & 0 & 0 \\ 0 & \Delta B & 0 & 0 & \frac{t}{\sqrt{2}} \\ 0 & 0 & -\Delta B & 0 & -\frac{t}{\sqrt{2}} \\ 0 & 0 & 0 & -B & 0 \\ 0 & \frac{t}{\sqrt{2}} & -\frac{t}{\sqrt{2}} & 0 & -\varepsilon \end{pmatrix}. \tag{4.2}$$

Furthermore, we need to construct new spin excitation and relaxation operators, $\hat{\sigma}_+$ and $\hat{\sigma}_-$ for this choice of basis. These operators only act on the spin in the dot closest to the ferromagnet, consistent with the limited range of the exchange coupling. With this limitation in mind, we obtain

$$\hat{\sigma}_{1,+} = \begin{pmatrix} 0 & 0 & 1 & 0 & 0 \\ 0 & 0 & 0 & 1 & 0 \\ 0 & 0 & 0 & 0 & 0 \\ 0 & 0 & 0 & 0 & 0 \\ 0 & 0 & 0 & 0 & 0 \end{pmatrix},\ \hat{\sigma}_{1,-} = \begin{pmatrix} 0 & 0 & 0 & 0 & 0 \\ 0 & 0 & 0 & 0 & 0 \\ 1 & 0 & 0 & 0 & 0 \\ 0 & 1 & 0 & 0 & 0 \\ 0 & 0 & 0 & 0 & 0 \end{pmatrix}, \tag{4.3}$$

where the subscript 1 denotes that the operators act on spin states of electrons in the dot closest to the ferromagnet.

As in the single spin qubit case, all operators need to be written in the Hilbert space of the combined system. Thus, we redefine $\hat{H}_q = \hat{H}_q^{(1)} + \hat{H}_q^{(2)}$, where $\hat{H}_q^{(1)} = I_N \otimes \hat{H}_q \otimes I_5$ and $\hat{H}_q^{(2)} = I_N \otimes I_5 \otimes \hat{H}_q$. I_N and I_5 are the N-dimensional and 5-dimensional identity matrices, respectively, where N is the number of allowed magnon states in the system. While the parameters in the DQD Hamiltonian of each double dot in principle may differ from the other double dot, we here assume the DQDs to be identical. In Sec. 5.1 we will briefly consider the effect of introducing a small difference between the detuning parameters $\varepsilon_1, \varepsilon_2$ of the two DQDs. Similarly, the spin excitation and relaxation operators for each double dot are constructed as $\hat{\sigma}_{1,\pm}^{(1)} = I_N \otimes \hat{\sigma}_{1,\pm} \otimes I_5$ and $\hat{\sigma}_{1,\pm}^{(2)} = I_N \otimes I_5 \otimes \hat{\sigma}_{1,\pm}$ in the combined Hilbert space. Furthermore, the magnon operators are defined as $\hat{\alpha}^{(\dagger)} = \tilde{\alpha}^{(\dagger)} \otimes I_5 \otimes I_5$, where $\tilde{\alpha}^{(\dagger)}$ is the annihilation (creation) operator for a squeezed magnon excitation in the ferromagnet as defined in Sec. 3.2. This allows us to obtain the interaction Hamiltonian, as in the single qubit case, as

$$\hat{H}_{int} = \sum_{i=1,2} \Big[g_R\Big(\hat{\alpha}^\dagger \hat{\sigma}_{1,-}^{(i)} + \hat{\alpha}\hat{\sigma}_{1,+}^{(i)}\Big) + g_{CR}\Big(\hat{\alpha}^\dagger \hat{\sigma}_{1,+}^{(i)} + \hat{\alpha}\hat{\sigma}_{1,-}^{(i)}\Big)\Big]. \tag{4.4}$$

The ferromagnet Hamiltonian is unchanged by the transition from coupling a single quantum dot to a DQD, and may still be written as in Eq. 3.15. The full system Hamiltonian for two DQDs coupled through a ferromagnet may then be written as

$$\hat{H} = \hat{H}_q + \hat{H}_{int} + \hat{H}_F. \tag{4.5}$$

As mentioned in Sec. 2.5, the actual Hilbert space of this Hamiltonian is too large to be considered in its entirety. In the following derivations we will work in the simplest reduced Hilbert space that still captures the interaction between the DQDs and the ferromagnet by setting $N = 2$ and disregarding any states with magnon occupation numbers $n > 1$. As even this simplification results in a Hamiltonian existing in a 50-dimensional Hilbert space, we will construct and handle the system Hamiltonian in Wolfram Mathematica [64]. To do so we may once again make use of the matrix formulation of quantum mechanics, and represent the Hamiltonian and its basis states as matrices and vectors, respectively. Such vectors and matrices may easily be constructed and manipulated in Mathematica using its symbolic computation capabilities.

Fig. 4.3a shows a schematic of the full Hamiltonian as obtained in Eq. 4.5, each red mark corresponding to a non-zero matrix element. This way of depicting the Hamiltonian, while not giving any information about the actual form of each of the non-zero matrix elements will enable us to visualize how the Hamiltonian consists of blocks and coupling elements between said blocks. This will allow us to identify the subspaces of the Hamiltonian that we wish to decouple using the Schrieffer-Wolff transformation. In Fig. 4.3, meshes have been added to more easily recognize the block structure of the Hamiltonian. The top left and bottom right blocks contain states in the $n = 0$ and $n = 1$ subspaces, respectively, while the top right and bottom left contain coupling terms between these subspaces. We may interpret this Hamiltonian as the sum of an unperturbed Hamiltonian $\hat{H}_0 = \hat{H}_q + \hat{H}_F$, shown schematically in Fig. 4.3b, and a perturbation $\hat{V} = \hat{H}_{int}$, shown in Fig. 4.3c. This allows us to reduce the Hamiltonian to the sum of a part that we understand quite well, i.e. an isolated DQD system and an isolated ferromagnet, and the interaction between the two.

These Hamiltonians are block diagonal and block off-diagonal, respectively. The elements of the block off-diagonal perturbation Hamiltonian are all $V_{ij} \propto g_R, g_{CR}$, as these coupling terms correspond to processes that alter the number of magnon excitations in the system. For magnon energies ω_0 that are significantly larger than the energy splitting of the qubit and the applied magnetic field, the subspaces of states with magnon occupations of $n = 0$ and $n = 1$ are well separated in energy, allowing us to perform a Schrieffer-Wolff transformation to incorporate the effects of the $n = 1$ block into the $n = 0$ block, as detailed in Sec. 2.5. This will allow us to directly assess the effective coupling between states that may be coupled through a state containing a magnon excitation.

For instance, the $|T_+T_-\rangle$ state may relax a spin up in the state of the left dot ($|T_+\rangle$) and excite a magnon through the $g_R\hat{\alpha}^\dagger\hat{\sigma}_{1,-}$ term in the interaction Hamiltonian, resulting in the $|1\ \downarrow\uparrow T_-\rangle$ state. This state may then annihilate its magnon excitation and excite a spin in the state of the right dot ($|T_-\rangle$) through

the $g_R\hat{\alpha}\hat{\sigma}_{1,+}$ term, so that the state transitions to the $|\downarrow\uparrow\uparrow\downarrow\rangle$ state in the $n = 0$ subspace. Through the second order SW transformation, this coupling path, and any other two-step coupling path between states in the $n = 0$ and $n = 1$ subspace, will be included through the appearance of coupling elements between the initial and final states in the $n = 0$ subspace. There are, of course, coupling paths that require four or more steps to return to the initial subspace. These may, as we shall see, be included by performing higher order SW transformations. We begin by performing the transformation to second order.

However, as the unperturbed Hamiltonian contains off-diagonal terms, calculating the generator of the SW transformation is not trivial. To facilitate the calculation, we transform $\hat{H}_0$ into a diagonal form. The off-diagonal in $\hat{H}_0$ terms result from the tunnel coupling between the states in the DQD Hamiltonian $\hat{H}_q$. We therefore need to rewrite $\hat{H}_q$ on a diagonal form. To do so, we perform a second order SW transformation on $\hat{H}_q$ in order to perturbatively include the effect of the tunnel coupling on the $|\uparrow\downarrow\rangle$ and $|\downarrow\uparrow\rangle$ states. Note that the accuracy of this transformation, as described in Sec. 2.5, depends on the energy difference between the $|\uparrow\downarrow\rangle$ / $|\downarrow\uparrow\rangle$ states and the $|S_{02}\rangle$ state being significantly larger than the tunnel coupling between them. Assuming the magnitude of the detuning parameter $|\varepsilon|$ to be larger than the tunnel coupling, we rewrite $\hat{H}_q$ as $\hat{H}_q = \mathcal{H}_0 + \mathcal{V}$, where

$$\begin{aligned}\mathcal{H}_0 &= B(|T_+\rangle\langle T_+| - |T_-\rangle\langle T_-|) \\ &\quad + \Delta B(|\uparrow\downarrow\rangle\langle\uparrow\downarrow| - |\downarrow\uparrow\rangle\langle\downarrow\uparrow|) - \varepsilon\,|S_{02}\rangle\langle S_{02}|\,, \\ \mathcal{V} &= \frac{t}{\sqrt{2}}(|\uparrow\downarrow\rangle\langle S_{02}| - |\downarrow\uparrow\rangle\langle S_{02}|) + h.c.\end{aligned} \tag{4.6}$$

As the unperturbed Hamiltonian $\mathcal{H}_0$ is diagonal, we obtain a generator S_1 for the SW transformation through Eq. 2.31 and perform a second order SW

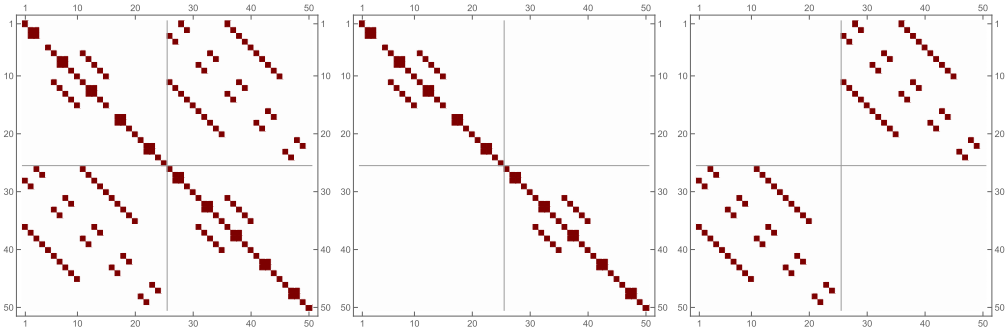

(a) **(b)** **(c)**

Figure 4.3: Schematic plots of **a)** full system Hamiltonian $\hat{H}$, **b)** the unperturbed Hamiltonian $\hat{H}_0 = \hat{H}_q + \hat{H}_F$, and **c)** the perturbation $\hat{V} = \hat{H}_{int}$, in the $|\uparrow\downarrow\rangle$-basis. Each red square corresponds to a non-zero element in the matrix. The operators have dimensions of 50x50, which are separated into four 25x25 blocks. The top left block contains states with magnon occupation number $n = 0$, while the bottom right block contains states with magnon occupation number $n = 1$. The two remaining blocks contain elements that couple the two subspaces.

transformation to obtain the effective Hamiltonian

$$\tilde{H}_q = \begin{pmatrix} B & 0 & 0 & 0 & 0 \\ 0 & \Delta B + \frac{t^2}{2(\Delta B+\varepsilon)} & \frac{t^2\varepsilon}{2(\Delta B^2-\varepsilon^2)} & 0 & 0 \\ 0 & \frac{t^2\varepsilon}{2(\Delta B^2-\varepsilon^2)} & -\Delta B - \frac{t^2}{2(\Delta B-\varepsilon)} & 0 & 0 \\ 0 & 0 & 0 & -B & 0 \\ 0 & 0 & 0 & 0 & \frac{\varepsilon(t^2-\Delta B^2+\varepsilon^2)}{\Delta B^2-\varepsilon^2} \end{pmatrix}, \tag{4.7}$$

for the DQD qubit.

We now argue that the leading order correction due to the tunnel coupling has been taken into account by the shift in energies of the $|\uparrow\downarrow\rangle$ and $|\downarrow\uparrow\rangle$ states, equivalent to the second order energy correction in perturbation theory (Eq. 2.24). The remaining correction, the off-diagonal elements in Eq. 4.7, may be discarded as long as this coupling element is significantly smaller than ΔB, which will be the case for sufficiently negative values of ε. Thus, for the parameter regime that is considered here, we may proceed with only the diagonal elements of $\tilde{H}_q$.

Finally, as the SW transformation performed above slightly alters the states in the DQD basis, the spin excitation and relaxation operators of Eq. 4.3 are no longer strictly correct. To account for this we transform them in the same way, setting

$$\tilde{\sigma}_{1,+} = e^{S_1}\hat{\sigma}_{1,+}e^{-S_1},\ \tilde{\sigma}_{1,-} = e^{S_1}\hat{\sigma}_{1,-}e^{-S_1}, \tag{4.8}$$

retaining terms to second order in S_1. The structure of the full Hamiltonian constructed with these updated operators is shown in Fig. 4.4. As expected, the unperturbed Hamiltonian, visible in the top left and bottom right 25x25 blocks, is now diagonal. Furthermore, we observe that the structure of the coupling between them, in the two off-diagonal blocks, has changed from Fig. 4.3. To understand this, consider the effect of the SW transformation on the states in the chosen basis. In addition to altering the Hamiltonian, the states in the basis have been transformed so that $|\uparrow\downarrow\rangle \to e^{S_1}|\uparrow\downarrow\rangle$, $|\downarrow\uparrow\rangle \to e^{S_1}|\downarrow\uparrow\rangle$, and $|S_{02}\rangle \to e^{S_1}|S_{02}\rangle$. As the $|T_+\rangle$ and $|T_-\rangle$ states are unaffected by the perturbation, they remain unchanged by the transformation. Thus, the transformed spin excitation and relaxation operators of Eq. 4.8 no longer act on the pure $|\uparrow\downarrow\rangle$ and $|\downarrow\uparrow\rangle$ states. Rather, they act on states that are mixtures of the $|\uparrow\downarrow\rangle$, $|\downarrow\uparrow\rangle$, and $|S_{02}\rangle$ states. Therefore, several new coupling elements have been introduced in Fig. 4.4 as compared to the coupling elements shown in Fig. 4.3c. To separate the pure states from the transformed states we will denote the latter as $|\phi\rangle_S$, so that $|\phi\rangle_S = e^{S_1}|\phi\rangle$.

4.2 Effective Hamiltonian in the $|\uparrow\downarrow\rangle$-basis

Having obtained a suitable full system Hamiltonian, in the case that we limit the possible magnon occupation numbers to $n = 0$ and $n = 1$, we now want to obtain an effective low-energy Hamiltonian that adequately reproduces the dynamics of the full Hamiltonian. Obtaining such an effective Hamiltonian will enable us to

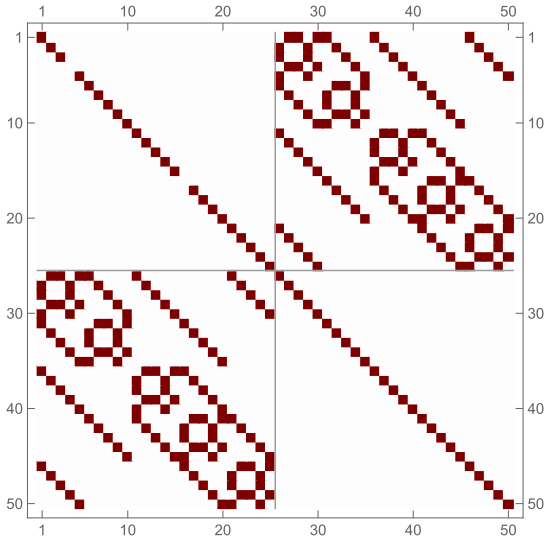

Figure 4.4: Schematic plot of the full system Hamiltonian in the $|\uparrow\downarrow\rangle$-basis. The top left and bottom right 25x25 blocks contain the diagonal unperturbed Hamiltonian for states with magnon occupation numbers of $n = 0$ and $n = 1$, respectively. The remaining two blocks contain the perturbation that couples the two aforementioned blocks.

evaluate how the each of the system parameters influences the behavior of the qubit. This, in turn, will allow us to predict parameter regimes that may enhance the qubit coupling and limit leakage.

We begin by decoupling the $n = 0$ and $n = 1$ magnon subspaces, so that we may consider only states in the $n = 0$ subspace. By applying a SW transformation to the full system Hamiltonian, taking the off-diagonal terms as the perturbation, we may include the effects of the coupling via the $n = 1$ magnon subspace into the Hamiltonian for the $n = 0$ subspace, as described in Sec. 4.1. Note that the accuracy of this transformation depends on the $n = 0$ and $n = 1$ blocks to be well separated in energy, so that the perturbation is much smaller than the energy difference between the states it couples, that is, $|V_{ij}| \ll |E_i - E_j|$. For this to hold we assume the magnon energy ω_0 to be significantly larger than the energy scale of the qubit. This assumption further justifies the limitation on the magnon occupation number; states with higher magnon occupation numbers will be far removed in energy, and transitions to these states become unlikely.

As the unperturbed Hamiltonian $\hat{H}_0 = \tilde{H}_q + \hat{H}_F$ is diagonal, we may simply calculate the second order SW transformation using Eq. 2.36. The resulting effective Hamiltonian is shown schematically in Fig. 4.5a. The $n = 0$ and $n = 1$ blocks are indeed decoupled, and effective coupling elements have been introduced between states within each block.

Turning our focus specifically to the coupling between the $|\uparrow\downarrow\ \downarrow\uparrow\rangle_S$ and $|\downarrow\uparrow\ \uparrow\downarrow\rangle_S$ states, we observe that these states are not coupled in the effective Hamiltonian we have obtained. That is, $\langle\uparrow\downarrow\ \downarrow\uparrow|\tilde{H}|\downarrow\uparrow\ \uparrow\downarrow\rangle_S = \langle\downarrow\uparrow\ \uparrow\downarrow|\tilde{H}|\uparrow\downarrow\ \downarrow\uparrow\rangle_S = 0$, where $\tilde{H}$ is the effective Hamiltonian. This may be seen in Fig. 4.5a, where

these matrix elements have been outlined in black.

To understand this we may turn to the interaction Hamiltonian, consisting of terms that excite or annihilate magnon and spin excitations, one at a time. If we, for the moment, disregard the magnon excitations and view the interaction as simply flipping one spin state at the time, it is evident that two spin flips is insufficient to transition between the $|\uparrow\downarrow\ \downarrow\uparrow\rangle$ and $|\downarrow\uparrow\ \uparrow\downarrow\rangle$ states. As the spin states of four electrons need to be flipped, the shortest possible coupling path is fourth order in the interaction. An example of such a path, disregarding any change in magnon excitations, may be

$$|\uparrow\downarrow\ \downarrow\uparrow\rangle \to |\downarrow\downarrow\ \downarrow\uparrow\rangle \to |\downarrow\uparrow\ \downarrow\uparrow\rangle \to |\downarrow\uparrow\ \uparrow\uparrow\rangle \to |\downarrow\uparrow\ \uparrow\downarrow\rangle\,,$$

where we see that four transtitions are indeed required. Thus, in order for this effective coupling to be included in the $n = 0$ subspace, we need to perform the SW transformation to fourth order.

Performing the transformation as presented in Eq. 2.40 yields an effective Hamiltonian whose structure is shown in Fig. 4.5b. The coupling terms $\langle\uparrow\downarrow\ \downarrow\uparrow|\tilde{H}|\downarrow\uparrow\ \uparrow\downarrow\rangle_S = \langle\downarrow\uparrow\ \uparrow\downarrow|\tilde{H}|\uparrow\downarrow\ \downarrow\uparrow\rangle_S$ are once again outlined in black. While they are too algebraically complicated to be easily displayed here, they are indeed non-zero, confirming that the coupling between the states is fourth order in the perturbation.

Thus, we see that, using the SW transformation we are indeed able to obtain effective coupling elements between the $|\uparrow\downarrow\ \downarrow\uparrow\rangle_S$ and $|\downarrow\uparrow\ \uparrow\downarrow\rangle_S$ states, and we observe that such a coupling is necessarily fourth order in the perturbation. Given the similarity between these states and actual qubit states, we expect to be able to obtain similar results for $|10\rangle$ and $|01\rangle$ when we now proceed in the eigenstate basis.

4.3 In the eigenstate basis

Recall that we encode the qubit in the second and third lowest energy eigenstates of the DQD system. While the $|\uparrow\downarrow\rangle$-basis used in the previous section succeeds in presenting an intuitive picture of the DQD system, it is limited by not explicitly including the qubit states. We now turn to a DQD Hamiltonian constructed from a basis of the eigenstates of the DQD system. To do so we consider first a DQD Hamiltonian in the $\{|T_+\rangle\,, |T_0\rangle\,, |S_{11}\rangle\,, |S_{02}\rangle\,, |T_-\rangle\}$-basis,

$$\hat{H}_q = \begin{pmatrix} B & 0 & 0 & 0 & 0 \\ 0 & 0 & \Delta B & 0 & 0 \\ 0 & \Delta B & 0 & t & 0 \\ 0 & 0 & t & -\varepsilon & 0 \\ 0 & 0 & 0 & 0 & -B \end{pmatrix}. \tag{4.9}$$

From the above Hamiltonian we may already note that the $|T_\pm\rangle$ states are eigenstates of the DQD system, with eigenenergies $E_\pm = \pm B$. Thus, to find the

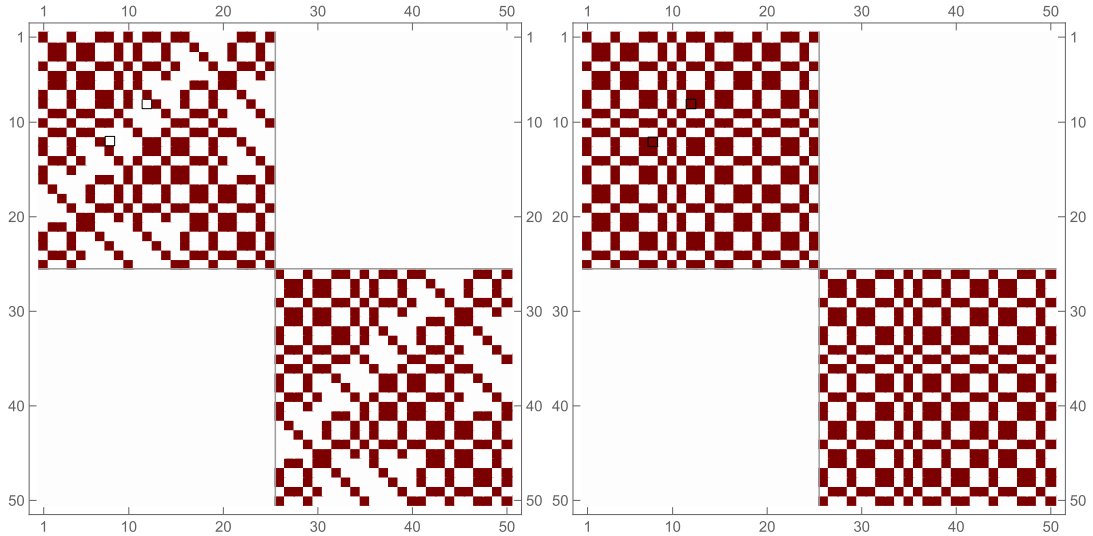

Figure 4.5: Schematic plots of effective full system Hamiltonians in the ↑↓-basis, transformed through **a)** second order and **b)** fourth order SW transformations. The top left block contains states in the $n = 0$ magnon subspace, while the bottom right block contains states in the $n = 1$ magnon subspace. As the remaining two blocks contain no non-zero elements, the $n = 0$ and $n = 1$ blocks are decoupled and may be treated independently. The coupling elements $\langle\uparrow\downarrow\ \downarrow\uparrow|\tilde{H}|\downarrow\uparrow\ \uparrow\downarrow\rangle_S$ and $\langle\downarrow\uparrow\ \uparrow\downarrow|\tilde{H}|\uparrow\downarrow\ \downarrow\uparrow\rangle_S$ are outlined in black in both plots.

remaining eigenstates we proceed by diagonalizing the reduced Hamiltonian in the $\{|T_0\rangle, |S_{11}\rangle, |S_{02}\rangle\}$-basis,

$$\hat{H}'_q = \begin{pmatrix} 0 & \Delta B & 0 \\ \Delta B & 0 & t \\ 0 & t & -\varepsilon \end{pmatrix}. \tag{4.10}$$

Doing so results in the eigenstates

$$\begin{aligned} |\psi_i\rangle &= a_i\,|T_0\rangle + b_i\,|S_{11}\rangle + c_i\,|S_{02}\rangle \\ a_i &= \frac{\Delta B(\varepsilon + E_i)}{tE_i\chi_i} \\ b_i &= \frac{\varepsilon + E_i}{t\chi_i} \\ c_i &= \frac{1}{\chi_i} \\ \chi_i &= \sqrt{1 + \frac{(E_i^2 + \Delta B^2)(E_i + \varepsilon)^2}{E_i^2 t^2}} \end{aligned} \tag{4.11}$$

where $i = \{0, 1, 2\}$ and E_i being the energy of the corresponding state $|\psi_i\rangle$. These energies are the roots of the third degree polynomial

$$\lambda^3 + \varepsilon\lambda^2 - \left(t^2 + \Delta B^2\right)\lambda - \Delta B^2\varepsilon = 0. \tag{4.12}$$

The solutions to this equation may be derived to obtain exact expressions for each eigenenergy. We will, however, proceed with the energies E_i as parameters in the DQD Hamiltonian and insert numerically determined values when needed. Thus we may simply write the DQD Hamiltonian in the $\{|T_+\rangle, |\psi_2\rangle, |\psi_1\rangle, |\psi_0\rangle, |T_-\rangle\}$-basis as

$$\hat{H}_q = \begin{pmatrix} B & 0 & 0 & 0 & 0 \\ 0 & E_2 & 0 & 0 & 0 \\ 0 & 0 & E_1 & 0 & 0 \\ 0 & 0 & 0 & E_0 & 0 \\ 0 & 0 & 0 & 0 & -B \end{pmatrix}, \tag{4.13}$$

where the energies and corresponding eigenstates have been chosen such that $E_0 < E_1 < E_2$. The qubit is encoded in the $|\psi_0\rangle$ and $|\psi_1\rangle$ states, so we define $|0\rangle = |\psi_0\rangle$, $|1\rangle = |\psi_1\rangle$, and $|2\rangle = |\psi_2\rangle$.

As in the $|\uparrow\downarrow\rangle$-basis, we need to rewrite the spin excitation operators of the interaction Hamiltonian for this choice of basis. This yields

$$\hat{\sigma}_+ = \begin{pmatrix} 0 & \frac{a_2-b_2}{\sqrt{2}} & \frac{a_1-b_1}{\sqrt{2}} & \frac{a_0-b_0}{\sqrt{2}} & 0 \\ 0 & 0 & 0 & 0 & \frac{a_2+b_2}{\sqrt{2}} \\ 0 & 0 & 0 & 0 & \frac{a_1+b_1}{\sqrt{2}} \\ 0 & 0 & 0 & 0 & \frac{a_0+b_0}{\sqrt{2}} \\ 0 & 0 & 0 & 0 & 0 \end{pmatrix}, \; \hat{\sigma}_- = \begin{pmatrix} 0 & 0 & 0 & 0 & 0 \\ \frac{a_2-b_2}{\sqrt{2}} & 0 & 0 & 0 & 0 \\ \frac{a_1-b_1}{\sqrt{2}} & 0 & 0 & 0 & 0 \\ \frac{a_0-b_0}{\sqrt{2}} & 0 & 0 & 0 & 0 \\ 0 & \frac{a_2+b_2}{\sqrt{2}} & \frac{a_1+b_1}{\sqrt{2}} & \frac{a_0+b_0}{\sqrt{2}} & 0 \end{pmatrix}. \tag{4.14}$$

Note that none of the c_i-components appear in these operators; this is to be expected as the excitation or relaxation of a spin only affects states in the (1,1) charge configuration. As with the eigenenergies, we proceed with the variables a_i, b_i, and c_i rather than inserting their full expressions, and keep in mind that they all depend on t, ε, and ΔB. While this does obscure the relations between the physical parameters of the system and the variables in the Hamiltonian, it also greatly simplifies calculations and allows us to maintain manageable expressions in the forthcoming analysis. We may then reinsert the actual expressions at the end of our calculations.

Restricting our analysis to systems hosting either $n = 0$ or $n = 1$ magnons, we construct the 50x50 Hamiltonian shown schematically in Fig. 4.6. As expected it consists of two diagonal blocks of states with magnon occupation numbers $n = 0$ and $n = 1$, respectively, and two off-diagonal blocks of coupling elements $V_{ij} \propto (a_k \pm b_k)g_R, g_{CR}$. By comparison to Fig. 4.4, we see that the structure of the Hamiltonian in the eigenstate basis is quite similar to that of the Hamiltonian in the $|\uparrow\downarrow\rangle$-basis for the transformed DQD Hamiltonian $\tilde{H}_q$. This is consistent with the earlier arguments on the similarities of the $|\uparrow\downarrow\rangle$ and $|\downarrow\uparrow\rangle$ states to the actual eigenstates of the Hamiltonian.

4.4 Effective Hamiltonian in the eigenstate basis

As in Sec. 4.2, we wish to obtain an effective Hamiltonian that reproduces the behavior of the qubits as determined by the full system Hamiltonian. Specifically,

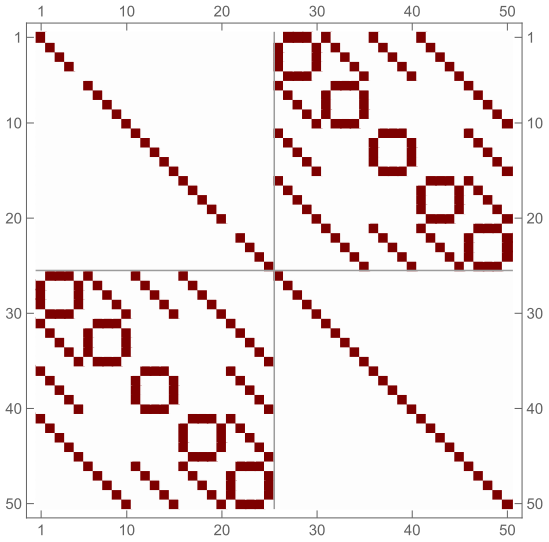

Figure 4.6: Schematic plot of the full system Hamiltonian in the eigenstate basis. The two blocks on the diagonal correspond to the $n = 0$ and $n = 1$ magnon subspaces, respectively, while the off-diagonal blocks contain terms coupling these subspaces.

we are interested in the behavior of the system when initialized in the $|10\rangle$ and $|01\rangle$ states. The goal of this section is therefore to obtain a Hamiltonian describing the effective coupling between these two states, as well as any leakage out of the qubit subspace.

If we once again require that the magnon energy ω_0 is significantly larger than the qubit splitting energy and the applied magnetic field, we may interpret the Hamiltonian shown in Fig. 4.6 as consisting of a block diagonal unperturbed Hamiltonian, $\hat{H}_0 = \hat{H}_q + \hat{H}_F$, and a block off-diagonal perturbation, $\hat{V} = \hat{H}_{int}$, for which the criterion for the validity of the SW transformation, $|V_{ij}| \ll |E_i - E_j|$, holds. We perform a second order SW transformation as derived in Eq. 2.36 to decouple the $n = 0$ and $n = 1$ magnon subspaces, perturbatively including the effect of the coupling between the two within each of the blocks. The result of this transformation is presented schematically in Fig. 4.7a. Once again, we see that the subspaces are decoupled, but as in the $|\uparrow\downarrow\rangle$-basis, the coupling elements between the $|01\rangle$ and $|10\rangle$ states, outlined in black, are zero. This implies that, like the transition between the $|\uparrow\downarrow\ \downarrow\uparrow\rangle$ and $|\downarrow\uparrow\ \uparrow\downarrow\rangle$ states, the transition between $|01\rangle$ and $|10\rangle$ requires at least four actions by the perturbation $\hat{H}_{int}$. If we recall the discussion on the close relation between the $|\uparrow\downarrow\rangle$ and $|\downarrow\uparrow\rangle$ states and the eigenstates in the beginning of the chapter, this is to be expected.

We perform the SW transformation to fourth order to obtain an effective Hamiltonian $\tilde{H}$, which is plotted schematically in Fig. 4.7b. The coupling terms $\langle 01|\tilde{H}|10\rangle = \langle 10|\tilde{H}|01\rangle$ are once again outlined in black. We observe that they are indeed non-zero, and while they are too large to be easily included here, we note that they are fourth order in the coupling terms g_R, g_{CR}, as expected.

Having decoupled the subspaces with different magnon occupation numbers we may proceed with only the $n = 0$ subspace. We now show that, by considering

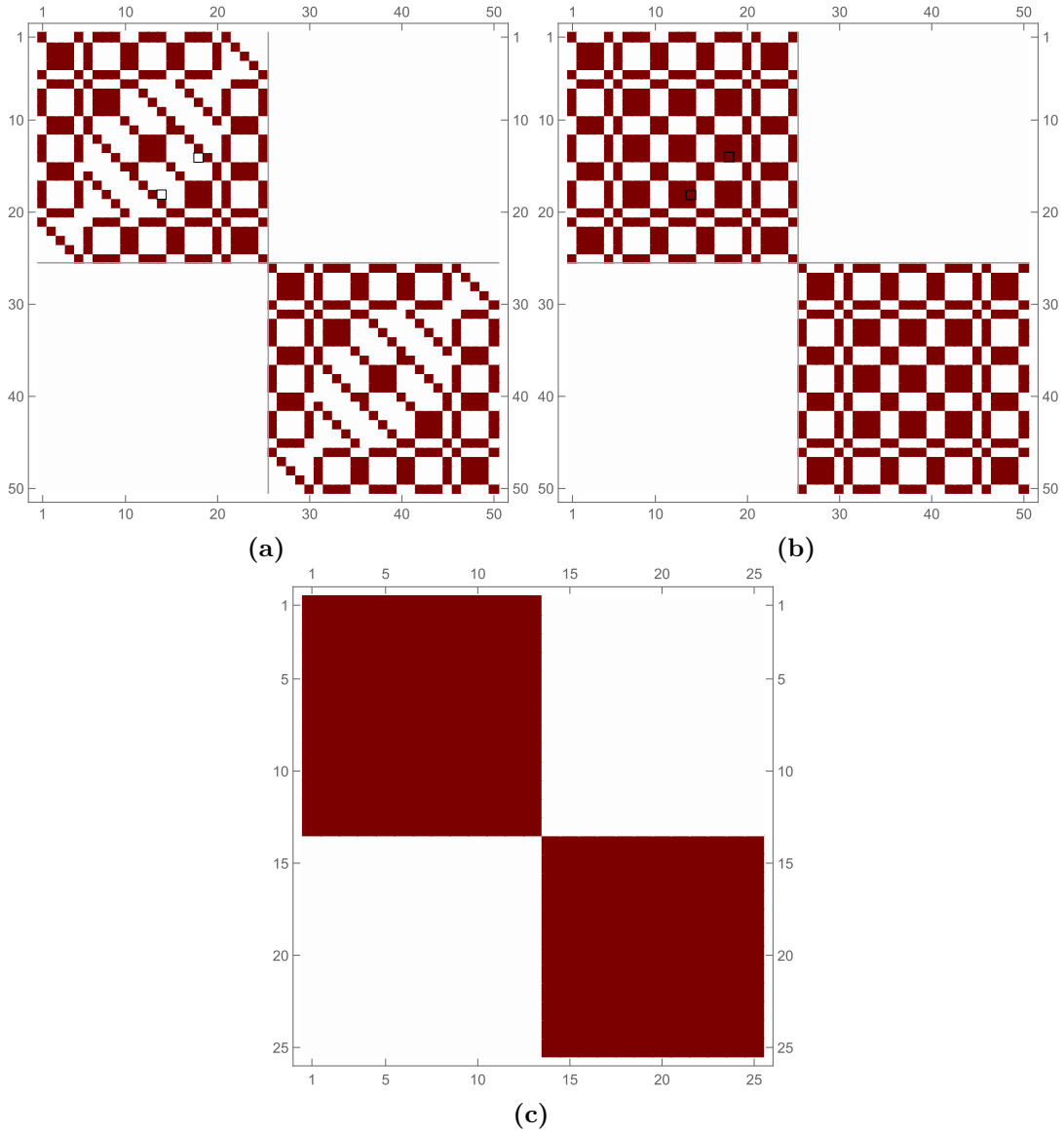

Figure 4.7: Schematic plots of effective Hamiltonians in the eigenstate basis, transformed through **a)** second order and **b)** fourth order SW transformations. The top left block contains states in the $n = 0$ magnon subspace, while the bottom right block contains states in the $n = 1$ magnon subspace. As the remaining two blocks contain no non-zero elements, the $n = 0$ and $n = 1$ blocks are decoupled and may be treated independently. The coupling elements $\langle 01|\tilde{H}|10\rangle$ and $\langle 10|\tilde{H}|01\rangle$ are outlined in black in both **a)** and **b)**. In **c)** we show a schematic plot of the reorganized top left block of the Hamiltonian in **b)**. Note that, while the plots in **a)** and **b)** have dimensions of 50x50, the plot in **c)** has dimensions of 25x25, and only depicts the $n = 0$ subspace.

the rotating and counter-rotating terms in the interaction Hamiltonian more closely, and specifically the effect they have on the total number of excitations of the system, we may further divide this into two decoupled subspaces. In this context, the excitations in question may be either spin states or squeezed magnons.

The rotating term $g_R(\hat{\alpha}^\dagger\hat{\sigma}_- + \hat{\alpha}\hat{\sigma}_+)$ exchanges a spin excitation for a magnon excitation, or vice versa. Thus, the rotating coupling conserves the total excitation number. The counter-rotating term $g_{CR}(\hat{\alpha}^\dagger\hat{\sigma}_+ + \hat{\alpha}\hat{\sigma}_-)$, however, describes the simultaneous relaxation or excitation of a spin and a magnon, thus changing the total number of excitations by ± 2. As only transitions changing the number of excitations by 0 or ± 2 are possible, the parity of excitations in the system is conserved. This entails that any even (odd) parity state only couples to other even (odd) states, creating two decoupled subspaces.

Consider the excitation numbers of each of the states in the DQD Hamiltonian. The $|T_0\rangle$, $|S_{11}\rangle$, and $|S_{02}\rangle$ states all carry net zero spin, being equal parts spin-up and spin-down. Therefore, as the $|0\rangle$, $|1\rangle$, and $|2\rangle$ states are superpositions of states with net zero excitations, they too carry net zero excitations. The polarized triplet states $|T_\pm\rangle$, on the other hand, carry a net spin of ± 1.

We now consider the combined excitation numbers of the states in the $n = 0$ subspace, which is summarized in Table 4.1. Any state that is a combination of two of the $|0\rangle$, $|1\rangle$, and $|2\rangle$ states, for instance the $|01\rangle$ state, will carry zero total excitation. The same is true for the $|T_+T_-\rangle$ and $|T_-T_+\rangle$ states. Any state that is a combination of one of the $|T_\pm\rangle$ states and one of the $|0, 1, 2\rangle$ states, will carry a total excitation number of ± 1. Finally, the $|T_+T_+\rangle$ and $|T_-T_-\rangle$ states carry a total excitation number of ± 2, respectively.

In Fig. 4.7c we include a schematic plot of the $n = 0$ subspace wherein we have reorganized the basis to show that the even and odd parity subspaces are indeed decoupled. The top left block in Fig. 4.7c contains the even parity states $|11\rangle$, $|10\rangle$, $|01\rangle$, $|00\rangle$, $|T_+T_-\rangle$, $|T_-T_+\rangle$, $|T_+T_+\rangle$, $|22\rangle$, $|20\rangle$, $|21\rangle$, $|02\rangle$, $|12\rangle$, and $|T_-T_-\rangle$. As the qubit states we are interested in, being states containing $|0\rangle$ and $|1\rangle$, are included in the even parity subspace we may safely disregard the odd parity subspace. Doing so, we have obtained a 13x13 effective Hamiltonian describing the coupled qubit system.

In order to understand the suitability of the proposed system for qubit coupling,

	$\|T_+\rangle$ (+1)	$\|2\rangle$ (0)	$\|1\rangle$ (0)	$\|0\rangle$ (0)	$\|T_-\rangle$ (−1)
$\|T_+\rangle$ (+1)	+2	+1	+1	+1	0
$\|2\rangle$ (0)	+1	0	0	0	-1
$\|1\rangle$ (0)	+1	0	0	0	-1
$\|0\rangle$ (0)	+1	0	0	0	-1
$\|T_-\rangle$ (−1)	0	-1	-1	-1	-2

Table 4.1: Table showing the combined excitation number of each of the 25 states in the $n = 0$ subspace of the system Hamiltonian. The numbers in parentheses denote the excitation number carried by each of the five DQD states.

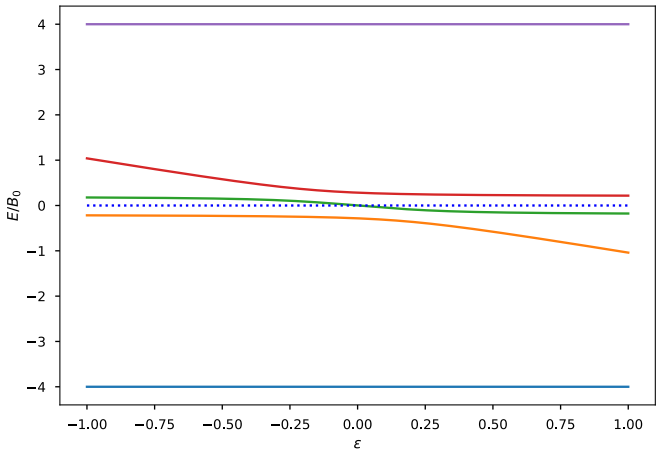

Figure 4.8: Numerically calculated energy spectrum of the DQD system as a function of the detuning parameter ε. Starting from the top, the energies correspond to the $|T_+\rangle$, $|2\rangle$, $|1\rangle$, $|0\rangle$, and $|T_-\rangle$ states, as described in Eq. 4.13. The tunnel coupling is $t = 0.2B_0$. As in Fig. 4.2, we include a magnetic field gradient across the DQD system, setting $\Delta B = 0.2B_0$. The externally applied magnetic field is set to $B = 4B_0$. The dotted line depicts the zero-point energy.

we need to be able to describe the switching rate between $|01\rangle$ and $|10\rangle$, as well as the leakage out of the qubit subspace. We limit this analysis to a regime where both the applied magnetic field B and the magnon energy ω_0 are significantly larger than the qubit splitting. The effect of the increased magnetic field is shown in Fig. 4.8, where the strength of the external field has been quadrupled from Fig. 4.2. The states $|0\rangle$, $|1\rangle$, and $|2\rangle$ remain unchanged by this increase, but the energy difference between these and the $|T_+\rangle$ and $|T_-\rangle$ states is increased. This is consistent with Eqs. 4.12 and 4.13, where the energies $E_{0,1,2}$ are independent of the external magnetic field. Furthermore, we require the detuning parameter ε to be negative.

For large B, the $|T_+T_+\rangle$ and $|T_-T_-\rangle$ states are far removed from the $|01\rangle$ and $|10\rangle$ states in energy, and any transition probability to these states may safely be neglected. The remaining states in the 13x13 Hamiltonian are significantly closer in energy, however, and require more careful consideration. Using the DQD energy spectrum in Fig. 4.8, we may construct a diagram of the energies of the combined $|0\rangle$ and $|1\rangle$ states, along with other combinations of states that will be close in energy. This diagram is shown in Fig. 4.9. As the energies of the $|0\rangle$ and $|1\rangle$ state are slightly asymmetric around the zero-point energy in Fig. 4.8, the energy of the combined $|01\rangle$ and $|10\rangle$ is slightly below zero. The combined states that are closest in energy are the $|T_+T_-\rangle$ and $|T_-T_+\rangle$ states, whose energies are exactly zero. For $t = \Delta B = 0.2B_0$ and $\varepsilon = -0.5B_0$, the energy difference between these states is $\Delta E_1 = |E_{|T_+T_-\rangle} - E_{|01\rangle}| = 0.078B_0$.

As we can see from Fig. 4.9, the remaining states are all farther removed in energy. The energy difference between the $|01\rangle$ / $|10\rangle$ states and the $|11\rangle$

and $|00\rangle$ states is, for the same parameters as above, $\Delta E_2 = |E_{|11\rangle} - E_{|01\rangle}| = |E_{|00\rangle} - E_{|01\rangle}| = 0.38B_0$. To first approximation, the coupling between $|01\rangle$ and $|10\rangle$ and all states except the $|T_+T_-\rangle$ and $|T_-T_+\rangle$ states may then be disregarded. We therefore consider a 4x4 Hamiltonian in the $\{|10\rangle, |01\rangle, |T_+T_-\rangle, |T_-T_+\rangle\}$ basis, neglecting coupling to the remaining 7 states in the above 13x13 Hamiltonian. This Hamiltonian allows us to evaluate the coupling between the $|01\rangle$ and $|10\rangle$ states and the leakage to the states outside the qubit subspace that are closest in energy.

The 4x4 Hamiltonian obtained here will, in Sec. 5.2 be compared with the results of a numerical calculation of the time evolution of the system, to assess the degree to which this effective Hamiltonian is able to capture the behavior of the full coupled qubit system. The numerical analysis the effective Hamiltonian will be compared to is presented in Sec. 5.1.

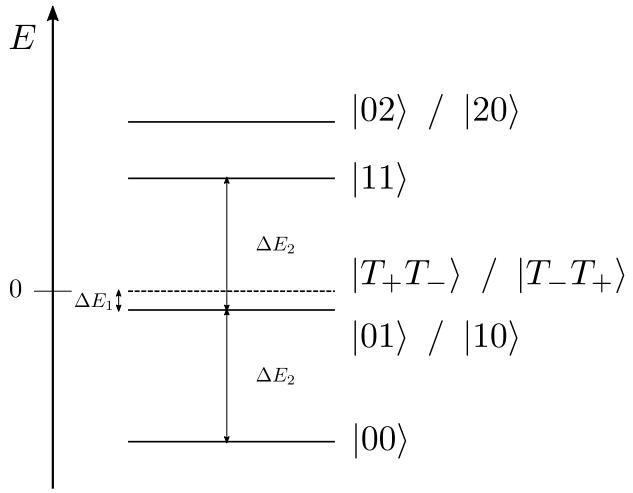

Figure 4.9: Diagram of the energy levels of the $|00\rangle$, $|01\rangle$, $|10\rangle$, $|T_+T_-\rangle$, $|T_-T_+\rangle$, $|11\rangle$, $|02\rangle$, and $|20\rangle$ states, based on the DQD energy spectrum in Fig. 4.8. States that are higher in energy than $|02\rangle$ and $|20\rangle$ have been omitted from the diagram. The energy difference between the $|T_+T_-\rangle$ / $|T_-T_+\rangle$ states and the $|01\rangle$ / $|10\rangle$ states is denoted by ΔE_1. For $t = \Delta B = 0.2B_0$ and $\varepsilon = -0.5$, this energy difference is $\Delta E_1 = 0.078B_0$. Similarly, the energy difference between to the $|11\rangle$ and $|00\rangle$ states is denoted by ΔE_2. For the same parameters, this energy difference is $\Delta E_2 = 0.38B_0$.

Chapter 5

Results

5.1 Numerical simulations of the DQD system

This section presents numerical simulations of the time evolution of the ferromagnetically coupled DQD system for different parameter regimes. As in Sec. 3.4, we solve the TDSE numerically using the QuTiP *sesolve* function applied on a matrix Hamiltonian constructed from Eq. 4.5. We show that the proposed system exhibits coherent switching and low leakage for a wide range of parameters. As for the single spin case, the code used in these simulations may be found in Appendix A.2

As in Sec. 3.4, we consider magnon energies tuned both on and off resonance with the qubit splitting, and systems both with and without the counter-rotating terms g_{CR}. The energy scale in the following simulations, while in principle abitrary, is defined relative to the energy of the $|T_+\rangle$ state for a specific magnetic field $B = B_0$. Furthermore, for ease of notation, the figures in the following sections will have occupation probabilities denoted simply by the state label $|\chi\rangle$, rather than the more precise $|\langle\psi(t)|\chi\rangle|^2$, $|\psi(t)\rangle$ being the state of the system at time t. Unless stated otherwise, the simulations presented in this section used system Hamiltonians limited to containing a maximum of 6 magnon excitations. As the matrix Hamiltonian associated with each magnon occupation number is 25x25, unlike the 4x4 Hamiltonians in the single spin qubit case, the computation time for each simulation rises more steeply than in the previous section. Simulations of the DQD system also require significantly more time-steps than the single spin qubit system, further increasing the computation time of each simulation. This limit on the number of magnon excitations is therefore chosen in order to be able to compute the simulations in a reasonable time-scale. In the following simulations, the strength of the tunnel coupling between the dots was set to $t = 0.2B_0$, and the magnetic field gradient due to the demagnetization field was similarly set to $\Delta B = 0.2B_0$.

We first consider a system where the magnon energy is tuned to be resonant with the qubit splitting, which we define as $\omega_q = E_1 - E_0$. Setting $\omega_0 = \omega_q$, we initialize in the $|01\rangle$ state and evaluate the occupation probabilities of the $|11\rangle$, $|01\rangle$, $|10\rangle$, and $|00\rangle$ as the system evolves in time. The simulation is carried

out both in the absence and presence of magnon squeezing, that is, including and excluding the counter-rotating coupling terms, respectively. The simulation results shown in Fig. 5.1a were obtained using $g_{CR} = 0$, while the results in Fig. 5.1b were obtained using $g_{CR} = 0.1B_0$. In both cases, the applied magnetic field was set to $B = 1B_0$, the detuning parameter was set to $\varepsilon = -0.3B_0$, and the rotating coupling constant was set to $g_R = 0.1B_0$.

Recall that, for magnon energies resonant with the qubit splitting, the single spin qubit system displayed significant leakage out of the qubit subspace. Furthermore, the introduction of magnon squeezing caused the time evolution of the qubit states to become quite chaotic. These issues are not present for the DQD system. In Fig. 5.1a, we observe that the qubit states are able to evenly mix, showing no sign of significant leakage. This is in contrast to the leakage visible in Fig. 3.2. By comparing Figs. 3.3 and 5.1b, we see that the DQD system, unlike the single spin qubit system, maintains coherent switching at resonant magnon energies even when including anisotropy and magnon squeezing. Apart from a shift in the switching frequency, the DQD system exhibits well-behaved switching and even mixing both for $g_{CR} = 0$ and $g_{CR} = 0.1B_0$. The frequency shift is due to a change in the coupling strength between the $|01\rangle$ and $|10\rangle$ states; when magnon squeezing is included, additional coupling paths between $|01\rangle$ and $|10\rangle$ become available through the $\hat{\alpha}^\dagger\hat{\sigma}_+$ and $\hat{\alpha}\hat{\sigma}_-$ terms in the Hamiltonian, altering the total coupling. Note that the slight broadening of the lines in Fig. 5.1 is due to low amplitude, high frequency oscillations in the occupation probabilities of the $|01\rangle$ and $|10\rangle$ states, similar to the oscillations visible in Fig. 3.4.

We now consider a system where the magnon energy is tuned well away from resonance, setting $\omega_0 = 4B_0$. Once again, we calculate the time evolution of the $|11\rangle$, $|01\rangle$, $|10\rangle$, and $|00\rangle$ states, initialized in the $|01\rangle$ state, both with and without the counter-rotating term g_{CR}. The detuning parameter is set to $\varepsilon = -0.5B_0$,

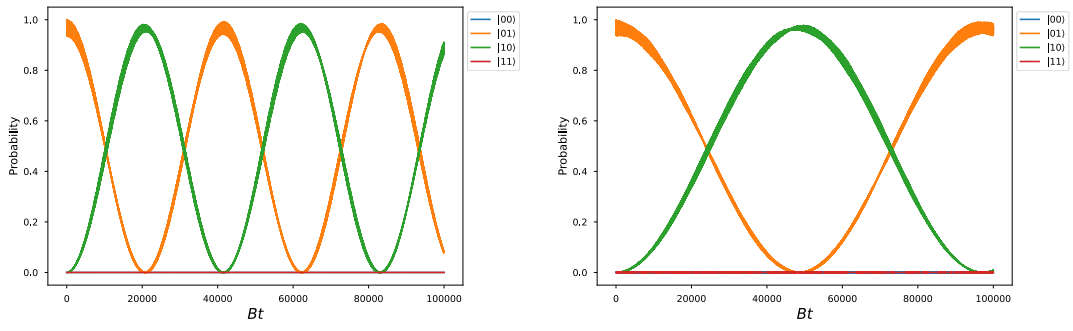

(a) **(b)**

Figure 5.1: Time evolution of the $|11\rangle$, $|01\rangle$, $|10\rangle$, and $|00\rangle$ states, initialized in $|01\rangle$. The magnon energy is resonant with the qubit splitting, $\omega_0 = \omega_q$, the applied magnetic field is $B = 1B_0$, and the detuning parameter is $\varepsilon = -0.3B_0$. Both simulations use $g_R = 0.1B_0$, $t = 0.2B_0$ and $\Delta B = 0.2B_0$. The counter-rotating terms is set to **a)** $g_{CR} = 0$ and **b)** $g_{CR} = 0.1B_0$.

and the applied magnetic field is $B = 1B_0$. These simulations are presented in Figs. 5.2a and 5.2b for $g_{CR} = 0$ and $g_{CR} = 0.1B_0$, respectively. In both cases, we observe well behaved coherent switching between, and even mixing of, the $|01\rangle$ and $|10\rangle$ states, indicating that any leakage out of the qubit subspace is minimal. This is similar to the behavior of the single spin qubit for detuned magnon energies, as shown in Figs. 3.4a and 3.4b. As in these figures, we observe that the only effect of introducing squeezed magnon, setting $g_{CR} = 0.1B_0$, is a slight increase in the switching frequency between the states.

One of the main benefits of encoding the qubit in DQDs rather than in single spin quantum dots is that the requirement for highly localized oscillating magnetic fields are replaced by precised electrical control. However, this precision may indeed pose a challenge in practical implementations of the proposed system. To illustrate this we once again calculate the time evolution of the coupled DQD system initialized in the $|01\rangle$ state, using the same parameters as in Fig. 5.2b. This time, however, we slightly alter the detuning of one of the dots. The time evolution of the occupation probabilities of the $|11\rangle$, $|01\rangle$, $|10\rangle$, and $|00\rangle$ states are plotted in Fig. 5.3. For DQD 1, that is, the DQD initialized in $|0\rangle$, we still set $\varepsilon_1 = -0.50B_0$ in both Figs. 5.3a and 5.3b. For DQD 2, initialized in $|1\rangle$, we in Fig. 5.3a set $\varepsilon_2 = -0.5005B_0$, while we in Fig. 5.3b set $\varepsilon_2 = -0.51B_0$. We observe that, as the difference in the detuning parameter between the two DQD increases, the oscillation between the $|01\rangle$ and $|10\rangle$ states is increasingly suppressed. Note that this effect is not specific to the current choice of parameters; similar results are obtained using different parameters, and in systems with the magnon energy tuned to resonate with the qubit splitting.

This may be understood by considering the requirement for energy to be conserved. Due to the energies of the $|0\rangle$ and $|1\rangle$ states depending on the detuning parameter, the introduction of a difference in detuning parameters between the

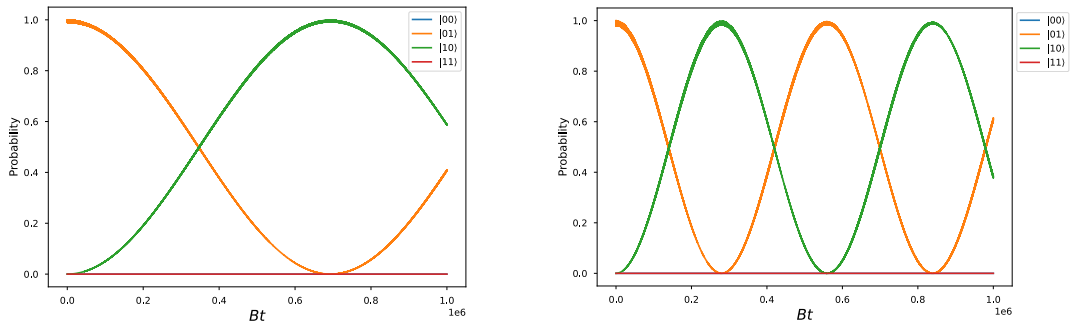

(a) **(b)**

Figure 5.2: Time evolution of the coupled DQD system for **a)** $g_{CR} = 0$ and **b)** $g_{CR} = 0.1B_0$, showing the $|11\rangle$, $|01\rangle$, $|10\rangle$, and $|00\rangle$ states. In both simulations, the external magnetic field was set to $B = 1B_0$, the magnon energy to $\omega_0 = 4B_0$, and the rotating coupling term to $g_R = 0.1B_0$. As before, $t = 0.2B_0$ and $\Delta B = 0.2B_0$. Both simulations were initialized in the $|01\rangle$ state.

qubits lifts the degeneracy of the $|01\rangle$ and $|10\rangle$ states. This sharply reduces the transition probability between the states, consequently reducing the switching frequency. This issue may be overcome by considering qubits coupling strengths that are sufficiently strong to overcome the reduction in the transition probability, but for the system considered here, a slight difference in qubit splitting renders the switching time imperceptibly long, and places strict requirements on the precision of the applied electrostatic voltages on each DQD. The successful implementation of exchange-only quibts implies that this precision is indeed attainable [35], but it does highlight that the benefits of the singlet-triplet qubit over the single spin qubit does come at the cost of increased susceptibility to electric noise [65].

In order to understand the behavior of the coupled DQD system in the parameter regime for which we derived the effective Hamiltonian in Sec. 4.4, we now perform similar simulations as above for an increased applied magnetic field. We initialize in the $|01\rangle$ state, still setting $\omega_0 = 4B_0$ and $\varepsilon = -0.5B_0$, and increase the applied magnetic field to $B = 10B_0$. In these simulations, the Hamiltonian was limited to hosting either $n = 0$ or $n = 1$ magnon excitations. This is done to facilitate comparison with simulations conducted using the effective Hamiltonian derived in Sec. 4.4, for which we assumed the magnon occupation number to be no higher than $n = 1$, and also serves to reduce computation time. For such large magnon energies, states with higher magnon occupation numbers are far removed in energy, reducing the likelihood of any states with higher magnon numbers impacting the qubit coupling. The exception is the $|5\ T_-T_-\rangle$ state, which has an energy of exactly zero for these parameters. However, as this state carries an odd-parity excitation number, it is decoupled from the qubit states. Figs. 5.4a and 5.4b show the time evolution of the $|11\rangle$, $|01\rangle$, $|10\rangle$, and $|00\rangle$ states, for $g_{CR} = 0$ and $g_{CR} = 0.1B_0$, respectively. We see that the well-behaved coherent switching

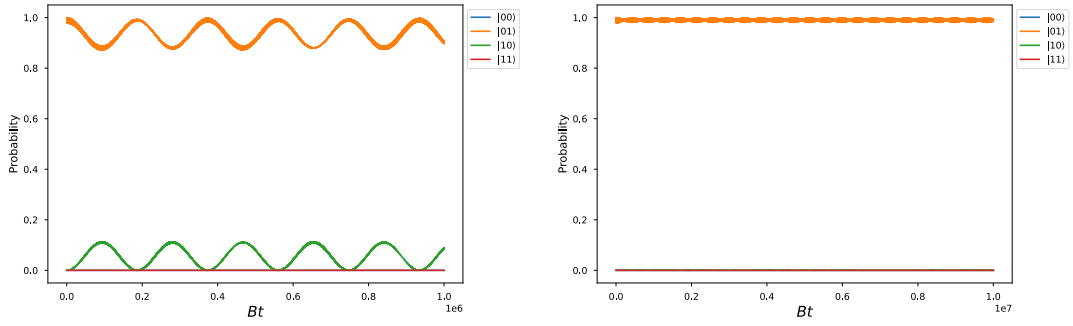

(a) **(b)**

Figure 5.3: Numerically calculated time evolution of the $|11\rangle$, $|01\rangle$, $|10\rangle$, and $|00\rangle$ states, initialized in $|01\rangle$. The calculation was performed using $B = 1B_0$, $\omega_0 = 4B_0$, and $t = \Delta B = 0.2B_0$. A slight difference between the detuning parameter of each DQD was introduced in the calculation. The detuning parameter of the first dot (initialized in $|0\rangle$) is fixed at $\varepsilon_1 = -0.5B_0$ for both plots. In **a)** the detuning parameter of the second dot (initialized in $|1\rangle$) is set to $\varepsilon_2 = -0.5005B_0$. In **b)**, $\varepsilon_2 = -0.51B_0$ was used.

between $|01\rangle$ and $|10\rangle$ states remains for the increased magnetic field, although the frequency is significantly slower than before. As in the previous simulations, the introduction of squeezed magnons by setting $g_{CR} = 0.1B_0$ only alters the oscillation frequency. Besides this shift, the behavior of the coupled qubit system remains largely the same. In Fig. 5.4c, we calculate the occupation probabilities of the $|T_+T_-\rangle$ and $|T_-T_+\rangle$ states. While these occupation probabilities being non-zero indicate leakage from the qubit subspace, the leakage is low enough to not visibly affect the switching of the qubit states.

5.2 Comparing full and effective Hamiltonians

Having derived an effective 4x4 Hamiltonian $\tilde{H}$ for the coupled DQD system for large applied magnetic fields B and magnon energies ω_0 in Sec. 4.4, the goal of this section is to evaluate the accuracy of the obtained Hamiltonian and more closely examine the coupling term between the $|01\rangle$ and $|10\rangle$ states.

We begin by performing a numerical simulation of the time evolution, as in the preceding section, this time using the effective Hamiltonian. Once again, the tunnel coupling and magnetic field gradient is set to $t = \Delta B = 0.2B_0$, and the detuning parameter to $\varepsilon = -0.5B_0$. For the assumptions in the derivation of $\tilde{H}$ to hold, both the applied magnetic field and the magnon energy has to be significantly larger than the qubit splitting, so we set $B = 10B_0$ and $\omega_0 = 4B_0$. Naturally, these are the same parameters used in the simulations shown in Fig. 5.4, enabling us to make a direct comparison between the full 50x50 Hamiltonian and the 4x4 effective Hamiltonian. The result of the simulations using $\tilde{H}$, for both $g_{CR} = 0$ and $g_{CR} = 0.1B_0$, are presented in Figs. 5.5a and 5.5b, respectively. Fig. 5.5c shows the leakage to the $|T_+T_-\rangle$ and $|T_-T_+\rangle$ states as the system evolves in time. By comparison to Fig. 5.4 we see that the effective Hamiltonian accurately reproduces the time evolution of the full 50x50 Hamiltonian, for both $g_{CR} = 0$ and $g_{CR} = 0.1B_0$. The leakage in Fig. 5.5c is larger than that of the full Hamiltonian in Fig. 5.4c, and the time evolution does not match quite as well as that of the $|01\rangle$ and $|10\rangle$ states. However, the leakage remains small enough to not significantly affect the switching of the qubits.

Having justified the assumptions made in the derivation of $\tilde{H}$ and established that it accurately reproduces the behavior of the coupled DQD system in the chosen parameter regime, we may now take a closer look at the coupling and leakage terms in this effective Hamiltonian. We consider the coupling between the $|01\rangle$ and $|10\rangle$ states, $\langle 01|\tilde{H}|10\rangle$, and the terms describing the leakage to the $|T_+T_-\rangle$ and $|T_-T_+\rangle$ states, $\langle 01|\tilde{H}|T_\pm T_\mp\rangle$ and $\langle 10|\tilde{H}|T_\pm T_\mp\rangle$. Note that, as $\tilde{H}$ in addition to being Hermitian is also real-valued, the Hamiltonian is symmetric: $\langle\phi_i|\tilde{H}|\phi_j\rangle = \langle\phi_j|\tilde{H}|\phi_i\rangle$.

As we have assumed B and ω_0 to be significantly larger than the qubit splitting, we may expand the elements of $\tilde{H}$ as a power series in B^{-1} and ω_0^{-1}, retaining only terms to leading order. This allows us to obtain an expression for the coupling

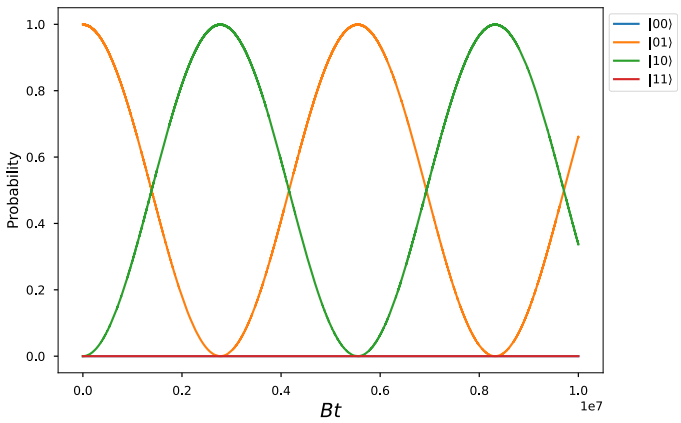

(a)

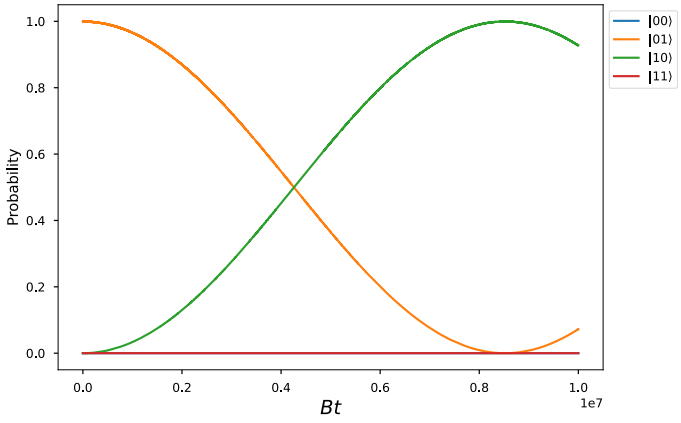

(b)

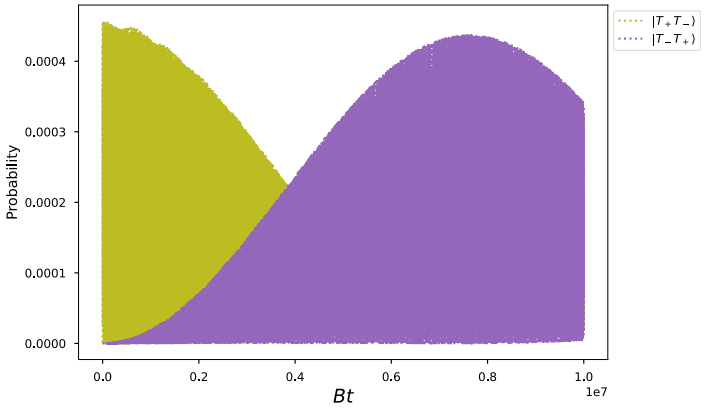

(c)

Figure 5.4: Time evolution of the coupled DQD system for **a)** $g_{CR} = 0$ and **b)** $g_{CR} = 0.1B_0$, showing the $|11\rangle$, $|01\rangle$, $|10\rangle$, and $|00\rangle$ states. In both simulations, the external magnetic field was set to $B = 10B_0$, the magnon energy to $\omega_0 = 4B_0$, and the detuning parameter to $\varepsilon = -0.5B_0$. For the rotating coupling we used $g_R = 0.1B_0$. As before, $t = 0.2B_0$ and $\Delta B = 0.2B_0$. Both simulations were initialized in the $|01\rangle$ state. **c)** Plot of the occupation probabilities of the $|T_+T_-\rangle$ and $|T_-T_+\rangle$ states calculated using the same parameters as in **b)**.

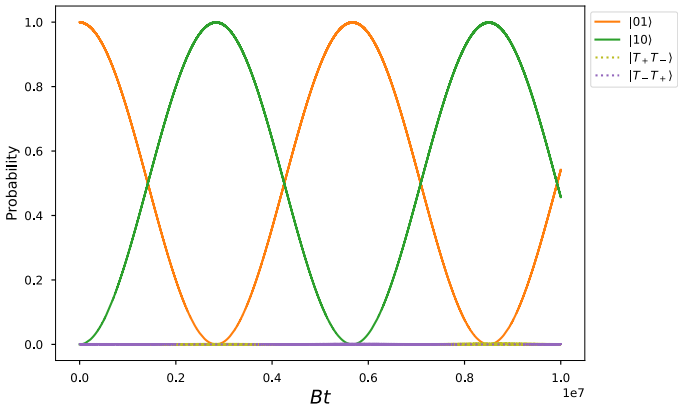

(a)

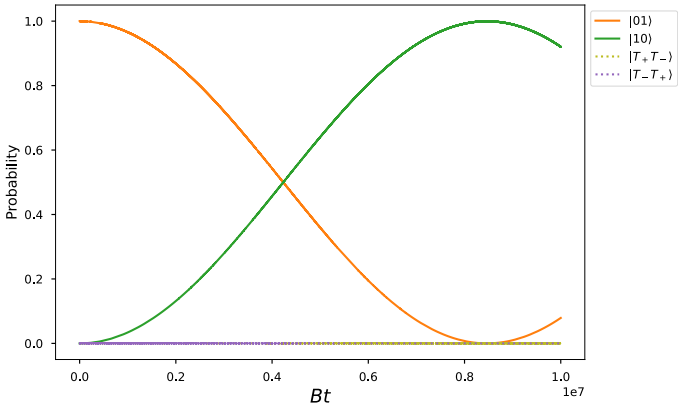

(b)

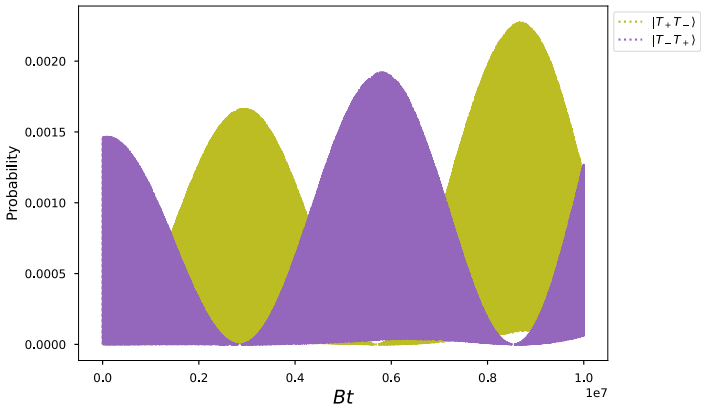

(c)

Figure 5.5: Time evolution of the $|01\rangle$, $|10\rangle$, $|T_+T_-\rangle$, and $|T_-T_+\rangle$ states calculated using the effective Hamiltonian $\tilde{H}$, initialized in $|01\rangle$. To comply with the assumptions in the derivation of this Hamiltonian, the applied magnetic field was set to $B = 10B_0$ and the magnon energy to $\omega_0 = 4B_0$. The rotating coupling was set to $g_R = 0.1B_0$, while the counter-rotating coupling was **a)** $g_{CR} = 0$ and **b)** $g_{CR} = 0.1B_0$. **c)** Plot of the occupation probabilities of the $|T_+T_-\rangle$ and $|T_-T_+\rangle$ states calculated using the same parameters as in **b)**.

between the $|01\rangle$ and $|10\rangle$ states as

$$\begin{aligned}\langle 01|\tilde{H}|10\rangle =&\frac{E_1E_0+\Delta B^2}{\Sigma_1\Sigma_0}[\frac{(E_1-\Delta B)(E_0-\Delta B)}{(B+\omega_0)^3}g_{CR}^4\\&-\frac{(E_1+\Delta B)(E_0+\Delta B)}{(B-\omega_0)^3}g_R^4\\&+2\frac{B(E_1+E_0)\Delta B+2\omega_0(E_1E_0+\Delta B^2)}{(B-\omega_0)^2(B+\omega_0)^2}g_{CR}^2g_R^2],\end{aligned}\tag{5.1}$$

where $\Sigma_i = \Delta B^2 + E_i^2(1+\frac{t^2}{(E_i+\varepsilon)^2})$ for $i = 0, 1$. For the leakage terms to the $|T_+T_-\rangle$ and $|T_-T_+\rangle$ states we obtain

$$\begin{aligned}\langle 01|\tilde{H}|T_+T_-\rangle =& \langle 10|\tilde{H}|T_-T_+\rangle\\=&\frac{(E_1-\Delta B)(E_0+\Delta B)(E_1+\varepsilon)(E_0+\varepsilon)}{2E_1E_0t^2\chi_1\chi_0(B-\omega_0)(B+\omega_0)}\\&\cdot[B(g_{CR}^2-g_R^2)-\omega_0(g_{CR}^2+g_R^2)]\end{aligned}\tag{5.2}$$

$$\begin{aligned}\langle 01|\tilde{H}|T_-T_+\rangle =& \langle 10|\tilde{H}|T_+T_-\rangle\\=&\frac{(E_1+\Delta B)(E_0-\Delta B)(E_1+\varepsilon)(E_0+\varepsilon)}{2E_1E_0t^2\chi_1\chi_0(B-\omega_0)(B+\omega_0)}\\&\cdot[B(g_{CR}^2-g_R^2)-\omega_0(g_{CR}^2+g_R^2)],\end{aligned}\tag{5.3}$$

where $\chi_{0,1}$ are as defined in Eq. 4.11. Note that the expression in the square brackets above appears in both Eqs. 5.2 and 5.3. Recall that the coupling constants g_R and g_{CR} may be tuned by manipulating the magnetic anisotropy of the ferromagnet. Therefore, we see that we are able to completely suppress the leakage to both $|T_+T_-\rangle$ and $|T_-T_+\rangle$ by choosing coupling constants so that

$$B(g_{CR}^2-g_R^2)-\omega_0(g_{CR}^2+g_R^2)=0.\tag{5.4}$$

This equations holds for coupling constants g_R and g_{CR} such that $g_{CR} = \pm g_R\sqrt{\frac{B+\omega_0}{B-\omega_0}}$. As g_{CR} only appears in even powers, we may disregard the sign and choose for instance $g_{CR} = g_R\sqrt{\frac{B+\omega_0}{B-\omega_0}}$. Inserting this into Eq. 5.1, we obtain

$$\langle 01|\tilde{H}|10\rangle = 2\frac{E_1E_0+\Delta B^2}{\Sigma_2\Sigma_3}g_R^4,\tag{5.5}$$

which, importantly, is non-zero. Therefore, by careful tuning of the coupling constants g_R and g_{CR}, we completely suppress leakage to these states, while maintaining coupling between the qubit states $|01\rangle$ and $|10\rangle$. This amounts to decomposing the 4x4 effective Hamiltonian into two 2x2 blocks containing decoupled subspaces. Thus, any state initialized within the qubit subspace spanned by $|01\rangle$ and $|10\rangle$ will inevitably remain within this subspace as any leakage paths in the effective Hamiltonian are eliminated. Naturally, this is not strictly true for the full 50x50 Hamiltonian. For this Hamiltonian, the coupling

to $|T_+T_-\rangle$ and $|T_-T_+\rangle$, while reduced, will remain non-zero. This is due to the approximations made in the SW transformation and the truncated series expansion above. Furthermore, the coupling to the remaining even parity states is not necessarily diminished by this choice of coupling constants. These states are, however, farther removed in energy, rendering leakage less likely.

As a demonstration, we once again calculate the time evolution of the system using the 4x4 effective Hamiltonian. All the parameters apart from the counter-rotating coupling constant remain unchanged from the ones used in Fig. 5.5, apart from g_{CR}, which is tuned so that leakage is suppressed. For the given parameters, this amounts to setting $g_{CR} = 0.153B_0$, a slight increase from the previous value. The resulting time evolution is presented in Fig. 5.6. While decidedly slower than for $g_{CR} = 0.1B_0$, we once more observe coherent switching between the $|01\rangle$ and $|10\rangle$ states, and, as expected, no occupation of the $|T_+T_-\rangle$ and $|T_-T_+\rangle$ states.

Finally, this choice of counter-rotating coupling presents us with an opportunity to both evaluate the actual leakage from the qubit subspace in this setup, and simultaneously visualize the difference between the effective and full Hamiltonians. In Fig. 5.7, we calculate the occupation probabilities of the $|T_+T_-\rangle$ and $|T_-T_+\rangle$ states using the full 50x50 Hamiltonian. The system is initialized in $|01\rangle$ with the same parameters as in Fig. 5.6, that is, parameters that in the effective Hamiltonian would result in exactly zero leakage. We observe from Fig. 5.7 that, while the leakage is non-zero, it is several orders of magnitude lower than in Fig. 5.4c, where $g_{CR} = 0.1B_0$ was used. Furthermore, from the magnitude of the leakage, we may surmise that the effective Hamiltonian in this case reproduces the behavior of the 50x50 Hamiltonian with a deviation on the order of 10^{-6}. This confirms both that the choice of coupling constants derived from the effective Hamiltonian indeed reduces leakage significantly, and that the effective Hamiltonian is able to accurately reproduce the behavior of the full system.

Note the difference in time-scale between Figs. 5.6 and 5.7. Due to the low oscillation frequency of the qubits in this setup, the computation time required to evaluate a switching cycle increases drastically. While time-consuming, it is possible to calculate when using the 4x4 effective Hamiltonian. For the full 50x50 system, however, the time required to compute the time evolution over such a time scale is on the order of several days[1].

[1] If only someone had invented a quantum computer we could run the simulations on instead...

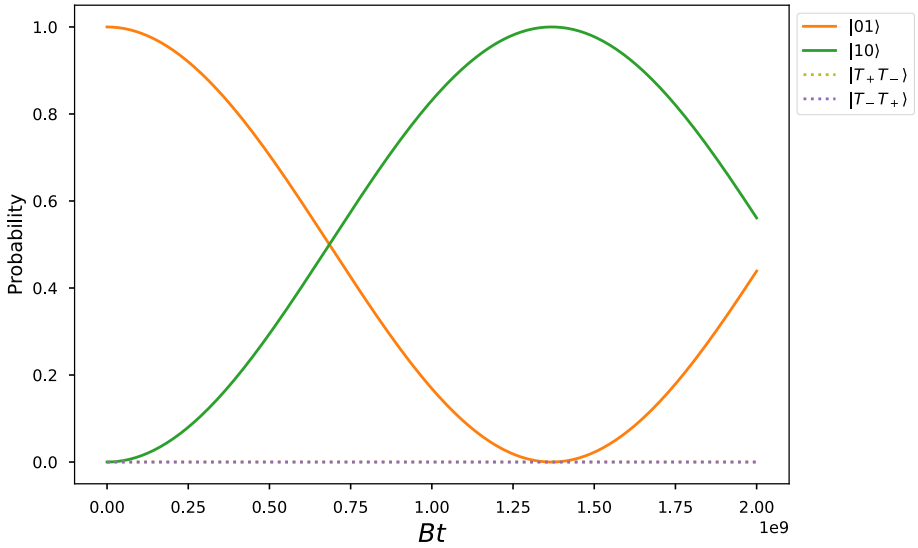

Figure 5.6: Time evolution of the $|01\rangle$, $|10\rangle$, $|T_+T_-\rangle$ and $|T_-T_+\rangle$ states, initialized in $|01\rangle$. Calculated using the effective Hamiltonian $\tilde{H}$ for $B = 10B_0$ and $\omega_0 = 4B_0$. The rotating coupling was set to $g_R = 0.1B_0$. The counter-rotating coupling constant was tuned to suppress leakage, setting $g_{CR} = 0.153B_0$.

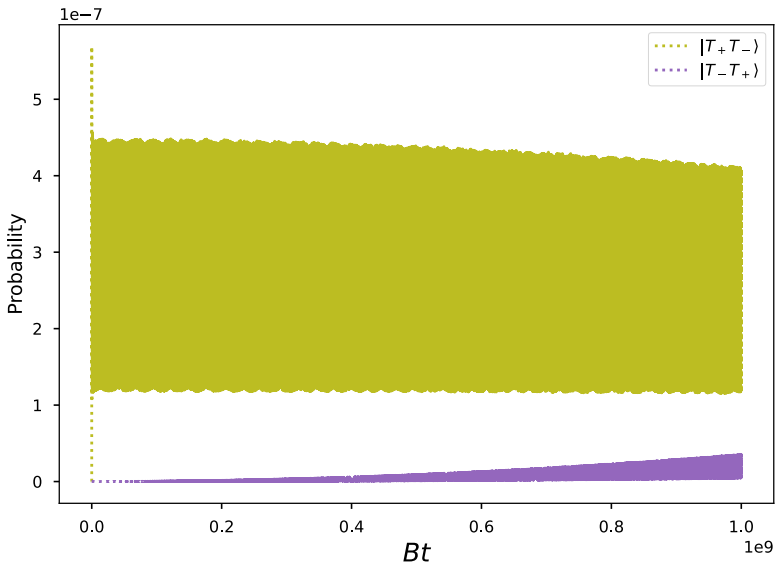

Figure 5.7: Time evolution of the occupation probabilities of the $|T_+T_-\rangle$ and $|T_-T_+\rangle$ states calculated using the full 50x50 Hamiltonian. for $B = 10B_0$ and $\omega_0 = 4B_0$. The rotating coupling was set to $g_R = 0.1B_0$. The counter-rotating coupling constant was tuned to suppress leakage, setting $g_{CR} = 0.153B_0$. Initialized in $|01\rangle$. Note the shorter time-scale compared to Fig. 5.6.

Chapter 6

Concluding remarks

In this thesis we have conducted a theoretical study of a ferromagnetically coupled singlet-triplet qubit system with qubits hosted in double quantum dots. By combining the tunability and electrical control of the DQD-based singlet-triplet qubit with the intermediate-range coupling provided by the ferromagnet, this platform proves to be a promising proposal to improve upon key challenges in the progress towards realizing quantum computing.

We build on the previously established framework for a similar system consisting of a ferromagnet coupling single spin qubits, and expand this to consider two electrons in a double quantum dot setup. The derivation of the system Hamiltonian is performed by considering it as tripartite; we derive Hamiltonians for the DQDs, the ferromagnet, and the interaction between the two. For the ferromagnet Hamiltonian, the inclusion of anisotropy causes the eigenmodes of the spin fluctuations in the ferromagnet to take the form of squeezed magnons. This squeezing results in the appearance of counter-rotating terms in the exchange interaction between the ferromagnet and the electron in the nearest of the dots in each of the DQDs. Importantly, this allows us to tune the coupling constants between the ferromagnet and the DQDs by altering the magnetic anisotropy.

The exchange coupling gives a contribution to $\hat{\sigma}_z$ that is only present for the electron in the dot closest of the dots. We include this effect as a magnetic field gradient across the DQD. Additionally, we include an applied magnetic field, a relative electrostatic potential, and the tunnel coupling between the two dots. With these parameters, we construct the DQD Hamiltonian, and obtain the full system Hamiltonian as the sum of the three parts. The qubit states $|0\rangle$ and $|1\rangle$ are then encoded in two energy eigenstates in the DQD.

With the goal of understanding the coupling between the $|01\rangle$ and $|10\rangle$ states, we proceed to derive effective an effective low-energy Hamiltonian for the 0-magnon subspace. To do so, we assume the magnon energy to be larger than the energy scale of the qubits and perform a fourth order SW transformation to decouple the $n = 0$ subspace, obtaining effective coupling terms between the $|01\rangle$ and $|10\rangle$ states. Furthermore, by considering how the coupling through the ferromagnet conserves the parity of excitation numbers, we divide this subspace into to subspaces of different parity states. This allows us to obtain an effective

13x13 Hamiltonian containing all states in the $n = 0$ subspace to which the $|01\rangle$ and $|10\rangle$ states are coupled to.

Through numerical analysis of the time evolution of the full system Hamiltonian, we are able to show that the coupled qubit system demonstrates coherent switching of the qubit states in several parameter regimes. Furthermore, the even mixing of the qubit states implies that leakage from the qubit subspace is minimal. These numerical results are compared to results obtained using the effective Hamiltonian. We show that, through the SW transformation, we have obtained a Hamiltonian in the $n = 0$ subspace that is able to accurately reproduce the dynamics of the system.

To proceed we assume the magnetic field as well as the magnon energy to be significantly larger than the qubit splitting, and consider the energy levels of the aforementioned 13 states. We find that we may, to first order, disregard leakage from $|01\rangle$ and $|10\rangle$ to any states other than the $|T_+T_-\rangle$ and $|T_-T_+\rangle$ states, due to these being significantly closer in energy than the remaining states. We thus obtain an effective Hamiltonian in a reduced Hilbert space containing only the $|01\rangle$, $|10\rangle$, $|T_+T_-\rangle$, and $|T_-T_+\rangle$ states describing their energies and the coupling between them.

In order to assess the coupling between the $|01\rangle$ and $|10\rangle$ states, along with the leakage to the $|T_+T_-\rangle$ and $|T_-T_+\rangle$ states, we perform a series expansion of the terms in the 4x4 effective Hamiltonian to obtain tractable expressions for the aforementioned coupling terms. Having obtained these, we find that by tuning the rotating and counter-rotating constants, we are able to completely suppress leakage to the $|T_+T_-\rangle$ and $|T_-T_+\rangle$ states. Numerical simulations using the full system Hamiltonian for the choice of coupling constants found to suppress leakage show markedly reduced leakage compared to previous simulations, and confirm the accuracy of the obtained effective Hamiltonian.

Bibliography

1. Finnseth, Ø. *Qubit-qubit coupling for spin qubits mediated by squeezed magnons,* Specialization project report in TFY4520. Department of Physics, Norwegian University of Science and Technology. 2021.
2. Feynman, R. P. Simulating Physics with Computers. *International Journal of Theoretical Physics* **21** (1982).
3. Arute, F. *et al.* Quantum supremacy using a programmable superconducting processor. *Nature 2019 574:7779* **574,** 505–510 (Oct. 2019).
4. Grover, L. K. Quantum Mechanics Helps in Searching for a Needle in a Haystack (1997).
5. Shor, P. W. Algorithms for quantum computation: Discrete logarithms and factoring. *Proceedings - Annual IEEE Symposium on Foundations of Computer Science, FOCS,* 124–134 (1994).
6. McClean, J. R., Babbush, R., Love, P. J. & Aspuru-Guzik, A. Exploiting locality in quantum computation for quantum chemistry. *Journal of Physical Chemistry Letters* **5,** 4368–4380 (July 2014).
7. Córcoles, A. D. *et al.* Challenges and Opportunities of Near-Term Quantum Computing Systems.
8. Kitaev, A. Y. Fault-tolerant quantum computation by anyons. *Annals of Physics* (2003).
9. Shor, P. W. Fault-tolerant quantum computation (May 1996).
10. Berman, P. R. *Introductory Quantum Mechanics* ISBN: 978-3-319-68596-0. http://link.springer.com/10.1007/978-3-319-68598-4 (Springer International Publishing, Cham, 2018).
11. Wie, C.-R. Two-Qubit Bloch Sphere.
12. Nielsen, M. A. & Chuang, I. L. *Quantum Computation and Quantum Information* 0–704. ISBN: 9781107002173. www.cambridge.org (2010).
13. Danon, J. *Lecture notes in Nanophysics* 2021.
14. Hemmer, P. C. *Kvantemekanikk* 5th ed. (Fagbokforlaget, 2005).
15. Storey, N. *Electronics, a Systems Approach* 5th ed. (Pearson Education Limited, 2013).

16. Bluhm, H. & Schreiber, L. R. Semiconductor Spin Qubits — A Scalable Platform for Quantum Computing? *2019 IEEE International Symposium on Circuits and Systems (ISCAS),* 1–5 (2019).

17. Ladd, T. D. *et al.* Quantum Computing. *Nature* **464,** 45–53 (Sept. 2010).

18. DiVincenzo, D. P. Topics in Quantum Computers (1996).

19. Loss, D. & DiVincenzo, D. P. Quantum computation with quantum dots. *Physical Review A* **57,** 120 (Jan. 1998).

20. Linder, J. *Intermediate Quantum Mechanics* (Bookboon, 2017).

21. Kelly, J. *et al.* State preservation by repetitive error detection in a superconducting quantum circuit. *Nature 2015 519:7541* **519,** 66–69 (Mar. 2015).

22. Niemietz, D., Farrera, P., Langenfeld, S. & Rempe, G. Nondestructive detection of photonic qubits. *Nature 2021 591:7851* **591,** 570–574 (Mar. 2021).

23. Pezzagna, S. & Meijer, J. Quantum computer based on color centers in diamond. *Applied Physics Reviews* **8,** 011308 (Feb. 2021).

24. Nayak, C., Simon, S. H., Stern, A., Freedman, M. & Das Sarma, S. Non-Abelian Anyons and Topological Quantum Computation (2008).

25. Wallquist, M., Hammerer, K., Rabl, P., Lukin, M. & Zoller, P. Hybrid quantum devices and quantum engineering. *Physica Scripta* **2009,** 014001 (Dec. 2009).

26. Vandersypen, L. M. & Eriksson, M. A. Quantum computing with semiconductor spins. *Physics Today* **72,** 38 (Aug. 2019).

27. Zhang, X. *et al.* Qubits based on semiconductor quantum dots. *Chinese Physics B* **27** (Feb. 2018).

28. Ono, K., Austing, D. G., Tokura, Y. & Tarucha, S. Current Rectification by Pauli Exclusion in a Weakly Coupled Double Quantum Dot System. *Mon. Not. R. Astron. Soc* **563,** 929 (2002).

29. Harvey-Collard, P. *et al.* High-fidelity single-shot readout for a spin qubit via an enhanced latching mechanism. *Physical Review X* **8** (Mar. 2017).

30. Jing, J. & Wu, L.-A. Decoherence and control of a qubit in spin baths: an exact master equation study OPEN. *ScienTific RepoRts* | **8,** 1471 (2018).

31. Jo, H., Ahn, J. & Song, Y. Qubit leakage suppression by ultrafast composite pulses. *Optics Express, Vol. 27, Issue 4, pp. 3944-3951* **27,** 3944–3951 (Feb. 2019).

32. Sala, A. & Danon, J. The exchange-only singlet-only spin qubit. *Physical Review B* **95** (Feb. 2017).

33. Cadellans, A. S. *Exchange-only, nuclear spin-free qubits in semiconductor quantum dots* PhD thesis (2020). ISBN: 978-82-326-4859-7. https://ntnuopen.ntnu.no/ntnu-xmlui/handle/11250/2682234.

34. Hanson, R., Kouwenhoven, L. P., Petta, J. R., Tarucha, S. & Vandersypen, L. M. K. Spins in few-electron quantum dots.

35. Petta, J. R. *et al.* Coherent manipulation of coupled electron spins in semiconductor quantum dots. *Science* **309,** 2180–2184 (Sept. 2005).

36. Martins, F. *et al.* Noise Suppression Using Symmetric Exchange Gates in Spin Qubits. *Physical Review Letters* **116,** 116801 (Mar. 2016).

37. Kawakami, E. *et al.* Electrical control of a long-lived spin qubit in a Si/SiGe quantum dot (2014).

38. Maune, B. M. *et al.* Coherent singlet-triplet oscillations in a silicon-based double quantum dot (2012).

39. Bacon, D., Kempe, J., Lidar, D. A. & Whaley, K. B. Universal Fault-Tolerant Quantum Computation on Decoherence-Free Subspaces (2000).

40. Borjans, F., Croot, X. G., Mi, X., Gullans, M. J. & Petta, J. R. Long-Range Microwave Mediated Interactions Between Electron Spins. *Nature* **577,** 195–198 (May 2019).

41. Kamra, A. & Belzig, W. Magnon-mediated spin current noise in ferromagnet | nonmagnetic conductor hybrids.

42. Trifunovic, L., Pedrocchi, F. L. & Loss, D. Long-Distance Entanglement of Spin Qubits via Ferromagnet. *Physical Review X* **3,** 041023 (Dec. 2013).

43. Sakurai, J. J. & Napolitano, J. *Modern Quantum Mechanics* 3rd ed., 0–548. ISBN: 9781108499996 (Cambridge University Press, Sept. 2021).

44. Saleh, B. E. A. & Teich, M. C. *Fundamentals of Photonics* 3rd ed. (Wiley, 2019).

45. Heisenberg, W. Über den anschaulichen Inhalt der quantentheoretischen Kinematik und Mechanik. *Zeitschrift für Physik 1927 43:3* **43,** 172–198 (Mar. 1927).

46. Robertson, H. P. The Uncertainty Principle. *Physical Review* **34,** 163 (July 1929).

47. Gerry, C. & Knight, P. *Introductory Quantum Optics* (2004).

48. Nolting, W. & Ramakanth, A. *Quantum theory of magnetism* 1–752. ISBN: 9783540854159 (Springer Berlin Heidelberg, 2009).

49. Holstein, T. & Primakoff, H. Field Dependence of the Intrinsic Domain Magnetization of a Ferromagnet. *Physical Review* **58,** 1098 (Dec. 1940).

50. Utermohlen, F. *Spin-Wave Theory Using the Holstein-Primakoff Transformation* 2020.

51. Bravyi, S., Divincenzo, D. P. & Loss, D. Schrieffer-Wolff transformation for quantum many-body systems (2011).

52. Skogvoll, I. C., Lidal, J., Danon, J. & Kamra, A. Tunable Anisotropic Quantum Rabi Model via a Magnon-Spin-Qubit Ensemble. *Physical Review Applied* **10,** 64008 (2021).

53. Bruus, H. & Flensberg, K. *Many-body Quantum Theory in Condensed Matter Physics, an introduction* (Oxford University Press, 2004).

54. Kamra, A., Agrawal, U. & Belzig, W. Noninteger-spin magnonic excitations in untextured magnets. *Physical Review B* **96,** 020411 (July 2017).

55. Kittel, C. *Introduction to Solid State Physics* 8th ed. (Wiley, 2005).

56. Skogvoll, I. C. *Tunable anisotropic quantum Rabi model via magnon/spin-qubit ensemble* MA thesis (Norwegian University of Science and Technology, 2021).

57. Zheng, H., Han, H., Zheng, J. & Yan, Y. Strain tuned magnetocrystalline anisotropy in ferromagnetic H-FeCl2 monolayer. *Solid State Communications* **271,** 66–70 (Mar. 2018).

58. Kamra, A., Belzig, W. & Brataas, A. Magnon-squeezing as a niche of quantum magnonics. *Applied Physics Letters* **117,** 090501 (Aug. 2020).

59. Kamra, A. & Belzig, W. Super-Poissonian Shot Noise of Squeezed-Magnon Mediated Spin Transport (2016).

60. Xie, Q.-T., Cui, S., Cao, J.-P., Amico, L. & Fan, H. Anisotropic Rabi model.

61. Johansson, J. R., Nation, P. D. & Nori, F. QuTiP 2: A Python framework for the dynamics of open quantum systems. *Computer Physics Communications* **184,** 1234–1240 (Nov. 2012).

62. *qutip.sesolve — QuTiP 4.6 Documentation* https://qutip.org/docs/latest/modules/qutip/sesolve.html#sesolve.

63. Styer, D. F. *et al.* Nine formulations of quantum mechanics. *American Journal of Physics* **70,** 288–297 (Mar. 2002).

64. Wolfram Research Inc., *Mathematica, Version 13.0.0* Champaign, IL, 2021. https://www.wolfram.com/mathematica.

65. Sala, A. & Danon, J. Leakage and dephasing in 28Si-based exchange-only spin qubits. *Physical Review B* **98,** 245409 (Dec. 2018).

Appendix A

Numerical analysis of time evolution

In this appendix we include the Python code used to create system Hamiltonians and solve the TDSE for the single spin qubit and the DQD qubit case. Both the construction of the Hamiltonian matrices, basis states, and projection operators, as well as the solve-function for the TDSE are handled using the QuTiP package.

```
import numpy as np
import qutip as qt


### DEFINING OPERATORS ###

## sigma-z operators
sigz1 = qt.tensor([qt.sigmaz(), qt.qeye(2)]) ## sigma z, dot 1
sigz2 = qt.tensor([qt.qeye(2), qt.sigmaz()]) ## sigma z, dot 2
sigz1.dims = [[4], [4]] ## setting dimensions
sigz2.dims = [[4], [4]]

## sigma-plus/minus operators
sp1 = qt.tensor([qt.sigmap(), qt.qeye(2)]) ## sigma plus, dot 1
sm1 = qt.tensor([qt.sigmam(), qt.qeye(2)]) ## sigma minus, dot 1
sp2 = qt.tensor([qt.qeye(2), qt.sigmap()]) ## sigma plus, dot 2
sm2 = qt.tensor([qt.qeye(2), qt.sigmam()]) ## sigma minus, dot 2
sp1.dims = [[4], [4]] ## setting dimensions
sm1.dims = [[4], [4]]
sp2.dims = [[4], [4]]
sm2.dims = [[4], [4]]

## magnon number operator
def num(N):
    n = qt.tensor([qt.num(N), qt.qeye(4)])
    n.dims = [[4*N], [4*N]]
    return n


```

```
## system Hamiltonian, single spin qubit
def h(w, N, gr = 0.1, gcr = 0.1, delta = 0):
    ## w: magnon energy, N: number of allowed magnons, gr,gcr:
    coupling constants
    ## delta: difference in qubit energy between dots 1 and 2

    I = qt.qeye(N) ## Identity operator in magnon Hilbert space
    I4 = qt.qeye(4) ## Identity operator in two-qubit Hilbert
    space
    c = qt.create(N) ## magnon creation operator
    d = qt.destroy(N) ## magnon annihilation operator

    ## magnon energy
    term1 = w*num(N)

     ## constructing sigma z in full system Hilbert space
    sg1 = qt.tensor(I, sigz1)
    sg1.dims = [[4*N], [4*N]]
    sg2 = qt.tensor(I, sigz2)
    sg2.dims = [[4*N], [4*N]]
    term2 = (sg1+(1-delta)*sg2)*0.5 ## qubit energy

    ## magnon operators in full system Hilbert space
    c4 = qt.tensor([c, I4])
    d4 = qt.tensor([d, I4])
    ## spin excitation and relaxation operators in full system
    Hilbert space
    sm1N = qt.tensor([I, sm1])
    sp1N = qt.tensor([I, sp1])
    sm2N = qt.tensor([I, sm2])
    sp2N = qt.tensor([I, sp2])

    ## rotating coupling term
    term32 = gr*(c4*sm1N + d4*sp1N + c4*sm2N + d4*sp2N)
    ## counter-rotating coupling terms
    term42 = gcr*(c4*sp1N + d4*sm1N + c4*sp2N + d4*sm2N)
    term32.dims = [[4*N], [4*N]]
    term42.dims = [[4*N], [4*N]]

    return term1+term2+term32+term42 ## returns full system
    Hamiltonian

## CALCULATING TIME EVOLUTION OF SINGLE SPIN SYSTEM ##
def evolution(w, N, gr, gcr, tstart, tend, state, steps = 10000,
    delta = 0):
    ## state: initial state (0+n: up/up, 1+n: up/down, 2+n: down/
    up, 3+n:down/down)
    init = qt.basis(4*N, state)
    ## n: desired magnon occupation number

    I = qt.qeye(N)

    ## spin state projection operators
    updown = qt.basis(4*N, 1).proj()
```

```
78      downup = qt.basis(4*N, 2).proj()
79      downdownmag = qt.basis(4*N, 7).proj()
80      upupmag = qt.basis(4*N, 4).proj()
81      upup = qt.basis(4*N, 0).proj()
82      downdown = qt.basis(4*N, 3).proj()
83      updownmag = qt.basis(4*N, 5).proj()
84      downupmag = qt.basis(4*N, 6).proj()
85      downdown2 = qt.basis(4*N, 11).proj()
86      upup2 = qt.basis(4*N, 8).proj()
87
88      ## CHOOSE OPERATORS TO EVALUATE HERE ##
89      ops = [upup, updown, downup, downdownmag, upupmag]
90
91      a = h(w, N, gr, gcr, delta) ## system Hamiltonian
92      tlist = np.linspace(tstart, tend, steps) ## time steps
93
94      ## Solving TDSE ##
95      result = qt.sesolve(a, init, tlist, ops, options = qt.Options
        (nsteps = 50000000))
96      return result
```

Listing A.1: Single spin qubit system

```
1  import numpy as np
2  import qutip as qt
3
4
5  ### DEFINING OPERATORS ###
6  I5 = qt.qeye(5)
7
8  ## sigma plus / sigma minus
9  sigmaminus = (1/np.sqrt(2))*qt.Qobj(np.array
       ([[0,0,0,0,0],[1,0,0,0,0],[-1,0,0,0,0],[0,1,1,0,0],[0,0,0,0,0]])
       )
10 sigmaplus = (1/np.sqrt(2))*qt.Qobj(np.array
       ([[0,1,-1,0,0],[0,0,0,1,0],[0,0,0,1,0],[0,0,0,0,0],[0,0,0,0,0]])
       )
11
12 #transfer to full Hilbert space
13 sgmp1 = qt.tensor(sigmaplus, I5)
14 sgmp1.dims = [[25],[25]]
15 sgmp2 = qt.tensor(I5, sigmaplus)
16 sgmp2.dims = [[25],[25]]
17
18 sgmm1 = qt.tensor(sigmaminus, I5)
19 sgmm1.dims = [[25],[25]]
20 sgmm2 = qt.tensor(I5, sigmaminus)
21 sgmm2.dims = [[25],[25]]
22
23
24 ### DQD Hamiltonian ###
25 def h_basis_B(B, epsilon, t, dbz = 0):
```

```
26      ## B: applied magnetic field, epsilon: detuning parameter, t:
        tunnel coupling, dbz: magnetic field gradient
27      return qt.Qobj(np.array([[B,0,0,0,0], [0,0,dbz,0,0], [0,dbz
        ,0,0,t], [0,0,0,-B,0], [0,0,t,0,-epsilon]]))
28
29
30  ### FULL HAMILTONIAN OF COUPLED DQD SYSTEM ###
31  def two_dots_h(B, w, N, gr, gcr, epsilons, t, dbz = [0,0]):
32      ##epsilons: detuning for each dot [e1, e2]
33      ## dbz: magnetic field gradient for each dot [dbz1, dbz2]
34      IN = qt.qeye(N)
35      ## magnon energy
36      term1 = w*qt.num(N)
37      term1 = qt.tensor(term1, I5,I5)
38      term1.dims = [[N*25], [N*25]]
39
40      ## qubit energies
41      h1  = qt.tensor(IN, h_basis_B(B, epsilons[0], t, dbz[0]), I5)
42      h1.dims = [[N*25], [N*25]]
43      h2  = qt.tensor(IN, I5, h_basis_B(B, epsilons[1], t, dbz[0]))
44      h2.dims = [[N*25], [N*25]]
45      term2 = h1+h2
46
47      ## interaction energies
48      c = qt.tensor(qt.create(N), I5, I5) ## magnon creation
        operator
49      c.dims = [[N*25], [N*25]]
50      d = qt.tensor(qt.destroy(N), I5, I5) ## magnon annihilation
        operator
51      d.dims = [[N*25], [N*25]]
52
53      sp1 = qt.tensor(IN, sgmp1) ## sigma plus, DQD 1
54      sp1.dims = [[N*25], [N*25]]
55      sp2 = qt.tensor(IN, sgmp2) ## sigma plus, DQD 2
56      sp2.dims = [[N*25], [N*25]]
57      sm1 = qt.tensor(IN, sgmm1) ## sigma minus, DQD 1
58      sm1.dims = [[N*25], [N*25]]
59      sm2 = qt.tensor(IN, sgmm2) ## sigma minus, DQD 2
60      sm2.dims = [[N*25], [N*25]]
61      term31 = gr*(c*sm1 + d*sp1) + gcr*(c*sp1 + d*sm1) ## rotating
        terms
62      term32 = gr*(c*sm2 + d*sp2) + gcr*(c*sp2 + d*sm2) ## counter-
        rotating terms
63
64      term3 = term31 + term32
65      return term1 + term2 + term3 ## returns full system
        Hamiltonian
66
67  ### TIME EVOLUTION OF COUPLED DQD SYSTEM ###
68  def evo_two_dots(B, w, N, tstart, tend, es, tc, steps = 50000, g1
        = 0.1, g2 = 0.1, dbzs = [0,0], res = True, mode = 'qb'):
69      ## es: detuning list [e1,e2]
70      ## g1: rotating constant, g2: counter-rotating constant
71      ## res: True -> magnon energy resonates with qubit splitting
```

```
72      ## res: False -> magnon energy takes input value w
73
74      ## mode: operation mode of function
75      # 'qb': evaluates the qubit states 11, 01, 10, 00
76      # 'leak': evaluates leakage to T+T- and T-T+
77      # 'dqd1'/'dqd2': evaluates the eigenstates of dqd1/dqd2
78      # 'mag': evaluates occupancy of different magnon number
    states
79
80      IN = qt.qeye(N) ## magnon Hilbert space identity operator
81      tlist = np.linspace(tstart, tend, steps)
82
83      ## resonant magnon energy
84      w_opt = h_basis_B(B, es[0], tc, dbzs[0]).eigenenergies()[2]-
    h_basis_B(B, es[0], tc, dbzs[0]).eigenenergies()[1]
85      if res:
86          a = two_dots_h(B, w_opt, N, g1, g2, es, tc, dbz = dbzs)
87
88      ## off-resonant magnon energy
89      else:
90          a = two_dots_h(B, w, N, g1, g2, es, tc, dbz = dbzs)
91
92      ## eigenstates of DQD Hamiltonian for DQD 1, low energy to
    high energy
93      zero1 = h_basis_B(B, es[0], tc, dbzs[0]).eigenstates()[1][0]
94      one1 = h_basis_B(B, es[0], tc, dbzs[0]).eigenstates()[1][1]
95      two1 = h_basis_B(B, es[0], tc, dbzs[0]).eigenstates()[1][2]
96      three1 =  h_basis_B(B, es[0], tc, dbzs[0]).eigenstates()
    [1][3]
97      four1 = h_basis_B(B, es[0], tc, dbzs[0]).eigenstates()[1][4]
98
99      ## eigenstates of DQD Hamiltonian for DQD 2, low energy to
    high energy
100     zero2 = h_basis_B(B, es[1], tc, dbzs[1]).eigenstates()[1][0]
101     one2 = h_basis_B(B, es[1], tc, dbzs[1]).eigenstates()[1][1]
102     two2 = h_basis_B(B, es[1], tc, dbzs[1]).eigenstates()[1][2]
103     three2 =  h_basis_B(B, es[1], tc, dbzs[1]).eigenstates()
    [1][3]
104     four2 = h_basis_B(B, es[1], tc, dbzs[1]).eigenstates()[1][4]
105
106
107     ## PROJECTION OPERATORS FOR EIGENSTATES OF EACH DOT ##
108
109     p01 = zero1.proj()
110     p01 = qt.tensor(IN, p01, I5)
111     p11 = one1.proj()
112     p11 = qt.tensor(IN, p11, I5)
113     p21 = two1.proj()
114     p21 = qt.tensor(IN, p21, I5)
115     p31 = three1.proj()
116     p31 = qt.tensor(IN, p31, I5)
117     p41 = four1.proj()
118     p41 = qt.tensor(IN, p41, I5)
119     p02 = zero2.proj()
```

```
120     p02 = qt.tensor(IN, I5, p02)
121     p12 = one2.proj()
122     p12 = qt.tensor(IN, I5, p12)
123     p22 = two2.proj()
124     p22 = qt.tensor(IN, I5, p22)
125     p32 = three2.proj()
126     p32 = qt.tensor(IN, I5, p32)
127     p42 = four2.proj()
128     p42 = qt.tensor(IN, I5, p42)
129
130     dot1 = [p01, p11, p21, p31, p41]
131     dot2 = [p02, p12, p22, p32, p42]
132
133     ## PROJECTION OPERATORS FOR T+T- AND T-T+
134
135     pcpm = qt.tensor(four1, zero2).proj()
136     pcpm = qt.tensor(IN, pcpm)
137     pcmp = qt.tensor(zero1, four2).proj()
138     pcmp = qt.tensor(IN, pcmp)
139
140     leak = [pcpm, pcmp]
141
142
143      ## PROJECTION OPERATORS FOR QUBIT STATES 11, 01, 10, 00 ##
144
145     pc00 = qt.tensor(one1, one2).proj()
146     pc00 = qt.tensor(IN, pc00)
147     pc01 = qt.tensor(one1, two2).proj()
148     pc01 = qt.tensor(IN, pc01)
149     pc10 = qt.tensor(two1, one2).proj()
150     pc10 = qt.tensor(IN, pc10)
151     pc11 = qt.tensor(two1, two2).proj()
152     pc11 = qt.tensor(IN, pc11)
153     qb_list = [pc00, pc01, pc10, pc11]
154
155     ## MAGNON OCCUPANCY OPERATORS ##
156     mag = qt.tensor(qt.num(N), I5,I5) #magnon occupancy
157     mag = []
158     for i in range(N):
159         temp = qt.basis(N, i).proj()
160         mag.append(qt.tensor(temp, I5, I5))
161
162     ### CHOOSE INITIALIZATION HERE ###
163     init = qt.tensor(qt.basis(N, 0), one1, two2).unit()
164
165     ## SOLVING TDSE FOR GIVEN MODE ##
166     if mode == 'dqd1':
167         result = qt.sesolve(a, init, tlist, dot1, options = qt.
    Options(nsteps = 5000000), progress_bar = True)
168         ## note progress bar as these simulations take
    significantly longer than the single spin qubit case
169         ## disabled by setting progress_bar = None
170
171     elif mode == 'dqd2':
```

```
172         result = qt.sesolve(a, init, tlist, dot2, options = qt.
    Options(nsteps = 5000000), progress_bar = True)
173
174     elif mode == 'mag':
175         result = qt.sesolve(a, init, tlist, mag, options = qt.
    Options(nsteps = 5000000), progress_bar = True)
176
177     elif mode == 'leak':
178         result = qt.sesolve(a, init, tlist, leak, options = qt.
    Options(nsteps = 5000000), progress_bar = True)
179
180     elif mode == 'qb':
181         result = qt.sesolve(a, init, tlist, qb_list, options = qt
    .Options(nsteps = 5000000), progress_bar = True)
182
183     else:
184         print('Input mode does not match accepted value.')
185         return
186     return result
```

Listing A.2: Singlet-triplet qubit system

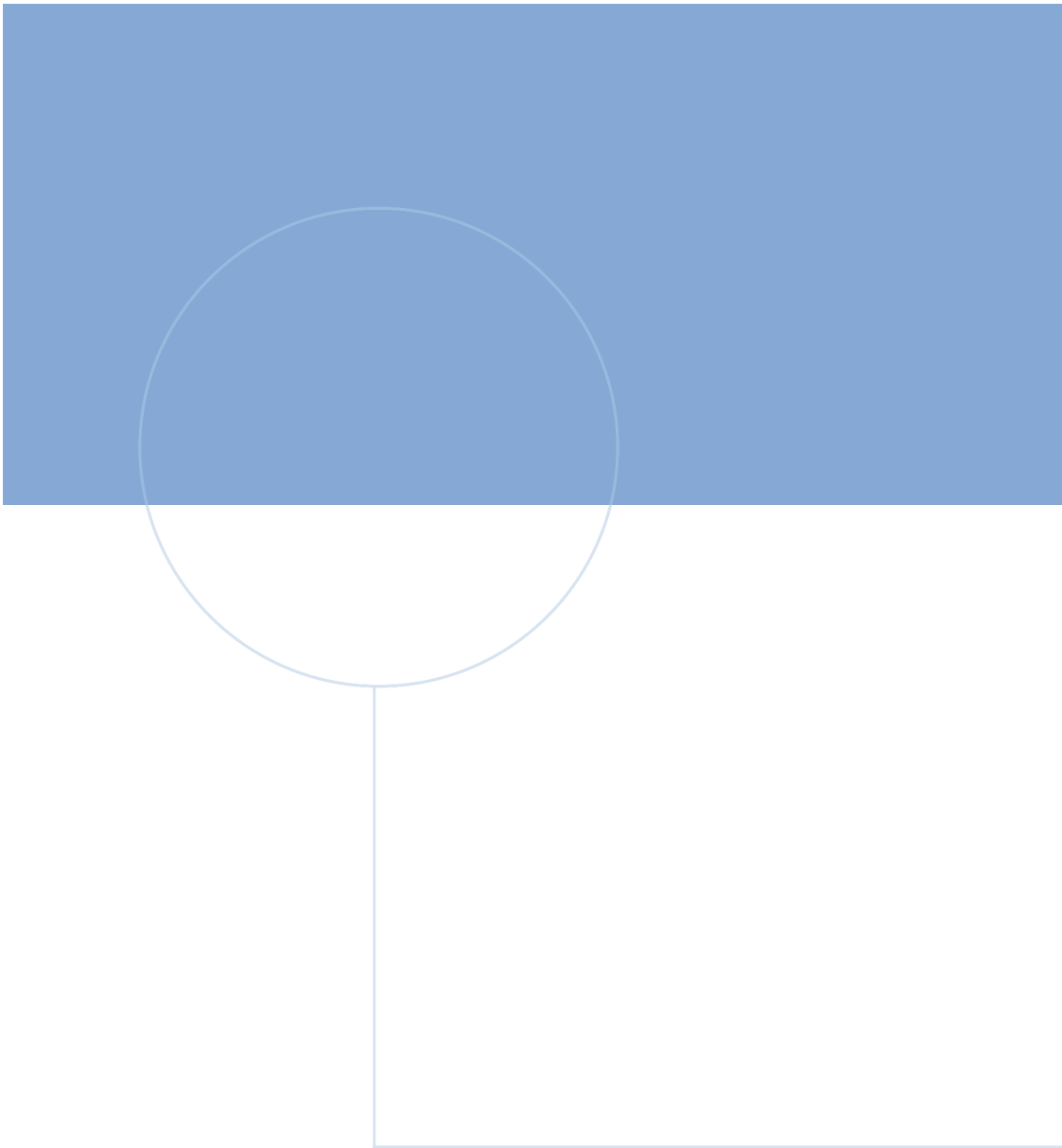

NTNU

Norwegian University of
Science and Technology